

Experimental Studies of Injector Array Configurations for Circular Scramjet Combustors

Christopher A. Rock

Dissertation submitted to the faculty of the Virginia Polytechnic Institute and State University in partial fulfillment of the requirements for the degree of

Doctor of Philosophy
in
Aerospace Engineering

Joseph A. Schetz, Chair
William J. Devenport
Walter F. O'Brien
Michael K. Philen

September 1, 2010
Blacksburg, VA

Keywords: Scramjet, Supersonic Combustion, Hypersonic Propulsion,
Fuel Injection, Mixing

Copyright © 2010 by Christopher Rock

Experimental Studies of Injector Array Configurations for Circular Scramjet Combustors

Christopher A. Rock

Abstract

A flush-wall injector model and a strut injector model representative of state of the art scramjet engine combustion chambers were experimentally studied in a cold-flow (non-combusting) environment to determine their fuel-air mixing behavior under different operating conditions. The experiments were run at nominal freestream Mach numbers of 2 and 4, which simulates combustor conditions for nominal flight Mach numbers of 5 and 10. The flush-wall injector model consists of sixteen inclined, round, sonic injectors distributed around the wall of a circular duct. The strut injector model has sixteen inclined, round, sonic injectors distributed across four struts within a circular duct. The struts are slender, inclined at a low angle to minimize drag, and have two injectors on each side. The experiments investigated the effects of injectant molecular weight, freestream Mach number, and jet-to-freestream momentum flux ratio (\bar{q}) on the fuel-air mixing process. Helium, methane, and air injectants were studied to vary the injectant molecular weight over the range of 4-29. All of these experiments were performed to support the needs of an integrated experimental and computational research program, which has the goal of upgrading the turbulence models that are used for Computational Fluid Dynamics predictions of the flow inside a scramjet combustor. The primary goals of this study were to use injector models that represent state of the art scramjet engine combustion chambers to provide validation data to support the development of turbulence model upgrades and to add to the sparse database of mixing results in such configurations. The main experimental results showed that higher molecular weight injectants had approximately the same amount of penetration in the far field as lower molecular weight injectants at the same \bar{q} . Higher molecular weight injectants also demonstrated a mixing rate that was the same as or slower than lower molecular weight injectants depending on the flow conditions. A comparison of the experimental results for the two different injector models revealed that the flush-wall injector mixed significantly faster than the strut injector in all of the experimental cases.

Acknowledgements

First and foremost, I would like to thank my parents and family for their love and support. My father was the one who first introduced me to the idea of pursuing a PhD, so that I would have the option to become a college professor. Without his encouragement, I probably would not have decided to pursue this degree.

Second, I would like to acknowledge my advisor, Dr. Joseph Schetz, who has been a great mentor for the past few years. I would also like to thank him for providing me the opportunity to come to Virginia Tech through a graduate assistantship. I have also very much enjoyed the many stories that he has to tell about work, life, and travel.

I would also like to acknowledge my committee members: Dr. Devenport, Dr. O'Brien, and Dr. Philen. They have all demonstrated a very high level of commitment to their students through their teaching. I am grateful for the time they have spent assisting me with this research, which has certainly improved the end results.

Additionally, I would like to acknowledge the Air Force Research Laboratory for funding this research through Combustion Research and Flow Technology, Inc. (CRAFT Tech). I would also like to thank Ron Ungewitter from CRAFT Tech, who performed CFD for all of the experimental cases that I ran. Some of his CFD results are discussed in this dissertation.

I also thank the members of the AOE department staff who contributed to this research including Mark Montgomery, Steve Edwards, James Lambert, and Bruce Stanger. Mark was instrumental in building the data acquisition rack for the hypersonic tunnel and also provided electrical support for all of our lab equipment. Steve provided his LabVIEW expertise to assist me with equipment programming tasks. James and Bruce built the injector models, several instruments, and other parts needed for the experiments.

Finally, I would like to thank the current and former members of the Scramjet Research Group at Virginia Tech including Alex Duchmann, Ryan Throckmorton, Luca Maddalena, Scott Burger, Brian Leslie, and Ryan Meritt. I am especially appreciative for the help of Alex and Ryan Throckmorton, who trained me to use our lab equipment. I have enjoyed meeting and working with all of the members of this group.

Table of Contents

Acknowledgements	iii
List of Figures.....	viii
List of Tables	xiii
Nomenclature	xiv
Chapter 1: Introduction.....	1
1.1 The Scramjet Engine.....	1
1.2 Historical Background on the Scramjet.....	3
1.3 The Fuel Injection and Mixing Problem in a Scramjet.....	4
1.4 Theoretical Background on Fuel Injection and Mixing.....	4
1.4.1 Mixing Enhancement.....	4
1.4.2 Non-Dimensional Injection Parameters.....	6
1.4.3 Flow Features of Transverse Jets in Supersonic Flow.....	7
1.4.4 Fuel Selection Considerations.....	8
1.4.5 Combustor Design Considerations	9
1.4.6 Boundary Layer Effects	10
1.4.7 Performance Characterization.....	10
1.4.8 Empirical Correlations	11
1.5 Motivation for the Current Research	11
Chapter 2: Experimental Methods	15
2.1 Test Facilities.....	15
2.1.1 Hypersonic Wind Tunnel Facility.....	15
2.1.1.1 Data Acquisition and Tunnel Control.....	18
2.1.1.2 Boundary Layer Measurements	18
2.1.2 Supersonic Wind Tunnel Facility	21
2.1.3 Supersonic Free-Jet Facility.....	21
2.2 Test Models.....	23
2.2.1 Flush-Wall Injector Model.....	23
2.2.2 Strut Injector Model.....	24
2.2.3 Injectant Supply System	25

2.3	Instrumentation	28
2.3.1	Mass Flow Controllers	28
2.3.2	Orifice Plate Flow Meter	29
2.3.3	Probe Traversing System	31
2.3.4	Concentration Sampling Probe	32
2.3.4.1	Principle of Operation	35
2.3.4.2	Calibration	37
2.3.4.3	Data Analysis	41
2.3.4.4	Measurement Uncertainty	41
2.3.4.5	Correction for Test Facility Effects on Concentration Measurements	42
2.3.5	Cone-Static Probe	44
2.3.6	Aero-Thermodynamic Triple-Rake Probe	44
2.3.7	Conical Five-Hole Pressure Probe	45
2.3.7.1	Calibration	45
2.3.7.2	Data Analysis	50
2.3.7.3	Measurement Uncertainty	52
2.4	Multiple Probe Survey Method and Data Analysis Procedure	53
2.4.1	Outside of the Region of the Injectant Plume	53
2.4.1.1	Measurement Uncertainty	54
2.4.2	Within the Region of the Injectant Plume	54
2.4.2.1	Measurement Uncertainty	54
Chapter 3: Studies of a Flush-Wall Injector Array for Circular Scramjet Combustors		56
3.1	Test Conditions	56
3.2	Concentration Measurements	59
3.3	Mach Number and Total Pressure Measurements	64
3.4	Supporting CFD Analysis from Collaborators	68
3.5	Conclusions	74
Chapter 4: Studies of a Strut Injector Array for Circular Scramjet Combustors		76
4.1	Test Conditions	76
4.2	Concentration Measurements	79
4.3	Mach Number and Total Pressure Measurements	83

4.4	Supporting CFD Analysis from Collaborators	88
4.5	Conclusions.....	94
	Chapter 5: Discussion.....	96
5.1	Summary of Conclusions.....	96
5.2	Comparison of the Flush-Wall and Strut Injector Configurations.....	100
5.3	Recommendations for Future Work.....	107
5.3.1	Cold-Flow Optical Concentration Measurements	107
5.3.2	Combustion Experiments.....	107
5.3.3	Test Facility Improvements	108
5.3.4	Concentration Probe Improvements	110
	Appendix A: Taylor-Maccoll Solution for a 10 Degree Sharp Cone with Variable Specific Heat Ratio.....	113
	Appendix B: Discussion of the Differences between the Straight Tip and Angled Tip Concentration Probes	116
	Appendix C: Uncertainty Analysis.....	118
C.1	Boundary Layer Measurements	119
C.2	Injectant Mass Flow Rate Measurements.....	120
C.2.1	Mass Flow Controllers	121
C.2.2	Orifice Plate Flow Meter.....	121
C.3	Concentration Measurements.....	122
C.3.1	Data Reduction Code Validation.....	123
C.3.2	Analysis Results	124
C.4	Mach Number and Total Pressure Measurements.....	128
C.4.1	Measurement of an Airflow	128
C.4.1.1	Data Reduction Code Validation	129
C.4.1.2	Analysis Results.....	130
C.4.2	Measurement of a Gas Mixture.....	130
C.4.2.1	Analysis Results.....	132
	Appendix D: Proposed New Concentration Probe Design.....	133
D.1	Introduction.....	133
D.1.1	Desired Features for a Concentration Probe	133

D.1.2	Previous Concentration Probe Designs.....	134
D.1.2.1	Ninnemann and Ng Design (Virginia Tech, 1989).....	135
D.1.2.2	Brown and Rebollo Design (Caltech, 1972).....	136
D.1.2.3	Xillo et al. Design (Virginia Tech, 1998).....	136
D.1.2.4	Maddalena Design (Virginia Tech, 2007).....	137
D.1.2.5	Additional Background on the Use of the Ng and Maddalena Probes	138
D.1.3	Design Goals for the New Concentration Probe.....	139
D.2	Component Selection.....	139
D.2.1	Hot-Film Sensor.....	140
D.2.2	Pressure Transducer.....	141
D.2.3	Thermocouple.....	142
D.3	Probe Design.....	142
D.3.1	One Dimensional, Steady Flow Analysis.....	145
D.4	Conclusions.....	148
	References.....	150

List of Figures

Figure 1.1: Diagram of a scramjet engine.....	2
Figure 1.2: Examples of various injector configurations (from Kutschenreuter ⁵).....	5
Figure 1.3: Flow features of an underexpanded transverse jet in supersonic flow [from Ben-Yakar et al. (top) and Gruber et al. (bottom)].....	8
Figure 1.4: Airbreathing engine operating envelopes for hydrogen fuel (red) vs. hydrocarbon fuel (blue) [from Van Wie et al. ²].....	9
Figure 2.1: Virginia Tech hypersonic wind tunnel facility.....	16
Figure 2.2: Coordinate system associated with the hypersonic tunnel	16
Figure 2.3: Variation of total pressure during hypersonic tunnel run at Mach 2.....	17
Figure 2.4: Variation of total pressure during hypersonic tunnel run at Mach 4.....	17
Figure 2.5: Pitot pressure profile at the exit of the Mach 2 nozzle for the hypersonic tunnel.....	19
Figure 2.6: Mach number profile at the exit of the Mach 2 nozzle for the hypersonic tunnel	20
Figure 2.7: Pitot pressure profile at the exit of the Mach 4 nozzle for the hypersonic tunnel.....	20
Figure 2.8: Mach number profile at the exit of the Mach 4 nozzle for the hypersonic tunnel	21
Figure 2.9: Virginia Tech supersonic wind tunnel facility	22
Figure 2.10: Virginia Tech supersonic free-jet facility.....	22
Figure 2.11: Picture of the flush-wall injector model fitted to the hypersonic wind tunnel (flow is from right to left)	24
Figure 2.12: Picture of the flush-wall injector array (looking upstream)	24
Figure 2.13: Picture of the strut injector model (looking upstream).....	25
Figure 2.14: Injection system for the flush-wall injector model using orifice plate flow meter .	26
Figure 2.15: Injection system for the flush-wall injector model using mass flow controllers.....	27
Figure 2.16: Injection system for the strut injector model.....	27
Figure 2.17: Picture of one of the mass flow controllers (left) and its power supply and control module (right)	29
Figure 2.18: Picture of the probe traversing system mounted to the test cabin (test cabin side walls are removed).....	32
Figure 2.19: Comparison of the shock system near the probe tip for a non-aspirating probe (left) vs. an aspirating probe (right) [from Xillo et al.].....	33

Figure 2.20: Diagram of the concentration probe (from Maddalena).....	34
Figure 2.21: Picture of the concentration probe with the straight tip and integrated cone-static probe (left) vs. the concentration probe with the angled tip (right)	35
Figure 2.22: Picture of the calibration tank for the concentration probe	39
Figure 2.23: Concentration probe calibration results for a helium-air mixture for an overheat ratio of 1.0.....	39
Figure 2.24: Concentration probe calibration results for a methane-air mixture for an overheat ratio of 1.0.....	40
Figure 2.25: Concentration probe calibration results for a helium-air mixture for an overheat ratio of 0.5.....	40
Figure 2.26: Concentration probe measurement uncertainty.....	41
Figure 2.27: Fuel-air ratio variation during typical hypersonic tunnel runs for different injectants and freestream Mach numbers	43
Figure 2.28: Picture of the triple-rake probe with Pitot probe (top), total temperature probe (middle), and cone-static probe (bottom).....	45
Figure 2.29: Picture of the five-hole probe (left) and drawing of the probe tip (right)	45
Figure 2.30: Five-hole probe angular calibration data.....	47
Figure 2.31: Five-hole probe angular calibration map.....	47
Figure 2.32: Five-hole probe Mach number calibration	49
Figure 2.33: Five-hole probe correction factor map	52
Figure 3.1: Experimental mass fraction contours for the flush-wall injector, $M_\infty = 4$, He injection cases	60
Figure 3.2: Experimental mixing results along the injector centerline for the flush-wall injector model.....	61
Figure 3.3: Experimental Mach number contours for the flush-wall injector, $M_\infty = 4$, He and air injection cases	66
Figure 3.4: Experimental total pressure contours for the flush-wall injector, $M_\infty = 4$, He and air injection cases	66
Figure 3.5: Experimental Mach number and total pressure contours for the flush-wall injector, $M_\infty = 2$, He injection case.....	67

Figure 3.6: Experimental Mach number results along the injector centerline for the flush-wall injector model	67
Figure 3.7: Experimental total pressure results along the injector centerline for the flush-wall injector model	68
Figure 3.8: CFD mass fraction contours for the flush-wall injector, $M_\infty = 4$, He injection ($\bar{q} = 1.71$) case.....	70
Figure 3.9: CFD Mach number contours for the flush-wall injector, $M_\infty = 4$, He injection ($\bar{q} = 1.71$) case.....	71
Figure 3.10: Experiment vs. CFD mass fraction contour comparison for the flush-wall injector, $M_\infty = 4$, He injection ($\bar{q} = 1.71$) case	72
Figure 3.11: Experiment vs. CFD comparison of the mixing results along the injector centerline for the flush-wall injector, $M_\infty = 4$, He injection ($\bar{q} = 1.71$) case	72
Figure 3.12: Experiment vs. CFD Mach number contour comparison for the flush-wall injector, $M_\infty = 4$, He injection ($\bar{q} = 1.71$) case	73
Figure 3.13: Experiment vs. CFD total pressure contour comparison for the flush-wall injector, $M_\infty = 4$, He injection ($\bar{q} = 1.71$) case	74
Figure 4.1: Experimental mass fraction contours for the strut injector, $M_\infty = 4$, He injection case	79
Figure 4.2: Experimental mixing results along the centerline of the injectant plume for the strut injector (the dashed line indicates the outer edge of the strut)	80
Figure 4.3: Experimental Mach number contours for the strut injector, $M_\infty = 4$, He and air injection cases	85
Figure 4.4: Experimental total pressure contours for the strut injector, $M_\infty = 4$, He and air injection cases	85
Figure 4.5: Experimental Mach number results along the centerline of the injectant plume for the strut injector model	86
Figure 4.6: Experimental total pressure results along the centerline of the injectant plume for the strut injector model	87
Figure 4.7: Comparison of the experimental Mach number results along the centerline of the injectant plume for the strut injector, $M_\infty = 4$ cases	87

Figure 4.8: Comparison of the experimental total pressure results along the centerline of the injectant plume for the strut injector, $M_\infty = 4$ cases	88
Figure 4.9: CFD mass fraction contours for the strut injector, $M_\infty = 4$, He injection ($\bar{q} = 3.13$) case	90
Figure 4.10: CFD Mach number contours along the length of the duct for the strut injector, $M_\infty = 4$, He injection ($\bar{q} = 3.13$) case.....	91
Figure 4.11: Experiment vs. CFD mass fraction contour comparison for the strut injector,.....	91
Figure 4.12: Experiment vs. CFD comparison of the mixing results along the plume centerline for the strut injector, $M_\infty = 4$, He injection ($\bar{q} = 3.13$) case	92
Figure 4.13: Experiment vs. CFD Mach number contour comparison for the strut injector, $M_\infty = 4$, He injection ($\bar{q} = 3.13$) case.....	93
Figure 4.14: Experiment vs. CFD Mach total pressure contour comparison for the strut injector, $M_\infty = 4$, He injection ($\bar{q} = 3.13$) case	93
Figure 5.1: Comparison of the experimental mass fraction contours for the flush-wall injector vs. the strut injector (for He injection, $M_\infty = 4$, $f = 0.0098$)	104
Figure 5.2: Comparison of the experimental mixing results along the plume centerline for the flush-wall injector vs. the strut injector	105
Figure 5.3: Comparison of the experimental Mach number and total pressure results along the plume centerline for the flush-wall injector vs. the strut injector	106
Figure 5.4: Proposed new concentration probe design	111
Figure 5.5: Size comparison of the proposed new concentration probe vs. the existing concentration probe.....	112

Figures in Appendices

Figure A.1: Diagrams of a Pitot probe and a cone-static probe in supersonic flow.....	114
Figure D.1: Comparison of previous concentration probe designs.....	134
Figure D.2: Comparison of components considered for the new concentration probe.....	140
Figure D.3: New concentration probe design with mounting base attached.....	144
Figure D.4: Comparison of the flow velocity at the sensor plane for the new concentration probe design vs. the existing probe.....	146

Figure D.5: Comparison of the flow through time for the new concentration probe design vs. the existing probe.....147

Figure D.6: Location of the normal shock in the probe tip for both the new concentration probe design and the existing probe design.....148

List of Tables

Table 2.1: Mach number and total pressure uncertainties (+/- percent of reading) that apply when an airflow is being measured.....	53
Table 2.2: Mach number and total pressure uncertainties (+/- percent of reading) that apply when a gas mixture is being measured	55
Table 3.1: Flush-wall injector test matrix (includes nominal experimental conditions)	58
Table 3.2: Flush-wall injector mixing results (for the plume created by a single circular injector)	61
Table 4.1: Strut injector test matrix (includes nominal experimental conditions).....	78
Table 4.2: Strut injector mixing results (for the plume created by an entire strut with four circular injectors)	81
Table 5.1: Experimental conditions and mixing results for the flush-wall injector vs. the strut injector	102

Tables in Appendices

Table A.1: Taylor-Maccoll solution for a 10 degree sharp cone with variable specific heat ratio.....	115
Table B.1: Comparison of the straight tip and angled tip concentration probe configurations..	117
Table C.1: Accuracy ratings for pressure transducers and thermocouples.....	119
Table C.2: Data reduction code validation results for the concentration probe.....	124
Table C.3: Concentration probe uncertainty [+/- (% measured value)] as a function of mass fraction and pressure for helium-air mixtures.....	125
Table C.4: Average concentration probe uncertainty for helium-air mixtures.....	125
Table C.5: Concentration probe uncertainty [+/- (% measured value)] as a function of mass fraction and pressure for methane-air mixtures.....	126
Table C.6: Average concentration probe uncertainty for methane-air mixtures.....	126
Table C.7: Concentration probe uncertainty breakdown for the case of helium mass fraction = 0.07, total pressure = 1 atm, and total temperature = 294 K.....	127
Table C.8: Data reduction code validation results for the five-hole probe.....	130
Table C.9: Effect of flow angularity on the Mach number and total pressure measurement uncertainties for gas mixtures.....	131
Table D.1: Pricing for hot-film sensors for the proposed new concentration probe.....	141

Nomenclature

Letter	Meaning
a	Speed of sound
A	Area
A_{pl}	Over-stoichiometric plume area
c	Concentration correction factor
C_d	Discharge coefficient
$C_{p\eta}, C_{p\xi}$	Pitch and roll coefficients for five-hole probe
d	Injector diameter
d_o	Orifice diameter
d_f	Hot-film diameter
d_p	Internal pipe diameter
D	Duct diameter
f	Fuel-air ratio
h_{pl}	Over-stoichiometric plume height
I_f	Hot-film current
k	Thermal conductivity
l	Active sensing length of hot-film sensor
L_c	Length for α_{\max} to reach stoichiometric
m	Mass
\dot{m}	Mass flow rate
M	Mach number
\mathbb{M}	Molecular weight
Nu	Nusselt Number
p	Static pressure
$p_a - p_d$	Peripheral port pressures for five-hole probe
p_{avg}	Average of peripheral port pressures for five-hole probe
p_{cone}	Cone static pressure
p_0	Stagnation pressure
q	Dynamic pressure
q_f	Rate of heat transfer for hot-film sensor
\bar{q}	Jet-to-freestream momentum flux ratio
r	Recovery factor for total temperature probe
R	Specific gas constant
\mathbb{R}	Universal gas constant
R_f	Hot-film heated sensor resistance
R_{lc}	Combination of probe lead and probe cable resistances for hot-film sensor
R_s	Bridge resistance
R_0	Hot-film cold sensor resistance
Re	Reynolds Number
T	Static temperature
T_0	Stagnation temperature
u	Velocity
V	Voltage

w_{pl}	Maximum width of stoichiometric limits of fuel plume
X	Cartesian coordinate in the spanwise direction
y_{CM}	Vertical distance from duct wall to fuel plume center of mass
$y_{\alpha,max}$	Vertical distance from duct wall to location of α_{max}
Y	Cartesian coordinate in the vertical direction
Z	Cartesian coordinate in the streamwise direction
α	Mass fraction
β	Diameter ratio for orifice plate flow meter
δ	Boundary layer thickness
Δ	Differential
ε	Expansibility factor for orifice plate flow meter
γ	Ratio of specific heats
μ	Dynamic viscosity
ϕ	Roll angle
ψ	Correction factor for five-hole probe
ρ	Density
θ	Pitch angle

Subscripts

Letter	Meaning
j	Jet exit property
∞	Freestream property
max	Maximum value

Superscripts

Letter	Meaning
*	Critical property (sonic condition)

Abbreviations

Letter	Meaning
CFD	Computational Fluid Dynamics
FS	Full-scale
HST	Hypersonic Wind Tunnel
NASP	National Aerospace Plane
N/A	Not Applicable
PC	Personal Computer
PID	Proportional – Integral – Derivative
RANS	Reynolds-Averaged Navier-Stokes
SLPM	Standard liters per minute
SST	Supersonic Wind Tunnel

Chapter 1: Introduction

Ever since the first known scramjet engine was developed by Antonio Ferri and others in the United States in the early 1960s¹, scramjet technology has been advancing throughout the world. Research in scramjet technology is currently ongoing in countries such as the United States, Germany, France, Japan, Italy, Australia, China, and Russia. There are many research areas related to scramjet development including topics such as structures, materials, fuel-air mixing, supersonic combustion, engine performance, engine operability limits, engine cooling, and engine-vehicle integration. The focus of this study is fuel-air mixing, which presents a significant challenge in scramjet engines.

1.1 The Scramjet Engine

The scramjet (supersonic combustion ramjet) is an airbreathing propulsion system that is being developed for hypersonic flight applications. An airbreathing engine is one that captures air from the atmosphere and uses it for fuel oxidation. In contrast, a rocket motor uses an oxidizer that is carried onboard the vehicle. Airbreathing engines have some distinct advantages for certain applications in comparison to rockets. For example, vehicles powered by airbreathing engines typically have much greater range (i.e. the vehicle can travel further distances) than vehicles powered by rockets. The range of a rocket is limited by the amount of fuel and oxidizer that can be carried onboard the vehicle, whereas the range of an airbreathing engine is only limited by the amount of fuel that can be carried onboard.

Several different types of airbreathing engines exist for operation under different flight conditions. The three main types of airbreathing engines used for aeronautical applications are turbojets, ramjets, and scramjets. Turbojets use a mechanical compressor that consists of a series of rotating blades, which is driven by a turbine located downstream of the combustion chamber. Turbojets are limited to a flight Mach number of about 3.5. One of the primary limiting factors for high-speed turbojets is the allowable turbine blade temperature. In the flight regime roughly above Mach 2, adequate compression can be achieved without a mechanical compressor and other engine cycles become feasible. For flight Mach numbers in the range of approximately 2 to 5, the ramjet cycle can be used efficiently. In contrast to a turbojet, a ramjet has no rotating

parts. Compression is achieved by capturing the incoming supersonic airflow using an inlet and slowing it to subsonic conditions. Combustion occurs at subsonic conditions and the combustion products are expanded out an exhaust nozzle creating thrust. Ramjets are limited to approximately Mach 6, when the temperature of the air entering the combustor becomes so high that combustion cannot be completed. For operation at higher flight Mach numbers than ramjets can achieve, the scramjet cycle was developed. In a scramjet, supersonic flow is maintained throughout the entire engine. Besides this fundamental difference, a scramjet is similar in concept to a ramjet. Scramjets can be used above approximately Mach 5, but below that there is in general insufficient energy in the captured airstream to enable efficient combustion in the supersonic combustor².

Scramjet engines can be used to develop hypersonic aircraft, economical and reusable launch vehicles, and hypersonic missiles. Figure 1.1 shows a diagram of a scramjet engine, which uses no rotating parts and can power vehicles at hypersonic speeds in the atmosphere.

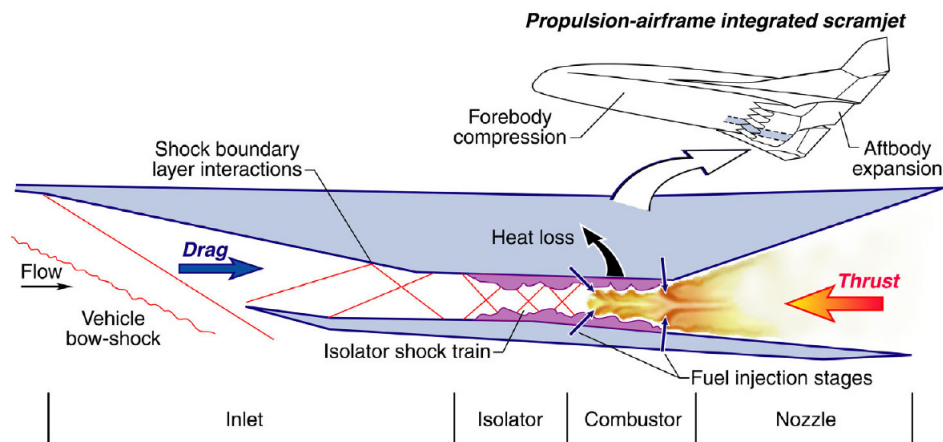


Figure 1.1: Diagram of a scramjet engine (www.nasa.gov/centers/langley)

The four major components of a scramjet engine are the inlet, isolator, combustor, and nozzle. The inlet captures and compresses high speed air from the atmosphere. This high pressure air is then ducted into the combustor. The ducting that delivers the air from the inlet to the combustor is called the isolator. Fuel is injected into the combustor and mixed with the incoming air. The fuel is then combusted and the high pressure, high temperature combustion products are expanded out the exhaust nozzle to create thrust.

1.2 Historical Background on the Scramjet

Until the beginning of the 21st century, scramjet technology had not yet advanced to the point of developing and flying a hypersonic vehicle powered by a thrust-producing scramjet engine. However, the recent successes of the X-43 and X-51 programs have demonstrated scramjet-powered flight vehicles using two different types of fuel. The X-43 was an unmanned, 3.7 meter length, hydrogen-fueled, flight vehicle that flew at Mach 9.7 under scramjet power for 10 seconds in November 2004. The X-51 is an unmanned, 7.9 meter length, hydrocarbon-fueled, flight vehicle that flew at Mach 5 under scramjet power for 200 seconds in May 2010. Prior to the flights of the X-43 and X-51, many previous scramjet research programs helped advance the technology to its current state.

Fry¹, McClinton et al.³, and Curran⁴ give detailed reviews of the historical development of scramjet engines prior to the flights of the X-43 and X-51. McClinton characterized scramjet development in the United States in terms of four generations. The first generation from 1960 - 1973 begins with the first scramjet demonstration by Ferri in 1960. During the first generation, scramjet performance was successfully demonstrated by ground tests up to Mach 7, and engine operability was studied. Hydrogen and hydrocarbon fuels were investigated in the first generation, but the primary focus was hydrogen fuel. The research focus shifted during the second generation from 1973 – 1986, when NASA focused on the engine-airframe integration of hydrogen-fueled scramjet engines on a Mach 7 hypersonic vehicle. Test facilities, test methods, and analysis methods were developed and component tests were performed to establish empirical design models. During the third generation from 1986 – 1994, the period of execution of the National Aerospace Plane (NASP) program, the research focus shifted from ground testing toward the development of the operational flight demonstrator. The NASP program was one of the most influential programs in the history of scramjet development in the United States. The program sought to develop a single-stage-to-orbit X-30 vehicle that utilized scramjet operation from Mach 5 to 25 with horizontal takeoff and landing capabilities. This was an extremely aggressive goal considering that neither scramjet engines nor flowpaths had been tested above Mach 7 before the program began. The NASP program was cancelled before the X-30 vehicle was built, but the program generated an enormous amount of scramjet engine research that

significantly advanced the state of the art. Ultimately, the NASP engine design provided the foundation for the X-43 demonstrator vehicle. After the NASP program, new research focuses emerged, which characterize the fourth generation from 1995 – today. The US Air Force began to mainly focus on hydrocarbon-fueled scramjet missiles, and this technology was recently demonstrated on the X-51 vehicle. NASA continued developing the NASP propulsion technology, which was demonstrated on the X-43 vehicle. Furthermore, research on combined cycle engines that use a scramjet cycle such as the TBCC (turbine-based combined cycle) and RBCC (rocket-based combined cycle) has become more prevalent and continues to be the focus for achieving affordable space access.

1.3 The Fuel Injection and Mixing Problem in a Scramjet

Achieving adequate fuel-air mixing is a significant challenge for scramjet engines due to the extremely fast flow-through time of the engine. At hypersonic speeds, the residence time of the air within the engine is usually on the order of 1-3 ms, during which the fuel and air must be mixed and burned². Additionally, the streamwise distance required to achieve adequate mixing can represent a significant percentage of the overall length of the engine. If the distance required to achieve adequate mixing in the combustor can be reduced, the skin-friction drag and heat transfer in the combustor will be reduced and the engine net thrust will be increased. Furthermore, to improve the overall engine efficiency, the injection process must also induce low total pressure losses.

1.4 Theoretical Background on Fuel Injection and Mixing

A large amount of research on fuel-air mixing for scramjet engines has already been performed. A review of previous research that is applicable to the current study is presented here to provide background information for the reader.

1.4.1 Mixing Enhancement

Many different injection techniques and configurations have been previously studied with the goal of enhancing the penetration and mixing of gaseous fuels. Liquid fuels can also be used in scramjet engines, but the current study involves only gaseous fuels. Proper penetration of the

injected fuel into the combustor is a necessary (but not sufficient) prerequisite for achieving adequate mixing⁵. The development of an injector configuration always requires a compromise between fuel penetration, mixing performance, and total pressure losses. Some of the different injector configurations that have been previously studied are shown in Figure 1.2 including wall jets, struts^{6,7}, and swept ramps^{8,9}. Different orifice shapes and arrangements that have been investigated primarily in wall jet configurations include circular injectors^{10,11,12}, wedge injectors¹³, diamond injectors^{14,15}, elliptical injectors^{16,17}, streamwise elongated slots^{18,19}, spanwise elongated slots²⁰, and aerodynamic ramps^{21,22,23}. Extensive reviews of mixing enhancement techniques for scramjet engines that include discussions of many of these different injector configurations are given by Schetz et al.²⁴, Kutschenreuter⁵, and Seiner et al.²⁵.

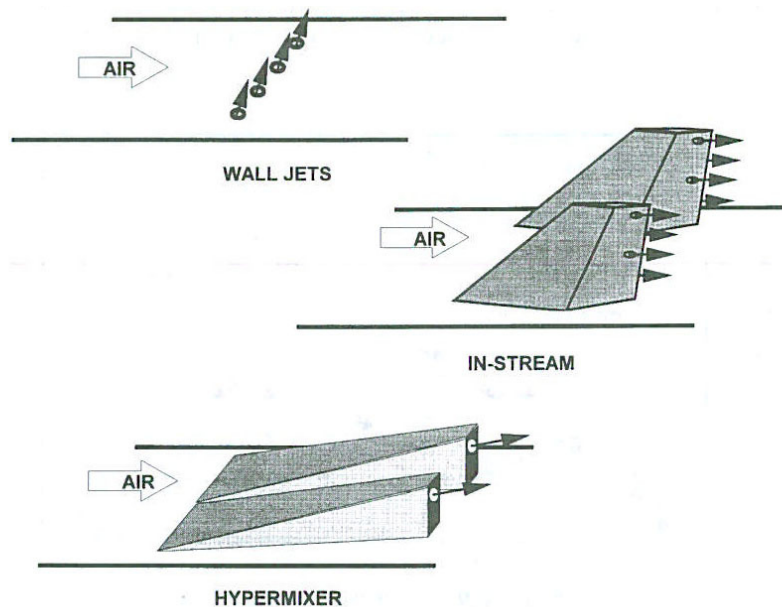


Figure 1.2: Examples of various injector configurations (from Kutschenreuter⁵)

One way injectors are classified is based upon whether the design is intrusive to the combustor (e.g. struts, ramps, fins, etc.) or non-intrusive (e.g. wall jets) although there are many different variations of both types. For use in scramjet combustors, flush-walled injectors are often preferred over in-stream injectors because they minimize total pressure losses, heating, and drag. However, some engine designs (e.g. a circular combustor cross-section) may require the use of in-stream injectors in order to obtain adequate distribution of the fuel across the combustor.

The angle at which a fuel is injected into a combustor is another key consideration. For instance, a fuel can be injected parallel or normal to the streamwise direction of the combustor. Parallel injection is generally characterized by relatively slow mixing which results in increased combustor length, but also low total pressure losses. Normal injection usually results in relatively fast mixing, but significant total pressure losses. However, often an angle in between that of parallel and normal injection is chosen as a compromise. Mays et al.²⁶ studied low-angled transverse injection of helium at sonic conditions into a Mach 3 crossflow for injectors angled at 15° and 30° relative to the freestream direction. This study found that the injection angle changed the level of initial mixing, but not the rate of downstream mixing. Moreover, despite the low injection angles, good crossflow penetration was found. McClinton¹¹ investigated transverse injection of hydrogen at sonic conditions at angles of 30°, 45°, 60°, and 90° into a Mach 4 crossflow. The results of this study found that as the injection angle decreased from 90° to 30°, total pressure losses decreased without sacrificing the amount of far field penetration or mixing. Both of these studies show results that favor the use of low injection angles.

1.4.2 Non-Dimensional Injection Parameters

There are a number of non-dimensional parameters that characterize the injection process. These parameters generally describe operating conditions and are sometimes used to compare experiments that are run at different conditions or with different facilities. One of the most useful parameters for correlating transverse jet injection results is called the jet-to-freestream momentum flux ratio, \bar{q} , defined as follows:

$$\bar{q} \equiv \frac{q_j}{q_\infty} = \frac{(\rho u^2)_j}{(\rho u^2)_\infty} = \frac{(p\gamma M^2)_j}{(p\gamma M^2)_\infty} \quad (1.1)$$

Empirical data shows that the initial penetration of the fuel jet produced by circular transverse injectors is proportional to $\bar{q}^{0.5}$ (refer to Section 1.4.8). This is an important correlation, since good penetration is a prerequisite for good mixing. As \bar{q} increases for circular injectors, initial penetration of the fuel jet increases. This effect can be explained by the momentum increase that occurs in the transverse direction as \bar{q} increases. A value of $\bar{q} \approx 2$ has been shown to give good performance for circular wall injectors operating at sonic conditions¹⁴.

Other useful parameters for correlating transverse jet injection results include the velocity ratio (u_j / u_∞), density ratio (ρ_j / ρ_∞), and fuel-air ratio (\dot{m}_f / \dot{m}_a). The velocity ratio and density ratio influence the development of shear layers in which the two fluids mix. Specifically, how the velocity ratio compares to 1 (i.e. is u_j / u_∞ greater than, less than, or equal to 1) is critical as the velocity difference ($u_j - u_\infty$) influences the development of shear layers and large turbulent structures that promote mixing. Therefore, if u_j / u_∞ is close to 1, the conditions for mixing are poor.

1.4.3 Flow Features of Transverse Jets in Supersonic Flow

The current study involves underexpanded transverse jets in supersonic crossflow. An underexpanded jet is characterized by a higher pressure at the nozzle exit than the ambient pressure (i.e. back pressure). Therefore, the flow is capable of additional expansion after leaving the jet nozzle. The flow features of underexpanded transverse jets in supersonic flow are rather complicated and have been studied extensively both experimentally and numerically^{20,27,28}. Figure 1.3 illustrates the general flow features of an underexpanded, circular transverse jet in supersonic crossflow. The disturbance of the crossflow results in the creation of a three-dimensional bow shock surrounding the jet. The bow shock interacts with the approaching turbulent boundary layer producing a region of separated flow upstream of the injector exit. As the jet expands out of the injector nozzle, the injectant plume rapidly bends toward the downstream direction. A system of shock waves forms in the injectant plume consisting of both a barrel shock and a Mach disk. Several different types of vortices also develop in the injectant plume and contribute to the mixing that occurs between the jet and the crossflow. The large scale vortical structure that develops in the injectant plume is referred to as the counter-rotating vortex pair (CVP), which significantly enhances the mixing process.

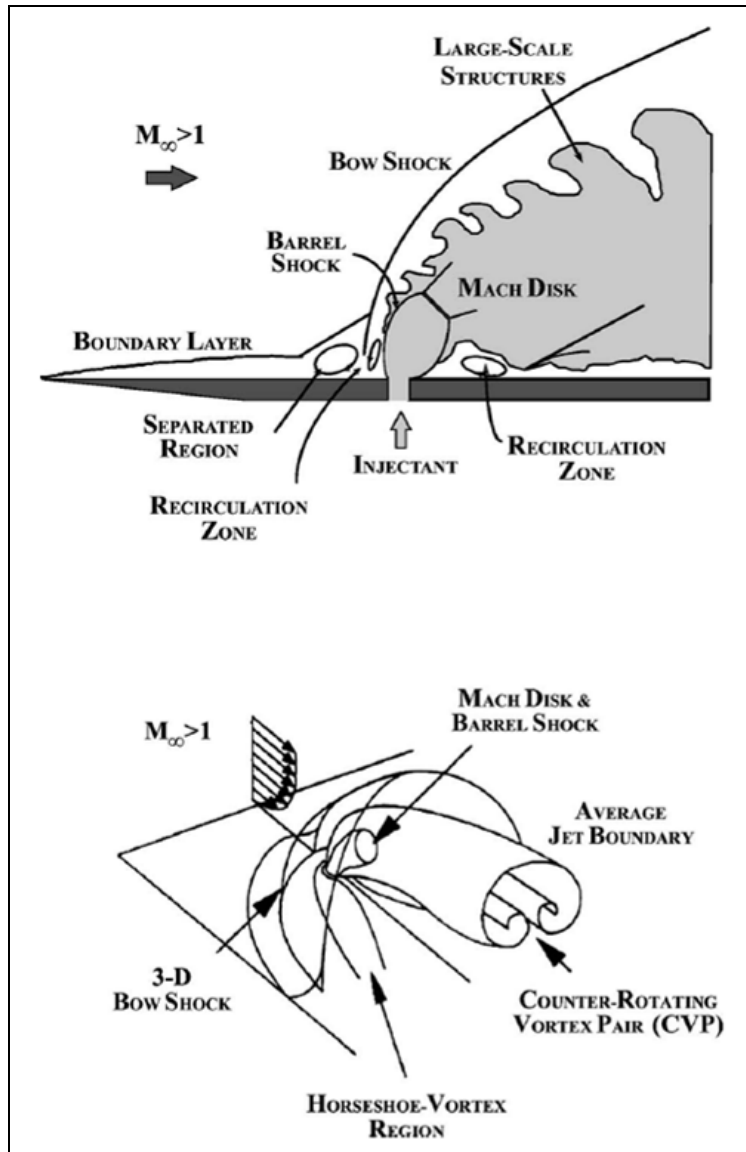


Figure 1.3: Flow features of an underexpanded transverse jet in supersonic flow [from Ben-Yakar et al.²⁹ (top) and Gruber et al.³⁰ (bottom)]

1.4.4 Fuel Selection Considerations

The fuels that are primarily being considered for use in scramjet engines include hydrogen and several hydrocarbons (mainly JP-7 and JP-10). In comparison to hydrocarbon fuels, hydrogen offers better energy release per unit mass of fuel, shorter ignition delay time, and better heat sink capacity for engine cooling considerations. Furthermore, hydrogen-fueled scramjet engines are capable of operating at significantly higher Mach numbers than hydrocarbon-fueled scramjet engines. Figure 1.4 shows a comparison of the operating envelopes for airbreathing engines that

are hydrogen-fueled vs. hydrocarbon-fueled. The main disadvantage of hydrogen fuel is its low density, which effectively restricts the use of hydrogen fuel to large vehicles. Thus, hydrogen fuel is generally considered for use in space launch applications, whereas hydrocarbon fuels are typically considered for missiles and responsive aircraft.

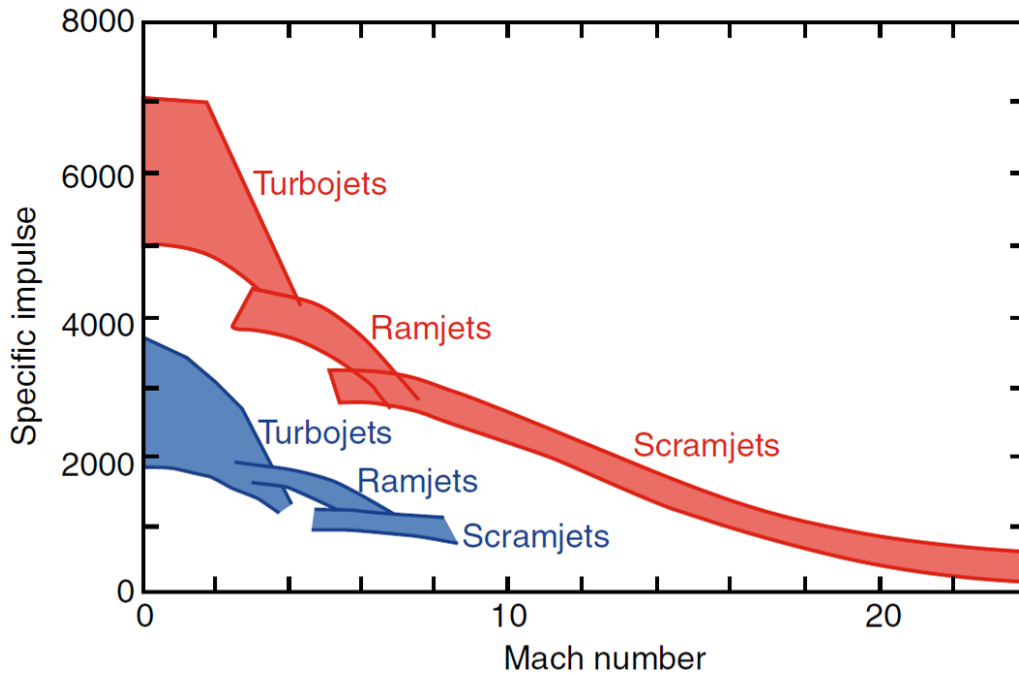


Figure 1.4: Airbreathing engine operating envelopes for hydrogen fuel (red) vs. hydrocarbon fuel (blue) [from Van Wie et al.²]

1.4.5 Combustor Design Considerations

There are a number of important factors to consider when designing an array of injectors for a scramjet combustor. One crucial factor is the amount spacing between neighboring injectors. If the injectors are spaced too closely together, mixing will be inhibited. Slow mixing results in increased combustor length, because a long distance is required to achieve adequate mixing. Schetz et al.²⁴ found that the critical value for the spacing of transverse injectors is about 9 injector diameters from center to center. Spacing below this critical value can reduce the downstream mixing rate by a factor of two. A second important factor that must be considered is the overall combustor length that is required based upon the mixing behavior of the injectors. A measure of the required combustor length is the length required for complete mixing (L_c), which is defined as the streamwise distance from the injection position to the point at which the maximum injectant mass fraction (α_{max}) in the plume reaches the stoichiometric value.

1.4.6 Boundary Layer Effects

The conditions of the boundary layer at the jet injection location can have significant influences on the fuel-air mixing process as viscous effects are dominant in the near-wall region. Theoretical indications are that the jet must penetrate significantly through the boundary layer and into the freestream flow in order to create the strong vortices that enhance the mixing process³¹. There have been very few systematic experimental studies of the effects of boundary layer thickness on jet injection flowfields. For these types of studies, the wall boundary layer thickness (δ) is usually non-dimensionalized in terms of the injector diameter (d). High values of δ/d are of interest, since these conditions are representative of the combustor conditions for scramjet-powered vehicles.

One effect that available experimental studies^{31,32} agree upon is that as δ/d increases, penetration of the jet in the near field region increases. The explanation for this effect is that the wall boundary layer locally increases the jet-to-freestream momentum flux ratio (\bar{q}), which in turn increases the initial penetration of the jet. As the jet becomes more axial, other mixing mechanisms (i.e. shear layer development) dominate, therefore the initial boundary layer thickness effect is less noticeable in the far field³³.

1.4.7 Performance Characterization

Over time, researchers have developed different methods for characterizing the performance of scramjet injectors. Calculations are often performed that assess the levels of mixing, penetration, plume area, and total pressure losses for an injector configuration. The rate of decay of the maximum injectant mass fraction, α_{max} , is one measure of mixing performance as this has direct implications on the required combustor length. The amount of penetration of the fuel plume is often described by either: (1) the location of the maximum injectant mass fraction in the plume relative to the combustor wall or (2) the location of the center of mass of the injectant in the plume relative to the combustor wall. Here, $y_{\alpha,max}$ is the vertical distance from the duct wall to the location of α_{max} , and y_{CM} is the vertical distance from the duct wall to the center of mass of the injectant in the plume. Calculations of the fuel plume area give a measurement of the fuel coverage across the combustor cross-section. These calculations are usually performed using the

stoichiometric ratio of the fuel as a metric. For instance, A_{pl} is defined as the over-stoichiometric plume area. Another measure of the plume size is the plume width (w_{pl}), defined as the maximum width of the stoichiometric limits in the plume.

1.4.8 Empirical Correlations

Some rough, but useful empirical correlations have been developed to approximate the penetration and mixing of transverse jets in high-speed flows. Schetz et al.²⁴ developed the following empirical correlation for the mixing of transverse jets in unconfined flows:

$$\alpha_{\max} \approx \left(\frac{x}{d} \right)^{-n} \quad (1.2)$$

where x is the distance downstream of the injector, d is the injector diameter, and $n \approx 0.8$. Higher values of n indicate faster mixing. Furthermore, the stoichiometric intercept for transverse injectors is usually in the range of $x = 200d$, which provides a basis for preliminary comparison of different injector configurations.

Cohen et al.³⁴ and Billig et al.³⁵ developed the following correlation for the penetration of circular transverse injectors in terms of the distance of the Mach disk from the wall:

$$\left(\frac{y_{disc}}{d} \right) \propto \bar{q}^{0.5} \quad (1.3)$$

where y_{disc} is the height of the Mach disk above the wall, d is the injector diameter, and \bar{q} is the jet-to-freestream momentum flux ratio. Billig et al.³⁵⁻³⁶ also developed a robust code called JETPEN to predict the mixing and penetration of transverse jets based on a semi-empirical analysis. JETPEN assumes that the injectors are in an unconfined flow.

In addition to the empirical relations presented here, many more complex empirical correlations for the mixing of high-speed flows have also been suggested by other researchers.

1.5 Motivation for the Current Research

In order to develop improved injection systems for scramjet engines with enhanced penetration and mixing, current levels of understanding and prediction capabilities for high-speed mixing flows must continue to be improved. The accuracy and uncertainty of Computational Fluid

Dynamics (CFD) predictions for these complex flows needs significant improvement. One way to achieve significant improvements in the CFD predictions is to expand the applicability of the turbulence models in the current CFD codes. A primary motivation for the experiments that were run for this study was to provide support for CFD turbulence model upgrades. The experiments will extend the database of high-speed mixing studies that is available for CFD code validation. In addition, the experiments sought to fill in gaps in the available database of high-speed mixing studies by targeting research areas that needed further investigation.

A large number of high-speed mixing studies for scramjet engines are available in the literature, but the effects of confinement within a duct on the mixing process in most of these studies have been insignificant. However, actual scramjet combustors are confined ducts, and one can expect that the effects of such confinement are very large. For instance, there are bow shocks created by the injection process itself. These bow shocks can reflect off combustor walls and interact with the jet plume downstream or if there is an array of injectors present, the bow shocks from multiple injectors can interact. If struts that protrude into the combustor are used for fuel injection, a highly complex 3-D flowfield is likely to develop in the combustor with multiple shock interactions. Thus, the effects of confinement are an important element in the fuel-air mixing process for scramjet combustors, and this area is in need of further study. Additionally, state of the art scramjet engines utilize circular cross-section combustors, so experiments that study these designs should be run in circular ducts.

To investigate the effects of confinement within a circular duct on the mixing process, two state of the art injector models for circular scramjet combustors were developed. Both injector models are based upon a circular duct diameter of 100 mm, which makes the models approximately full-scale for the size of a hypersonic missile engine. Each model has an array of inclined circular injectors, which are confined within a constant area circular duct. One model uses a non-intrusive injector design consisting of an array of flush-wall injectors that are evenly distributed around the wall of a circular duct. The second model uses an intrusive injector design consisting of four struts, which are confined within a circular duct. The injector models were designed to attach directly to the end of an axisymmetric, high-speed wind tunnel nozzle (creating a constant area duct) for testing.

Testing of the injector models was performed under cold-flow (non-combusting) conditions. The general goals of cold-flow studies of injection and mixing in simulated scramjet combustors are first to assess the penetration and mixing of the simulated fuel jets in comparison with the expectations upon which the injector arrangement was designed. Such designs are usually created using either CFD or empirical data and semi-empirical analyses. A second goal is to quantify the uncertainty of CFD predictions for such an injector design under cold-flow conditions, so that the reliability of CFD predictions for hot-flow, combusting conditions can be judged. Detailed experimental flowfield studies are extremely challenging under the hot-flow conditions of interest, so often the designer must rely on CFD. In this research, a third and perhaps the most important goal of the experiments is to aid in refining the turbulence modeling. Cold-flow experiments are better for achieving this goal than combustion experiments, because the effects of the turbulence modeling are better isolated when CFD is used to simulate a cold-flow experiment. When CFD is used to simulate a combustion experiment, both turbulence modeling and combustion chemistry modeling assumptions must be made. For the cold-flow case, the combustion chemistry modeling assumptions are not necessary, therefore the turbulence modeling can be better isolated for improvement.

The effects of injectant molecular weight on the gaseous fuel-air mixing process represents another area that has been identified as needing further research. Early benchmark experiments by NASA³⁷ and other researchers³⁴ in this area likely suffered from selective sampling problems (refer to Section 2.3.4 and reference 24 for additional details) and few experiments have been conducted in this area since then. To investigate the effects of injectant molecular weight, three different injectants were chosen for the current study: helium (molecular weight = 4), methane (molecular weight = 16.04), and air (molecular weight = 28.97). The use of helium as an injectant safely simulates hydrogen fuel, which was demonstrated by Torrance³⁷. Torrance established that the penetration and mixing of helium and hydrogen are nearly the same in cold-flow mixing studies with equivalent dynamics pressure ratios. Methane and air were chosen because these gases have molecular weights that are higher than helium. Methane was not selected because of its properties as a hydrocarbon fuel. Nevertheless, better understanding of the effects of injectant molecular weight will contribute to better understanding of the mixing behavior of heavy hydrocarbon fuels such as JP-7 and JP-10.

Another area that has been identified as needing further research is the effects of freestream Mach number on the fuel-air mixing process. To investigate these effects, experiments were run that independently varied the freestream Mach number. Comparable experiments were run at nominal Mach numbers of 2 and 4.

With the previously discussed issues in mind, an integrated experimental and computational research program was formulated. The computational side of the program sought to upgrade the turbulence models that are used for CFD predictions of the flow inside a scramjet combustor. The experimental side of the program sought to provide data to support the computational side, while also filling in gaps in the available database of high-speed mixing experiments. This dissertation presents the results of a set of experiments that were performed for this program at Virginia Tech. The computational side of this program was run by CRAFT Tech (Combustion Research and Flow Technology) in Pipersville, PA. For additional information on the turbulence model upgrades being investigated by CRAFT Tech, refer to references 38, 39, and 40.

Chapter 2: Experimental Methods

2.1 Test Facilities

Three Virginia Tech wind tunnel facilities were used for the current study including the hypersonic wind tunnel, the supersonic wind tunnel, and the supersonic free-jet facility. All mixing experiments were performed in the hypersonic wind tunnel. The supersonic wind tunnel and supersonic free-jet facility were used for instrument calibration procedures.

2.1.1 Hypersonic Wind Tunnel Facility

The Virginia Tech hypersonic wind tunnel shown in Figure 2.1 is a blow-down type facility, which operates at speeds ranging from Mach 2 to 7. The Mach number conditions for the facility are set through the use of interchangeable nozzles. Air (or other working gas) is supplied from a compressor to charge the storage bottles visible within the support frame for the tunnel. A special fast-acting control valve initiates flow into the plenum chamber. The flow then passes through an axisymmetric, converging-diverging nozzle and out through the diffuser. Figure 2.2 shows the shape of one of the hypersonic tunnel nozzles and the coordinate system associated with the tunnel. The nozzle exit diameter is 100 mm. Run times for the facility are typically in the range of 1-3.5 seconds. Due to the working principle of the tunnel and the fast-acting control valve, there is a gradual decrease in total pressure during the run. The variation in the total pressure during a run is in the range of approximately 10%. However, the average value of the total pressure during a run is repeatable to within approximately +/- 1% from run to run. Figures 2.3 and 2.4 show plots of the total pressure during typical 3.2 second runs at Mach numbers 2 and 4, respectively. For Mach numbers above 4, an electric heater raises the total temperature up to 800 K to prevent liquefaction.

From Figures 2.3 and 2.4, it is evident that the tunnel requires a finite amount of time to start up and shut down. During a typical 3.2 second run, about 1 second is required for the tunnel to start up and shut down. Measurements are not taken during start up and shut down, because the tunnel is not operating supersonically during these time intervals.

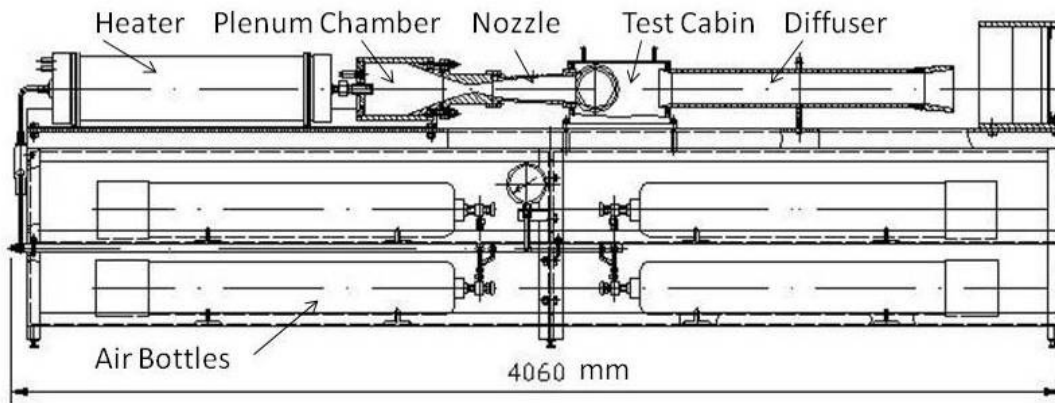


Figure 2.1: Virginia Tech hypersonic wind tunnel facility

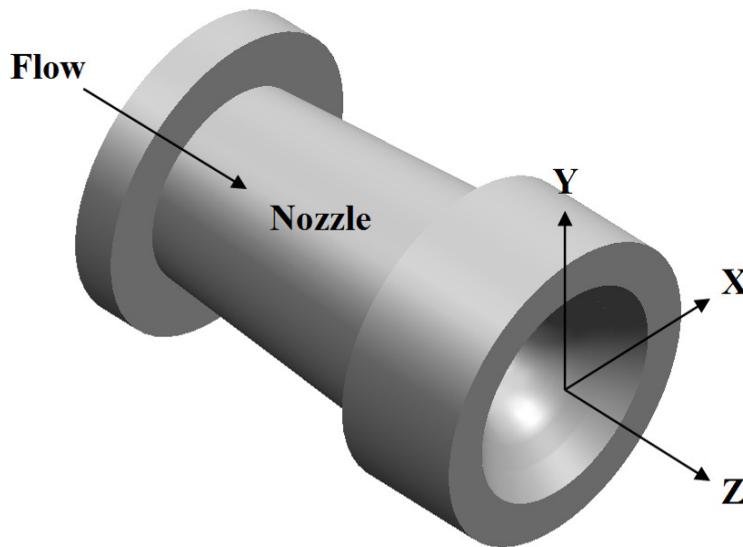


Figure 2.2: Coordinate system associated with the hypersonic tunnel

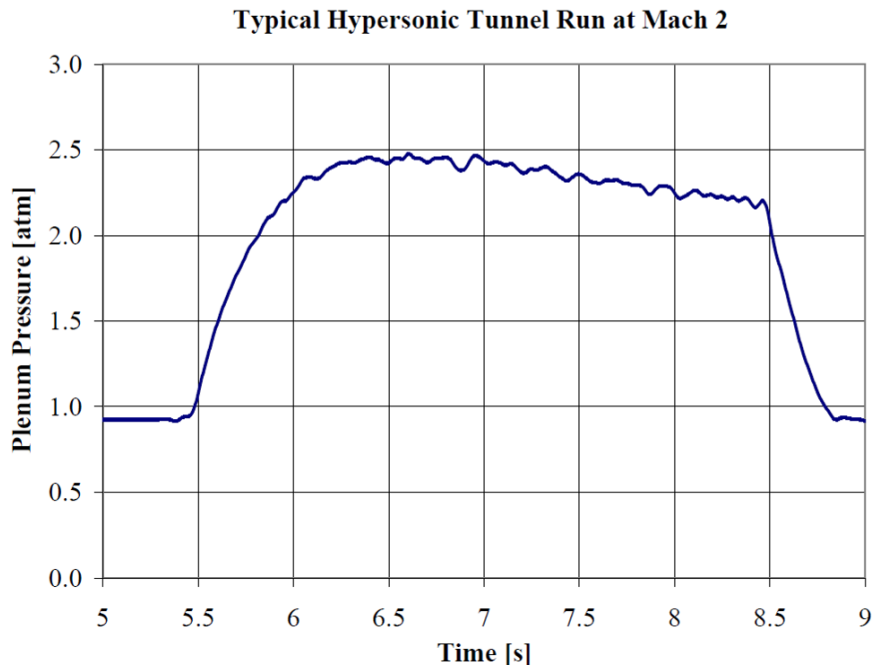


Figure 2.3: Variation of total pressure during hypersonic tunnel run at Mach 2

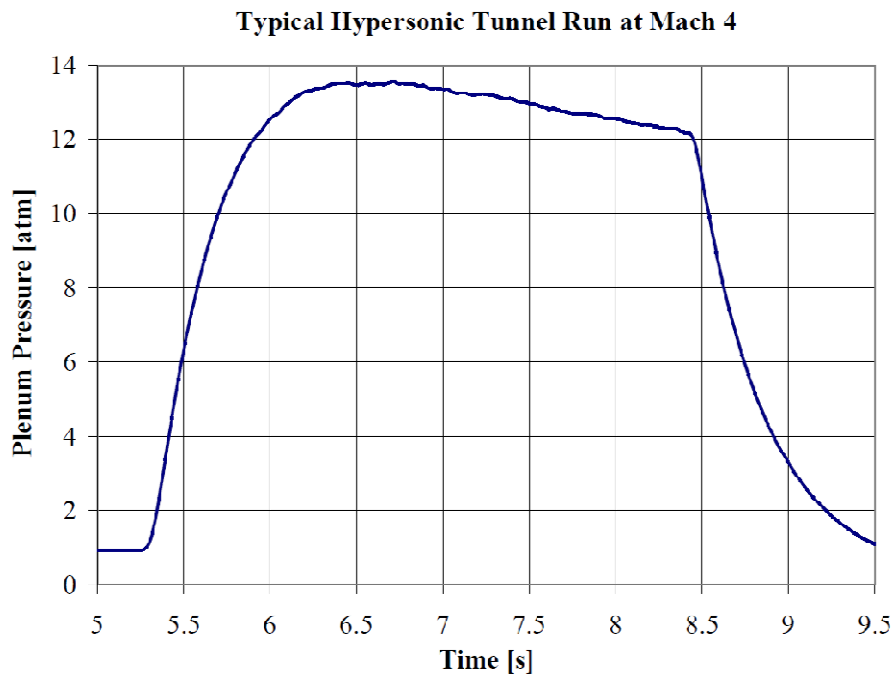


Figure 2.4: Variation of total pressure during hypersonic tunnel run at Mach 4

2.1.1.1 Data Acquisition and Tunnel Control

An integrated group of LabVIEW programs was used to control all aspects of the experiments including: operation of the wind tunnels, operation of an injectant supply system, the position of a traverse system, and data acquisition. Measurements were taken using various probes located inside the test cabin. Additionally, measurements were taken for the injectant mass flow rate, the plenum pressure of the tunnel during a run, and the pressures located at various positions in the injection system. Data was sampled at 500 Hz and recorded on a PC with a 16-channel, 16-bit A/D converter and a 64-channel multiplexer both with a built-in cold-junction compensator for temperature measurements. Due to the response times associated with the different probes, certain settling times have to be administered to reach steady state readings of the transducers during a run. For example, three of the probes that were used (the concentration, cone-static, and triple-rake probes) had to be paused for 200 ms at each data point, whereas another probe (a fast-response, conical five-hole probe) only needed to be paused for 50 ms at each data point.

2.1.1.2 Boundary Layer Measurements

Boundary layer measurements for the hypersonic wind tunnel were performed in order to characterize the test conditions and to validate CFD models for the flow through the Mach 2 and Mach 4 nozzles of the tunnel. The measurements were performed at the exit of each nozzle along the centerline by traversing a probe through the boundary layer and measuring discrete data points. The triple-rake probe, which was used for the boundary layer measurements, is further described in Section 2.3.6, and the traverse system that was used to position the probe is described in section 2.3.3. The triple-rake probe consists of a Pitot probe, a cone-static probe, and a total temperature probe in a rake configuration. The boundary layer measurements necessary for CFD validation purposes only required the use of the Pitot and cone-static probes. Using the Pitot probe, the boundary layer thickness of the flow at the exit of each nozzle was determined. Then by using a combination of the data from both the Pitot probe and the cone-static probe, the Mach number profile at the exit of each nozzle was determined. The method used to solve for Mach number is described in Appendix A and requires the use of normal shock relations and the Taylor-Maccoll solution for a sharp cone.

The results of the boundary layer measurements for the hypersonic tunnel are shown in Figures 2.5 – 2.8. In these figures, the Pitot pressure data is normalized with the freestream total pressure, which varies during the run and also varies from run to run. According to the Pitot pressure data, the boundary layer thickness is approximately 3 mm at the exit of the Mach 2 nozzle and approximately 7 mm at the exit of the Mach 4 nozzle. According to the Mach number data, the freestream Mach number is approximately 2.00 at the exit of the Mach 2 nozzle and approximately 3.87 at the exit of the Mach 4 nozzle. The uncertainty associated with the normalized Pitot pressure data was found to be approximately +/- 0.9% of the measured value, whereas the uncertainty associated with the Mach number data was found to be approximately +/- 1.1% of the measured value. An uncertainty analysis for the boundary layer measurements is presented in Appendix C.

$Y / D = 0.5$ represents the duct wall location and $Y / D = 0$ represents the duct centerline

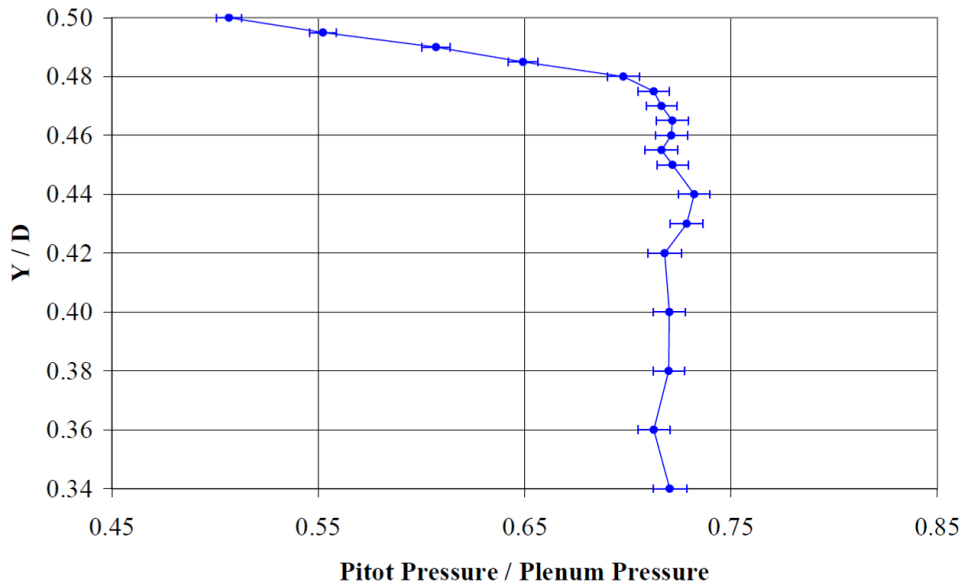


Figure 2.5: Pitot pressure profile at the exit of the Mach 2 nozzle for the hypersonic tunnel

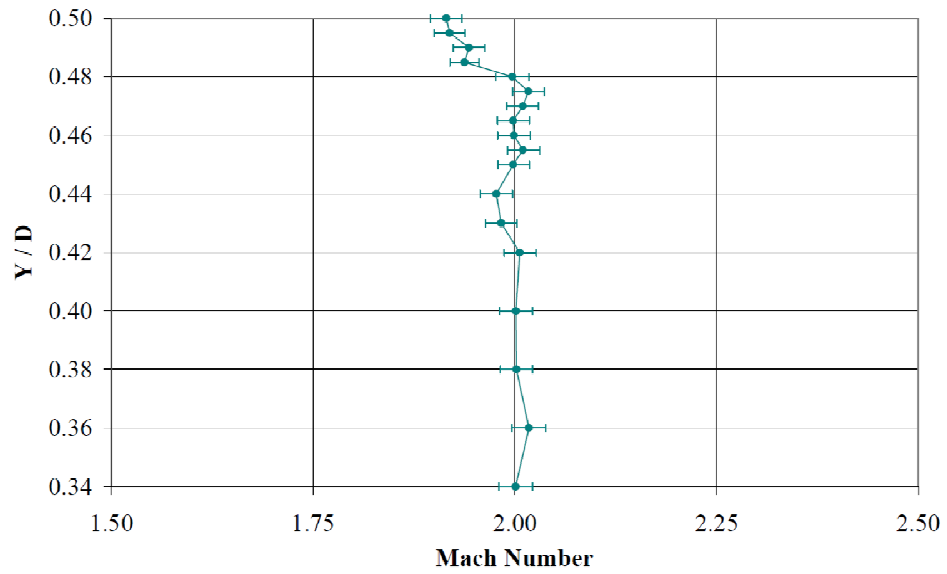


Figure 2.6: Mach number profile at the exit of the Mach 2 nozzle for the hypersonic tunnel

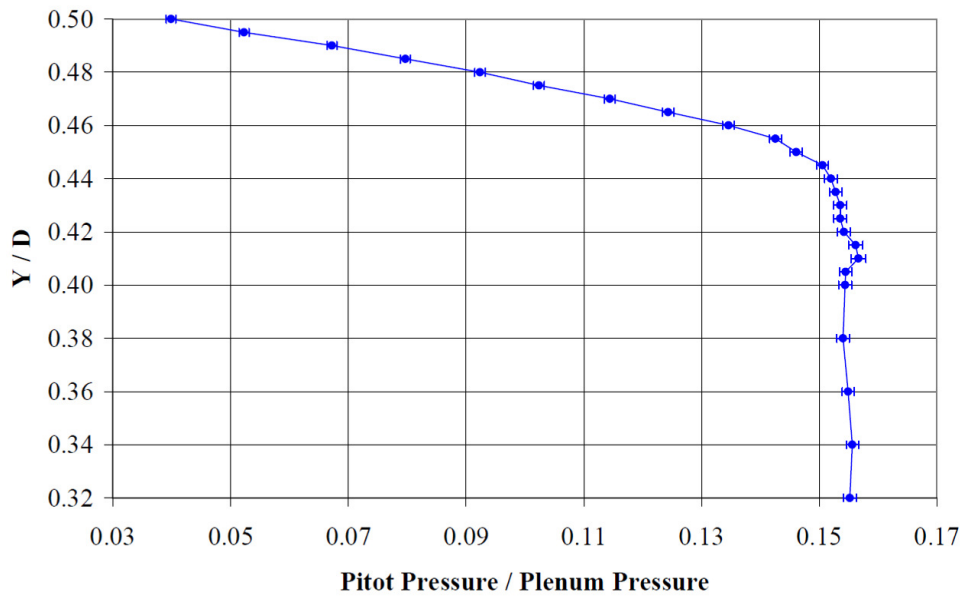


Figure 2.7: Pitot pressure profile at the exit of the Mach 4 nozzle for the hypersonic tunnel

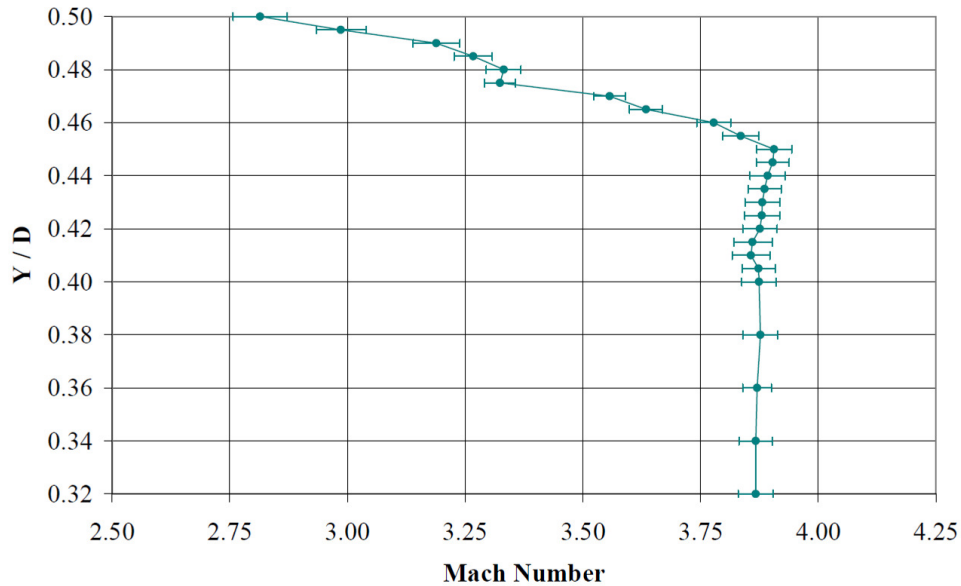


Figure 2.8: Mach number profile at the exit of the Mach 4 nozzle for the hypersonic tunnel

2.1.2 Supersonic Wind Tunnel Facility

The Virginia Tech supersonic wind tunnel shown in Figure 2.9 is a blow-down type facility that has a 23 cm x 23 cm test section. The Mach number conditions for the facility are set through the use of interchangeable two-dimensional, converging-diverging nozzles. Nozzles are available for Mach numbers of 2.4, 3, and 4. For the instrument calibration procedures, the Mach 2.4 and 4 nozzles were used. A compressor along with a drying and filtering system provide the air supply for the tunnel. Air is stored in two tanks with a total volume of 23 m³. During a wind tunnel run, air is released from the tanks, passes through a quick opening butterfly valve, then through a hydraulically actuated pressure regulating valve, and then passes into the settling chamber, test section, and out through the diffuser. Run times are typically about 20 seconds, but can vary from 8-60 seconds depending on run conditions. Through the use of PID (Proportional – Integral – Derivative) control, the total pressure during a run is maintained constant within approximately +/- 1%.

2.1.3 Supersonic Free-Jet Facility

The Virginia Tech supersonic free-jet facility shown in Figure 2.10 operates at Mach 3.1 and is primarily used for the calibration of different types of flow measurement probes. The facility

consists of a solenoid on/off valve, pressure regulator, plenum chamber, and nozzle. The nozzle is an axisymmetric, converging-diverging design with an exit diameter of 25.4 mm. The facility uses the same air supply as the supersonic wind tunnel and is capable of operating continuously if the compressor is left on during the run. The continuous operating capability of this facility allows a large number of calibration points to be measured during probe calibrations.

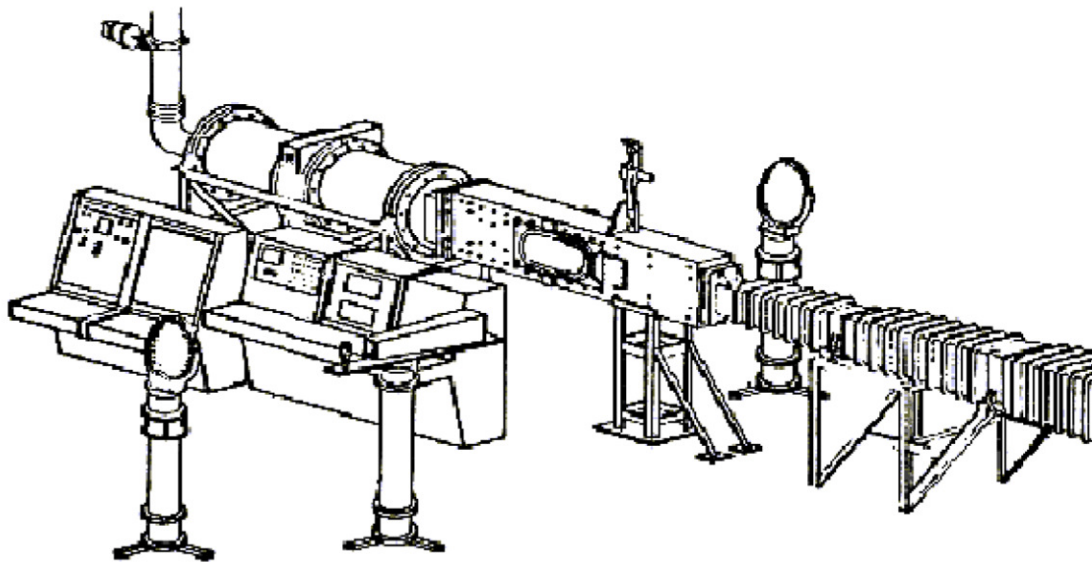


Figure 2.9: Virginia Tech supersonic wind tunnel facility

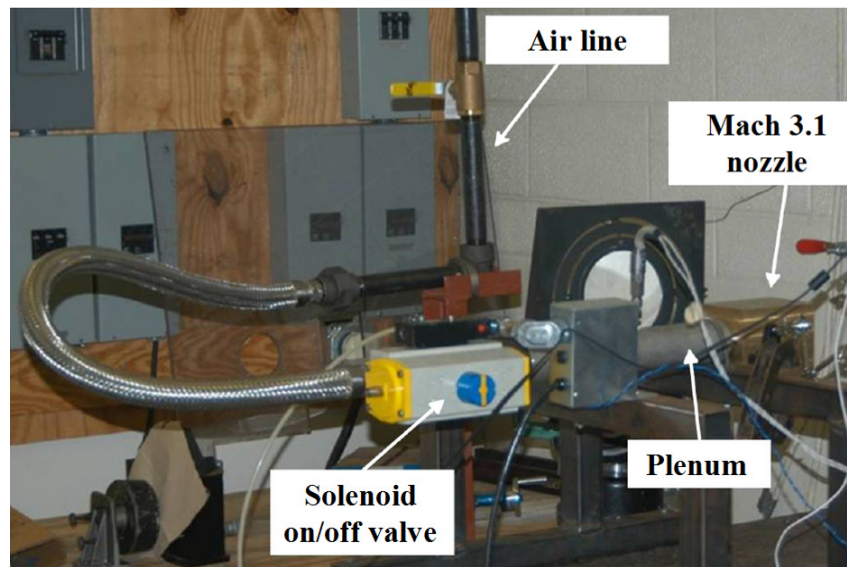


Figure 2.10: Virginia Tech supersonic free-jet facility

2.2 Test Models

Test hardware was developed to simulate the fuel injection process for a scramjet engine with a circular cross-section combustor. Two different injector models, a flush-wall injector model and a strut injector model, were developed based on state of the art scramjet engine designs. The injector models are approximately full-scale for the size of a scramjet missile engine. To provide a supply of fuel to the simulated injectors, an injection system was developed that is capable of controlling the mass flow rate of different types of gases.

2.2.1 Flush-Wall Injector Model

The flush-wall injector model connects directly to the end of the hypersonic tunnel nozzle, which creates a constant area duct of length 270 mm (2.7 duct diameters) that extends from the nozzle exit until the duct comes to an end in the test section. A picture of the flush-wall injector model fitted to the hypersonic wind tunnel is shown in Figure 2.11. The injector model has an array of 16 round, sonic injectors distributed evenly around the wall of the duct (with an angular spacing of 22.5° between injectors). A picture of the array of injectors within the injector model is shown in Figure 2.12. The injectors have a diameter of 2.06 mm and are located in a single axial plane that is 100 mm downstream of the end of the nozzle. The injectors are connected to a circumferential plenum chamber and a gas (helium, methane, or air) is injected at an angle of 30° relative to the streamwise axis of the duct. For the flush-wall injector model, a plane 172.3 mm (83.6 injector diameters or 1.72 duct diameters) downstream of the circular injector centers was selected for data measurement purposes. The injector model was designed using empirical background information and the JETPEN³⁵⁻³⁶ code, which is a semi-empirical analysis that assumes the injectors are isolated and in an unconfined flow.

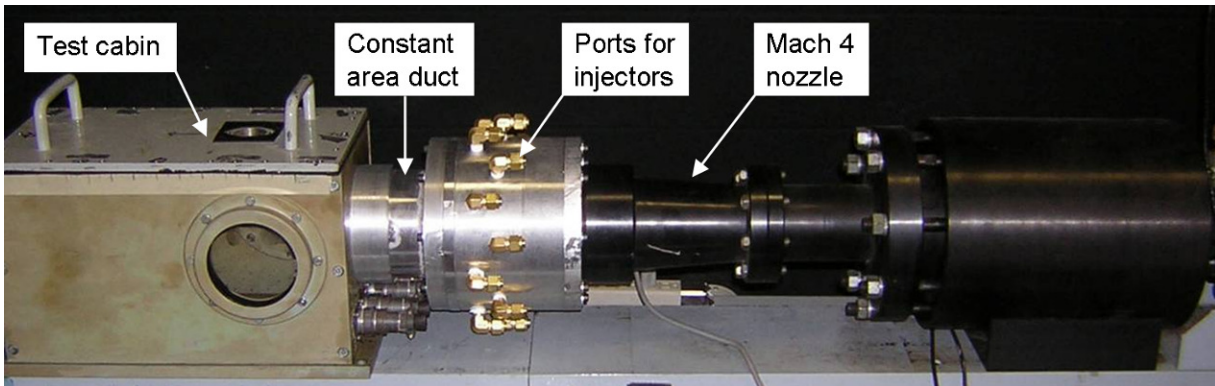


Figure 2.11: Picture of the flush-wall injector model fitted to the hypersonic wind tunnel (flow is from right to left)

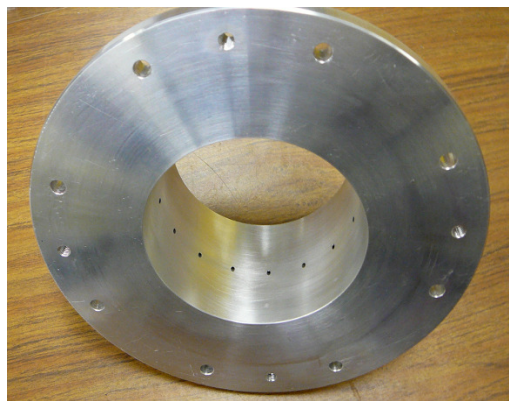


Figure 2.12: Picture of the flush-wall injector array (looking upstream)

2.2.2 Strut Injector Model

The strut injector model also connects directly to the end of the hypersonic tunnel nozzle and is designed to be a cylindrical duct extension of the wind tunnel nozzle. The model has an overall length of 270 mm (2.7 duct diameters). The model contains four slender, inclined struts with a total of 16 round, sonic injectors. Figure 2.13 shows a picture of the strut injector model. The struts have a width of 8.2 mm; they start at the front of the extension duct (i.e. the end of the tunnel nozzle) and extend 148 mm in the flow direction with an inclination of 10° . Two 1.52 mm diameter circular injectors on each lateral side of each strut create jets that penetrate into the tunnel crossflow at an angle of 30° relative to the streamwise axis of the duct. The centers of the injectors are located 92 mm from the leading edge of each strut. For the strut injector, a plane 180.5 mm (119 injector diameters or 1.81 duct diameters) downstream of the circular injector centers was selected for data measurement purposes. The generic strut injector model was designed at Johns Hopkins Applied Physics Lab (APL), and the design was provided to Virginia

Tech for experimental evaluation. The number, shape, and size of the struts were based on drag considerations and the previous experience of APL. The number, size, and location of the injectors were based on CFD studies.

As was discussed in Chapter 1, the development of a scramjet injection system always requires a compromise between fuel penetration, mixing performance, and total pressure losses. High total pressure losses are unavoidable in this configuration due to the physical obstacle created by the struts. In order to remain competitive with other geometries, a design such as this one must compensate for this disadvantage by achieving better fuel penetration and mixing performance.

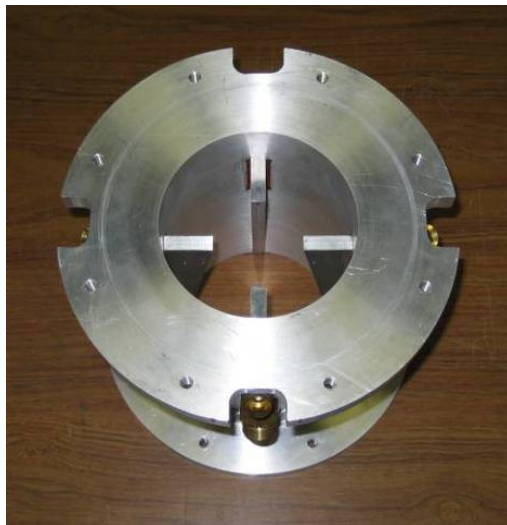


Figure 2.13: Picture of the strut injector model (looking upstream)

2.2.3 Injectant Supply System

To provide a supply of injectant to the simulated injectors, an injection system was developed to accurately control the mass flow rate of the gas being injected. Three different configurations of the injection system were used for the experiments, which are shown in Figures 2.14 – 2.16. Due to the differences in the design of the flush-wall injector model and the strut injector model, each injector model required a slightly different configuration of the injection system. Additionally, the method used to control the injectant mass flow rate was improved after several test campaigns. Initially, an orifice plate flow meter (see Section 2.3.2) was used to measure the mass flow rate of the injectant, and control within +/- 5% of the desired mass flow rate was achieved with this system. To obtain better control over the injectant mass flow rate, the

injection system was redesigned to replace the orifice plate flow meter with a system of two digital mass flow controllers (see Section 2.3.1). A system of two mass flow controllers was chosen, because a single mass flow controller was not capable of supporting the required mass flow rate for the experiment. Using the mass flow controllers, control of the injectant mass flow rate within $\pm 3\%$ of the desired value was achieved. The mass flow controllers were used for the bulk of the experiments (7 out of 9 experimental cases). The following is a summary of the three different configurations of the fuel injection system that were used for the experiments:

1. Flush-wall injector model configuration using an orifice plate flow meter (shown in Figure 2.14)
2. Flush-wall injector model configuration using a system of two digital mass flow controllers (shown in Figure 2.15)
3. Strut injector model configuration using a system of two digital mass flow controllers (shown in Figure 2.16)

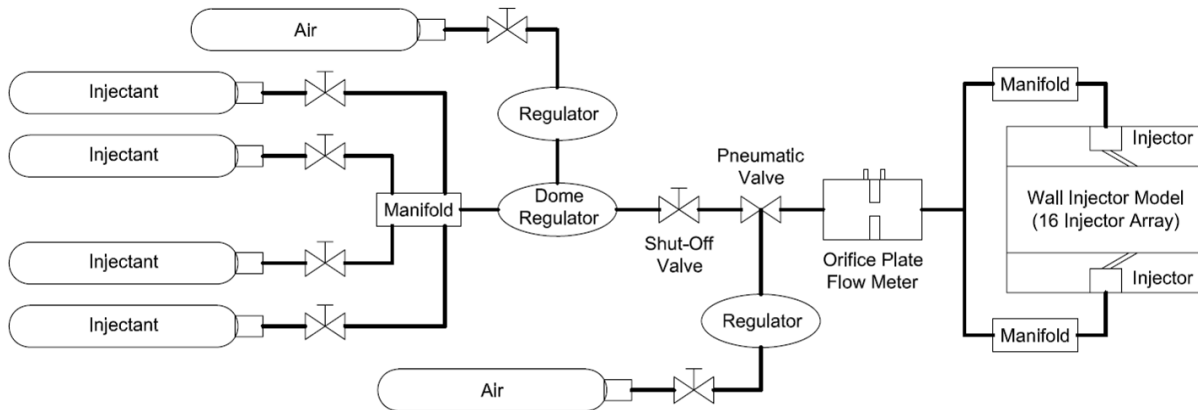


Figure 2.14: Injection system for the flush-wall injector model using orifice plate flow meter

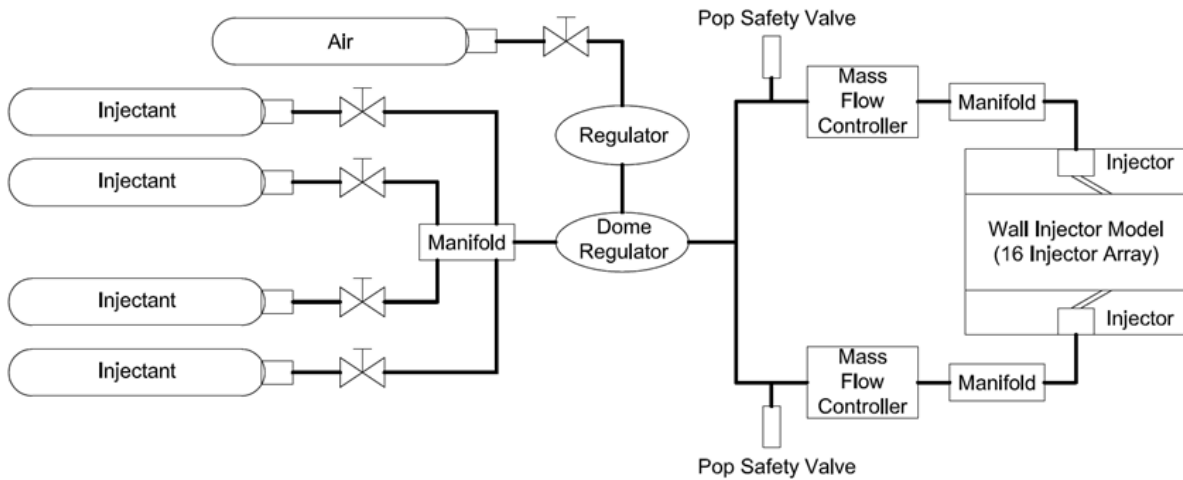


Figure 2.15: Injection system for the flush-wall injector model using mass flow controllers

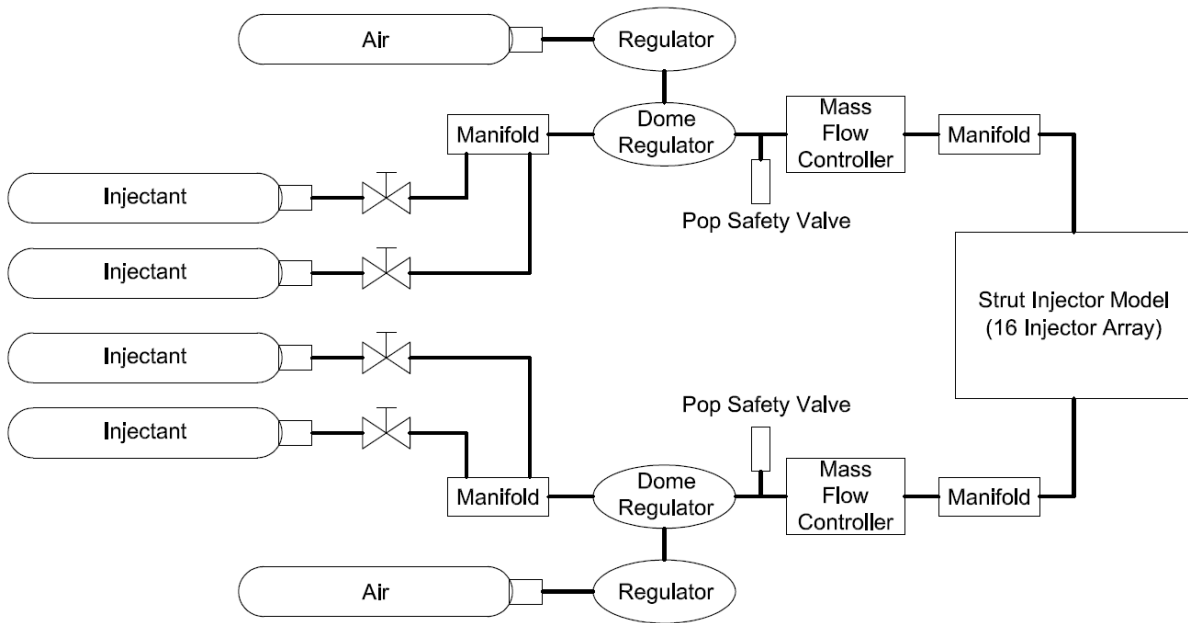


Figure 2.16: Injection system for the strut injector model

All of the configurations of the injection system have some common features. First, the injectant is supplied by a group of high pressure commercial gas bottles. The gas bottles are connected to a manifold and then to a dome-loaded regulator, which regulates the pressure that is being applied on the upstream side of the mass flow controllers (or orifice plate flow meter). The output of the dome-loaded regulator is set by using a second regulator to apply the desired output pressure to the diaphragm of the dome regulator. After the gas passes through the dome regulator and through the mass flow controllers (or orifice plate flow meter), two identical

manifolds are used to evenly distribute the gas to each of the 16 injectors in the arrays. In the orifice plate flow meter system configuration, an electronically controlled pneumatic valve is used to turn the flow on and off. In the configurations with the mass flow controllers, pop safety valves are used to protect the mass flow controllers from being accidentally over-pressured.

2.3 Instrumentation

2.3.1 Mass Flow Controllers

A system of two Teledyne-Hastings model HFC-D-307 digital mass flow controllers was used to control the injectant mass flow rate for the majority of the experiments (7 out of 9 experimental cases). These mass flow controllers were selected primarily due to their high flow capacity, high accuracy, and fast response time. Figure 2.17 shows a picture of one of the mass flow controllers and also the power supply and control module that is used with the system. Each mass flow controller uses a PID (Proportional – Integral – Derivative) control valve and is capable of controlling multiple types of gases. Each individual flow controller was calibrated by the manufacturer using air as the calibration gas. When the flow controllers are used to determine the mass flow rates of gases other than air, correction factors must be used. For helium and methane gases, the gas correction factors were empirically determined and provided by the manufacturer. The power supply unit shown in Figure 2.17 is capable of powering and controlling up to four mass flow controllers. The entire system is controlled by a LabVIEW program via digital communication over one of the serial ports of the lab computer. Alternatively, the system can be controlled manually by entering commands into the power supply unit. Each flow controller produces a 0-5 VDC analog output signal that is linearly proportional to the measured mass flow rate. These signals are recorded by the data acquisition system (see Section 2.1.1.1) and saved for further analysis.



Figure 2.17: Picture of one of the mass flow controllers (left) and its power supply and control module (right)

The response time of the flow controllers is about 2 seconds, which is the time it takes to go from zero flow to within +/- 2% of the mass flow set point. The accuracy rating of the mass flow controllers depends upon flow rate and also upon the type of gas that is being controlled (the type of gas influences the full-scale output of the flow controllers). For the mass flow rates used with the flow controllers in these experiments, the accuracy of the system of two flow controllers for each type of gas is as follows:

- Helium: 22.5 g/s +/- 0.5 g/s (2.2% of reading)
- Methane: 47.29 g/s +/- 1.12 g/s (2.4% of reading)
- Air: 62.66 g/s +/- 0.58 g/s (0.9% of reading)

For additional information on the accuracy of the flow controllers, refer to Appendix C. For information on how the injectant mass flow rates for the experiments were selected, refer to sections 3.1 and 4.1.

2.3.2 Orifice Plate Flow Meter

Prior to the acquisition of the mass flow controllers, an orifice plate flow meter was used to measure the injectant mass flow rate. The mass flow rate through the flow meter (\dot{m}_o) was determined by measuring the pressure upstream of the orifice (p_1), the temperature upstream of the orifice (T_1), and the differential pressure across the orifice (Δp) and applying the following equation (from ASME MFC-3M-2004⁴¹):

$$\dot{m}_o = \frac{C_{d,o}}{\sqrt{1-\beta^4}} \varepsilon \frac{\pi}{4} d_o^2 \sqrt{2\Delta p \rho_1} \quad (2.1)$$

In this equation, $C_{d,o}$ is the discharge coefficient given by equation 2.2, d_o is the diameter of the orifice, ρ_1 is the gas density upstream of the orifice given by equation 2.4, ε is an expansibility factor given by equation 2.9, and β is the diameter ratio ($\beta = d_o / d_p$) where d_p is the upstream internal pipe diameter. For pipe flow with a Reynolds number (based upon the pipe diameter, d_p) above 4000, an orifice plate flow meter with corner taps has the following discharge coefficient (from Miller⁴²):

$$C_{d,o} = 0.5959 + 0.0312\beta^{2.1} - 0.184\beta^8 + \frac{91.71\beta^{2.5}}{\text{Re}_{d_p}^{0.75}} \quad (2.2)$$

The discharge coefficient can also be determined from tables that are available in ASME MFC-3M-2004⁴¹. To solve for the discharge coefficient, the Reynolds number must be determined. The Reynolds number upstream of the orifice based on the pipe diameter is defined as:

$$\text{Re}_{d_p} = \frac{\rho_1 u_1 d_p}{\mu} \quad (2.3)$$

The gas density (ρ_1) can be determined using the perfect gas relation:

$$\rho_1 = \frac{p_1}{RT_1} \quad (2.4)$$

The flow through the orifice plate is choked resulting in sonic conditions through the orifice. Thus, the velocity upstream of the orifice (u_1) can be found using definition of Mach number (equation 2.5) and the area-Mach number relation (equation 2.6):

$$u_1 = M_1 a_1 = M_1 \sqrt{\gamma RT_1} \quad (2.5)$$

$$\frac{A_1}{A^*} = \frac{1}{M_1} \left[\frac{2}{\gamma + 1} \left(1 + \frac{\gamma - 1}{2} M_1^2 \right) \right]^{\frac{\gamma + 1}{2(\gamma - 1)}} \quad (2.6)$$

where

$$A_1 = \frac{\pi d_p^2}{4} \quad (2.7)$$

$$A^* = \frac{\pi d_o^2}{4} \quad (2.8)$$

The expansibility factor is found by using the following empirical relation (from ASME MFC-3M-2004⁴¹):

$$\varepsilon = 1 - (0.351 + 0.256\beta^4 + 0.93\beta^8) \left[1 - \left(\frac{p_2}{p_1} \right)^{\frac{1}{\gamma}} \right] \quad (2.9)$$

where p_2 is the pressure downstream of the orifice given by:

$$p_2 = p_1 - \Delta p \quad (2.10)$$

The orifice plate flow meter was used for experiments with helium injection at two different mass flow rates, 22.5 g/s and 30 g/s. The uncertainty in the helium mass flow rate measured by the orifice plate flow meter for the two different experiments was estimated as:

- Helium (22.5 g/s operation): 22.5 g/s +/- 0.11 g/s (0.5% of reading)
- Helium (30 g/s operation): 30 g/s +/- 0.12 g/s (0.4% of reading)

An uncertainty analysis for the orifice plate flow meter is presented in Appendix C.

2.3.3 Probe Traversing System

The two-axis traverse system shown in Figure 2.18 was used to position measurement probes within the test cabin. The traverse system operates at a velocity of about 10 mm/s and is controlled via digital communication through one of the serial ports on the lab computer with a LabVIEW program. The probes were inserted into the test cabin through a slot in the cabin lid, which was sealed using the combination of a sliding plate and a rubber gasket. This arrangement allows the traverse system to move a probe freely in both the spanwise and vertical directions while effectively sealing the test cabin. Measurements were taken approximately 2 mm in the streamwise direction beyond the end of the duct where the flow enters the test cabin. At this measurement plane, grids of data points were measured across a section of the duct. The grid spacing was typically 1-2 mm in both the spanwise and vertical directions.

The alignment of probes within the test cabin presented a significant challenge for many reasons such as: (1) access to the test cabin is only available through the cabin lid and (2) to prevent damage to the probes, touching a probe to a surface was not an option. Alignment was accomplished by aligning the probes to an injector, which was positioned in a known location above the duct centerline. During the alignment procedure, a constant pressure was applied to the alignment injector using a regulator. The probe position was then adjusted until the maximum pressure produced by the alignment injector was found, which corresponds to the center of the injector. A small value was chosen for the diameter of the alignment injector, 0.76 mm (0.03 in), to facilitate accurate alignment. Based on the manufacturing tolerances and the accuracy of the alignment procedure, the estimated uncertainty of the measurement grid origin

location is ± 0.25 mm in both the spanwise and vertical directions. Based on the accuracy of the traverse system, the estimated uncertainty of the grid points relative to one another is ± 0.01 mm in both the spanwise and vertical directions.

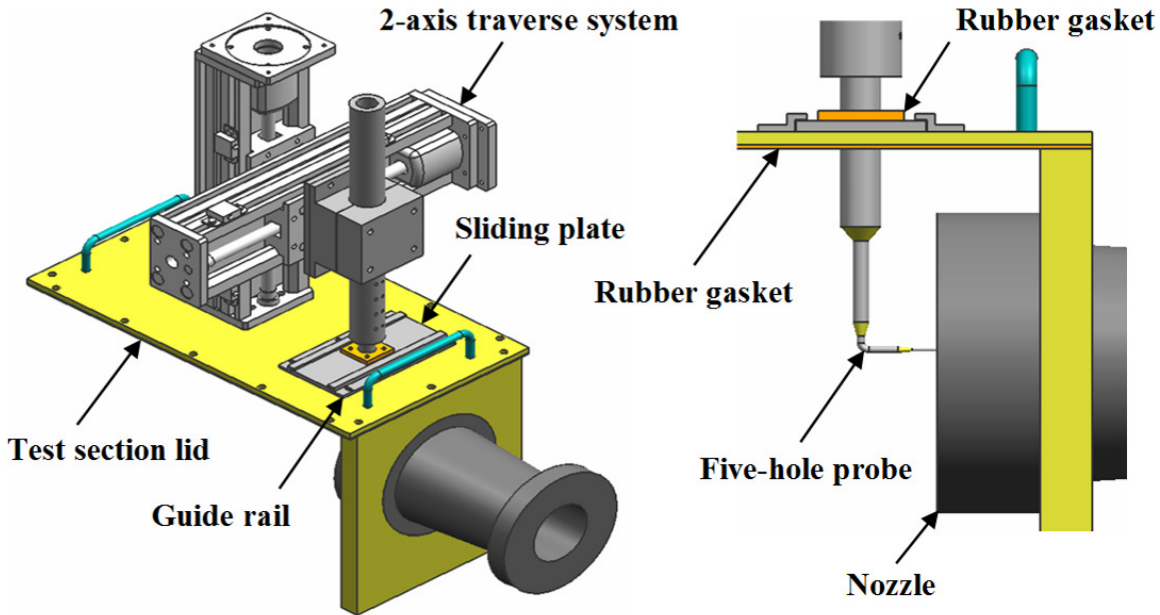


Figure 2.18: Picture of the probe traversing system mounted to the test cabin (test cabin side walls are removed)

2.3.4 Concentration Sampling Probe

Since this is primarily a mixing study, the acquisition of accurate gas composition measurements is crucial. Gas composition measurements were made using a specialized probe, which was designed based upon the fundamental concept developed at Virginia Tech by Ninnemann and Ng⁴³. The concentration is measured in terms of the mass fraction of a gas (e.g. helium or methane) in the overall gas mixture. The concentration sampling probe is an aspirating type probe that is attached to a vacuum pump. Figure 2.19 shows the influence of the vacuum pump on the shock system associated with the probe tip. The vacuum pump is used to suck in the detached normal shock that would normally occur in front of the probe tip in supersonic flow. This allows a streamtube equal to the probe capture area to enter the probe undisturbed and undistorted for isokinetic sampling. Without the vacuum pump, the flow would spill around the probe tip resulting in unrealistic concentration measurements. For instance, if the mixture that is being sampled is a light gas (e.g. helium or hydrogen) mixed with air, then the light gas will be

deflected by the spillage more than the heavier air. The result is a measured concentration of the light gas less than the true concentration. This problem is referred to as “selective sampling” and is further described in references 24 and 44.

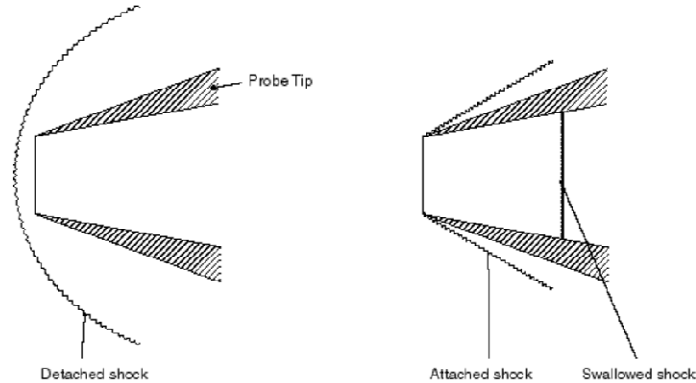


Figure 2.19: Comparison of the shock system near the probe tip for a non-aspirating probe (left) vs. an aspirating probe (right) [from Xillo et al.⁴⁵]

Figure 2.20 shows a diagram of the concentration probe. Inside the probe, there is a constant temperature hot-film sensor operating in a channel with a choked exit. The inlet hole at the tip of the probe has the same diameter as the choked orifice, 0.64 mm (0.025 in). The choices made for these dimensional values combined with the use of a vacuum pump prevents a detached normal shock from occurring in front of the probe tip. Schlieren flow visualization confirmed the absence of a detached normal shock. At the measurement plane, the probe has a pressure tap and a thermocouple, which are located nearby the hot-film sensor. The pressure tap is connected to an externally located pressure transducer using hypodermic tubing. The probe has a diverging tip (i.e. nozzle), which initially accelerates the flow until the point at which the normal shock occurs. After the normal shock, the flow is decelerated as the tip continues to diverge. Once the flow reaches the measurement plane, it has been decelerated to a Mach number of approximately 0.05.

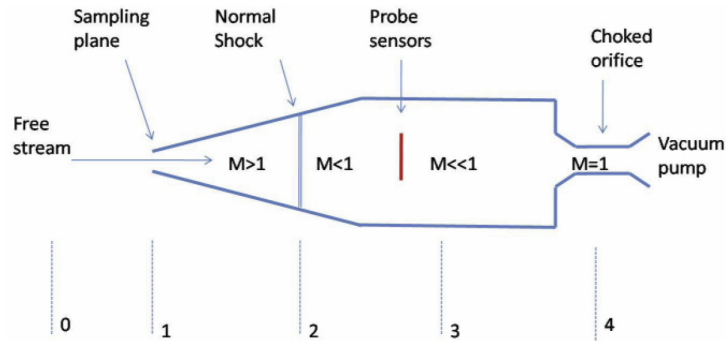


Figure 2.20: Diagram of the concentration probe (from Maddalena⁴⁶)

The concentration sampling probe is only capable of measuring the mean species concentration of a gas mixture, because it does not have high enough frequency response to measure fluctuating concentration values in supersonic turbulent flow. Additionally, due to the principle of operation of the probe, it is only capable of measuring binary gas mixtures. The overall frequency response of the concentration probe is approximately 20 Hz and is limited by the response of the external pressure transducer and associated tubing. The mean species concentration is found by averaging concentration measurements that are taken over a time interval. For these experiments, the concentration probe was paused at each experimental data point for a total of 200 ms due to the response time associated with the external pressure transducer and the need for a finite time interval over which to average the concentration measurements. Data was sampled at 500 Hz and 120 ms of data for each experimental data point was analyzed to determine the mean concentration at each point. Under typical conditions, the flow through time for the probe was calculated to be approximately 7 ms.

Two slightly different configurations of the same basic concentration probe design were used for the experiments. Figure 2.21 shows pictures of the two different concentration probe configurations. Both probes have the same nominal electrical properties and critical dimensions. Furthermore, the measurement uncertainty of the two probes was found to be nearly identical (refer to Appendix C). The primary differences between the two concentration probes are:

- One probe has a straight tip to avoid any negative flow angularity effects, whereas the other probe has an angled tip to facilitate measurement near a surface
- The straight tip concentration probe has an attached cone-static probe to allow for simultaneous concentration and cone-static measurements

For a more detailed discussion of the differences between the two probes, refer to Appendix B.

The housing of the each probe was designed to fit around the body of a TSI model 1210-20 hot-film sensor. The hot-film sensor is made of platinum and has a diameter of 50.8 μm with an active sensor length of 1.02 mm. The hot-film sensor is used in conjunction with a Dantec model 56C17 constant temperature anemometer (CTA) fitted with a Dantec model 56C01 CTA bridge. The overheat ratio of the hot-film sensor is defined as:

$$\frac{R_f - R_0}{R_0} \quad (2.11)$$

Here, R_f is the heated sensor resistance at operating temperature and R_0 is the cold sensor resistance at ambient temperature. For all of the experiments, an overheat ratio of 1.0 was used for the hot-film sensor of the concentration probe.

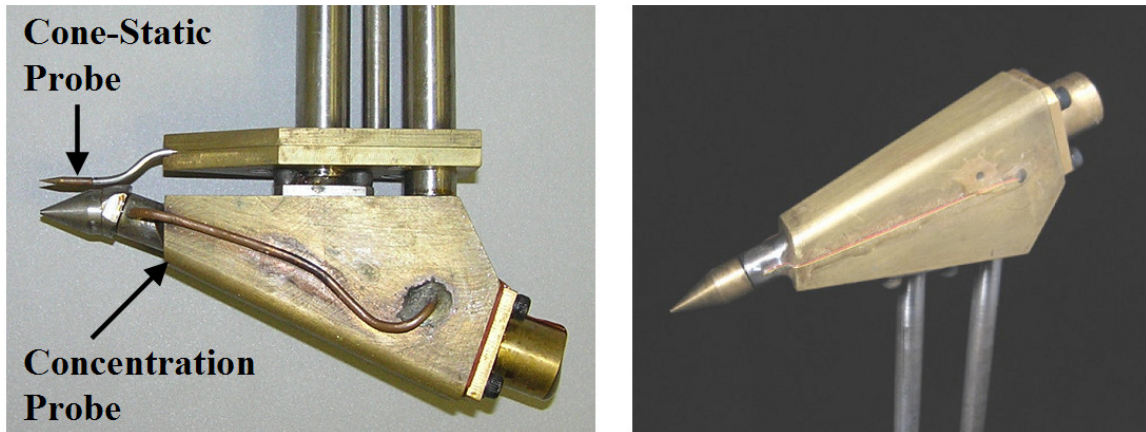


Figure 2.21: Picture of the concentration probe with the straight tip and integrated cone-static probe (left) vs. the concentration probe with the angled tip (right)

2.3.4.1 Principle of Operation

Referring to Figure 2.20, the continuity of mass flow through the concentration probe can be written as:

$$(\rho u A)_1 = (\rho u A)_2 = (\rho u A)_3 = (\rho u A)_4 \quad (2.12)$$

The mass flow rate at each station can also be written as:

$$\rho u A = p_0 M A \sqrt{\frac{\gamma}{RT_0} \left(1 + \frac{\gamma - 1}{2} M^2 \right)^{-\frac{\gamma + 1}{2(\gamma - 1)}}} \quad (2.13)$$

The flow throughout probe is assumed to be adiabatic (T_0 is a constant). In addition, the gas composition is assumed to be the same throughout the probe (γ and R are constants). Thus, in the case of the choked orifice at station 4 ($M_4 = 1$ and $A_4 = A^*$), equation 2.13 reduces to:

$$(\rho u A)_4 = p_{04} A_4 \sqrt{\frac{\gamma}{RT_{04}}} \left(\frac{\gamma + 1}{2} \right)^{-\frac{\gamma+1}{2(\gamma-1)}} = p_{04} A^* \sqrt{\frac{\gamma}{RT_{04}}} \left(\frac{\gamma + 1}{2} \right)^{-\frac{\gamma+1}{2(\gamma-1)}} \quad (2.14)$$

Equating the mass flow rate at the measurement plane (station 3) to the mass flow rate at the choked orifice (station 4) and assuming that there is no total pressure loss between stations 3 and 4 ($p_{03} = p_{04}$), it is possible to express the mass flux at the measurement plane as:

$$(\rho u)_3 = p_{03} \frac{A^*}{A_3} \sqrt{\frac{\gamma}{RT_{03}}} \left(\frac{\gamma + 1}{2} \right)^{-\frac{\gamma+1}{2(\gamma-1)}} \quad (2.15)$$

Therefore, the mass flux at the measurement plane is a function of the total pressure and total temperature at the measurement plane, the geometry of the probe, and the gas composition through the gas constant, R , and the ratio of specific heats, γ . Furthermore, since the Mach number at the measurement plane is approximately 0.05, the pressure and temperature measured at this plane approximately represent the total pressure and temperature of the fluid ($p_3 \approx p_{03}$ and $T_3 \approx T_{03}$).

The rate of heat transfer from the hot-film is given by:

$$q_f = I_f^2 R_f \quad (2.16)$$

where I_f is the hot-film current and R_f is the hot-film heated resistance. For a constant temperature anemometer, the relation between the hot-film voltage and the hot-film current is:

$$I_f = \frac{V}{R_f + R_{lc} + R_s} \quad (2.17)$$

where R_s is the bridge resistance in series with the hot-film and R_{lc} is the combination of the probe lead and probe cable resistances. In order to relate the hot-film heat transfer rate to the difference between the hot-film and fluid temperatures, the Nusselt number is used:

$$Nu = \frac{q_f}{\pi k l (T_f - T_{03})} \quad (2.18)$$

where k is the thermal conductivity of the gas mixture, l is the active sensing length of the hot-film, and T_f is the hot-film temperature. Using equations 2.16 and 2.17, the Nusselt number can be rewritten as:

$$Nu = \frac{R_f}{(R_f + R_{lc} + R_s)^2} \frac{V^2}{\pi k l (T_f - T_{03})} \quad (2.19)$$

The Nusselt number can then be expressed as a function of the Reynolds number. For air, this can be accomplished using King's law ($Nu = a + b\sqrt{Re}$). However, for helium-air mixtures, it was found that the following relation is more appropriate⁴⁷:

$$Nu = a(Re_d)^b = a \left(\frac{\rho u d_f}{\mu} \right)^b \quad (2.20)$$

In this equation, a and b are empirically determined constants that are only dependent upon the gas composition, and d_f is the diameter of the hot-film. Equation 2.20 was also validated for methane-air mixtures according to the procedure described in Appendix C, Section C.3.1. Using equations 2.15, 2.19, and 2.20, the governing equation for the hot-film anemometer voltage can be written as:

$$V^2 = \frac{(R_f + R_{lc} + R_s)^2}{R_f} \pi k l a \left[\frac{d_f}{\mu} p_{03} \frac{A^*}{A_3} \sqrt{\frac{\gamma}{RT_{03}}} \left(\frac{\gamma + 1}{2} \right)^{-\frac{\gamma+1}{2(\gamma-1)}} \right]^b (T_f - T_{03}) \quad (2.21)$$

The parameters k , μ , γ , and R as well as the constants a and b are properties of the gas mixture. Furthermore, since a constant temperature anemometer is used, T_f and R_f are constant (and depend on the overheat ratio chosen for the hot-film). Additionally, the values R_{lc} , R_s , l , and d are system parameters and remain constant. Therefore, the voltage response of the hot-film anemometer is only a function of the total pressure, p_{03} , the total temperature, T_{03} , and the gas composition. Thus, it is possible to write equation 2.21 in functional form as:

$$V = f(p_{03}, T_{03}, \alpha) \quad (2.22)$$

In this equation, the gas composition is represented by α , the mass fraction of a gas in a binary gas mixture.

2.3.4.2 Calibration

A calibration procedure for the concentration probe is necessary to determine the empirical constants, a and b , which are used in equation 2.20. The concentration probe was calibrated to

measure the mole fraction of a gas (e.g. helium or methane) in a binary gas mixture (e.g. helium-air or methane-air), which is uniquely related to a given pressure, temperature, and rate of heat transfer sensed at the hot-film. A hot-film responds to local mass flux variations. Once the mole fraction of a gas in a binary mixture is known, then the corresponding mass fraction can also be calculated.

Calibration of the probe is accomplished by connecting the probe to a tank that is filled with a known mixture of gases. A picture of the tank that is used for the calibration procedure is shown in Figure 2.22. A pressure transducer measures the pressure of the calibration tank. The tank is sealed and connected to two commercial gas bottles, one for each type of gas in the binary mixture. The calibration tank is then carefully filled with partial pressures of each gas. A small battery-powered fan is used ensure that the gas within the calibration tank remains mixed during the calibration procedure. The ratio of the partial pressure of one gas to the overall pressure in the tank is the mole fraction of that gas in the mixture. For example, if the tank is filled to 2.4 atm with air and then helium is added to the tank until the tank pressure is 3 atm, then the helium mole fraction in the tank is $0.6 / 3 = 20\%$. Once the tank is filled with a known mixture of gases, flow is released to the concentration probe via tubing and the concentration probe gradually sucks down the pressure in the tank as calibration data points are being taken. Pressure, temperature, and hot-film voltage are measured at each calibration data point. This procedure is repeated for mole fractions of a gas ranging from 0% - 100% in 10% increments, which generates the calibration curves shown in Figures 2.22 – 2.24. In between each 10% increment, a vacuum is used to clear the residual gas from the calibration tank.

Figure 2.23 shows the calibration results for a helium-air mixture, and Figure 2.24 shows the calibration results for a methane-air mixture with both calibrations performed at an overheat ratio of 1.0. An examination of Figures 2.22 and 2.23 reveals that the concentration probe operates over a much wider range of voltage for a helium-air mixture than for a methane-air mixture. The probe operates by utilizing variations in the gas constant (i.e. mixture molecular weight), which ultimately means that the probe has reduced sensitivity and increased uncertainty for a methane-air mixture in comparison to a helium-air mixture. Figure 2.25 shows the calibration results for a helium-air mixture at an overheat ratio of 0.5. A comparison of Figures 2.22 and 2.24 shows that

the probe operates over a wider range of voltage at the higher overheat ratio. Thus, the probe should always be operated at a high overheat ratio to improve sensitivity and reduce uncertainty. For these experiments, the overheat ratio for the hot-film sensor was chosen so that the hot-film would operate slightly below than the maximum heated sensor operating temperature specified by the manufacturer (425°C). Therefore, an overheat ratio of 1.0 (corresponding to a heated sensor temperature of 400°C) was used for all of the experiments.



Figure 2.22: Picture of the calibration tank for the concentration probe

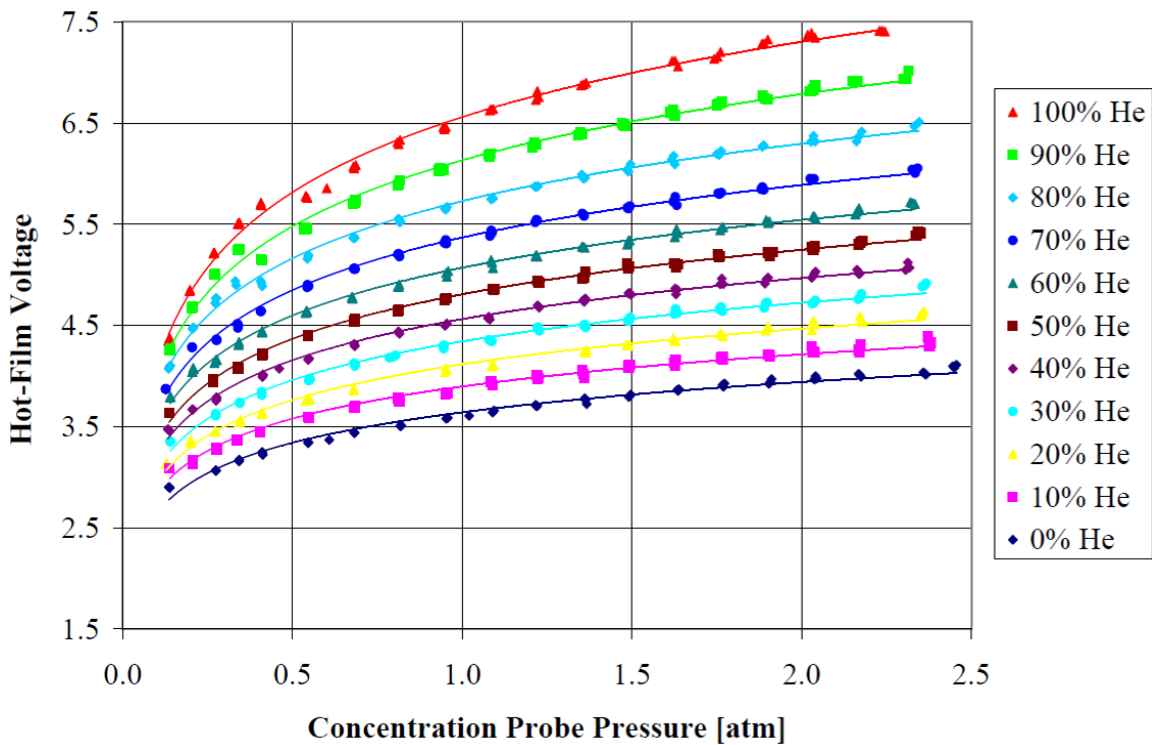


Figure 2.23: Concentration probe calibration results for a helium-air mixture for an overheat ratio of 1.0

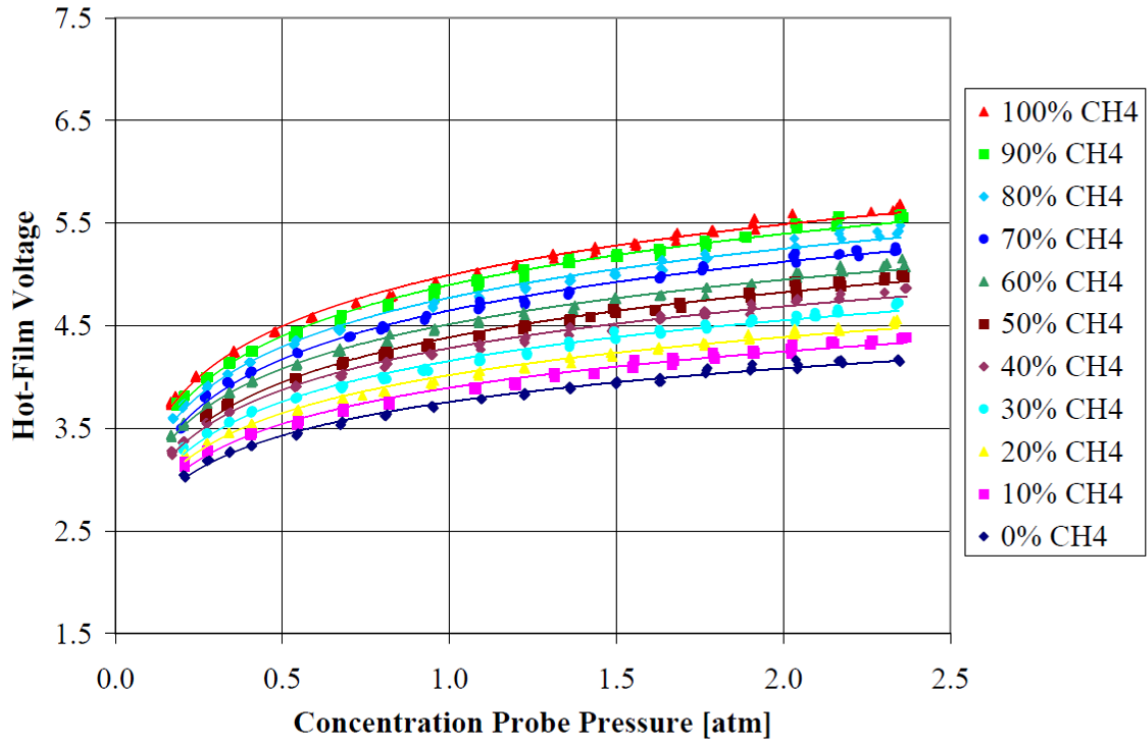


Figure 2.24: Concentration probe calibration results for a methane-air mixture for an overheat ratio of 1.0

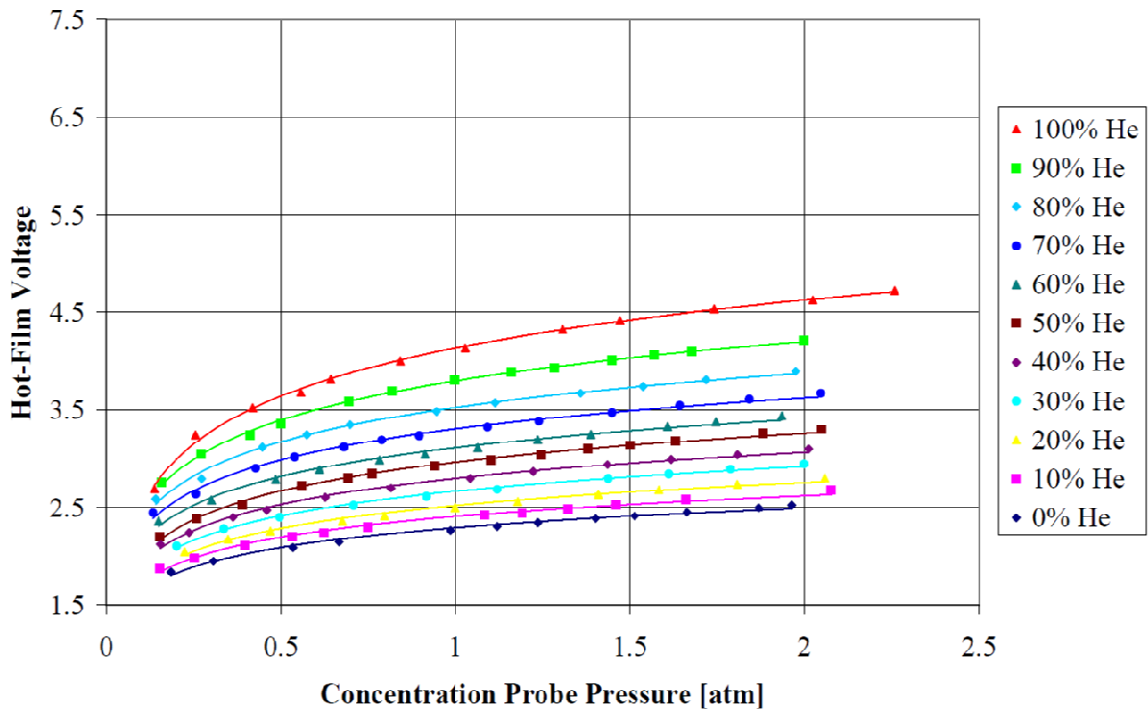


Figure 2.25: Concentration probe calibration results for a helium-air mixture for an overheat ratio of 0.5

2.3.4.3 Data Analysis

Data analysis for the concentration probe was accomplished using a Matlab code that utilized the governing equations (refer to Section 2.3.4.1) and the calibration data. At each concentration data point, values of pressure, temperature, and hot-film voltage were measured. The code then used the pressure and temperature data for each point and equation 2.21 to calculate upper and lower voltage bounds between the two nearest calibration curves. The code would start with the calibration curve for the lowest gas (i.e. helium or methane) concentration and sequentially search for the two curves that bounded the voltage at the corresponding pressure. The code then calculated the concentration value at each point using interpolation from the bounding curves.

2.3.4.4 Measurement Uncertainty

Figure 2.26 shows a plot of the estimated measurement uncertainty for the concentration probe, which is applicable to both versions of the probe (straight tip and angled tip). An uncertainty analysis for the concentration probe is presented in Appendix C. The differences between the two probes were found to have a very small effect on the measurement uncertainty results. In this figure, the measurement uncertainty of the concentration probe is presented as a function of the mass fraction reading for both helium and methane gas mixtures in air.

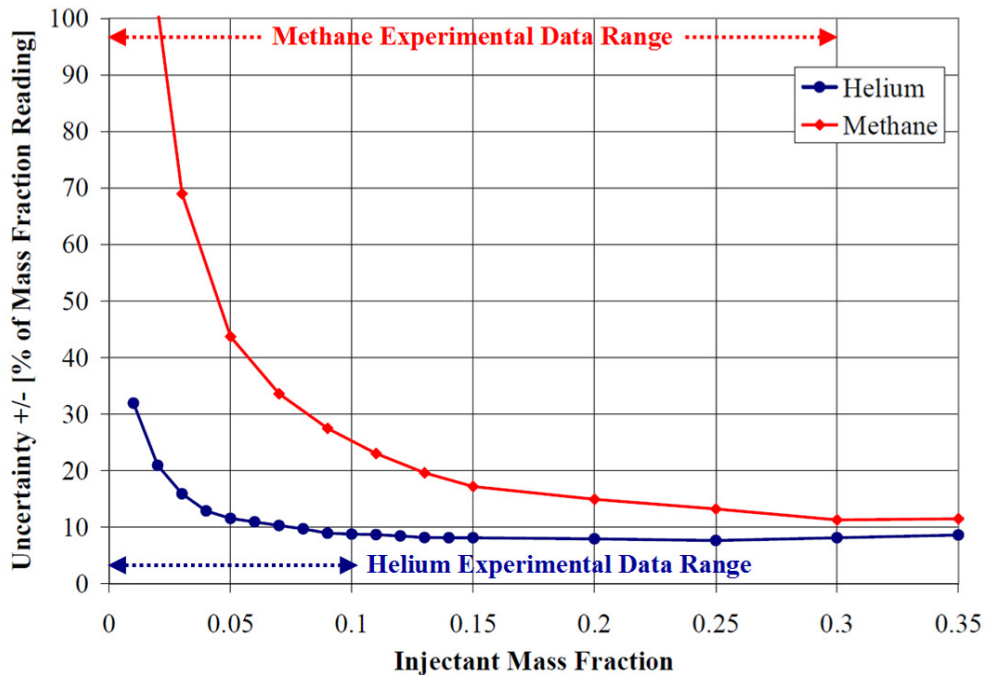


Figure 2.26: Concentration probe measurement uncertainty

From Figure 2.26, it is evident that the measurement uncertainty for a helium-air mixture is less than that of a methane-air mixture. Furthermore, the measurement uncertainty of the probe decreases as mass fraction increases. An important observation from these uncertainty results is that the measurement plane for gas composition sampling (located a certain distance downstream of the injection position) must be carefully selected, so that the uncertainties associated with the concentration probe are minimized.

2.3.4.5 Correction for Test Facility Effects on Concentration Measurements

Variations in the total pressure and total temperature of the hypersonic tunnel during a run and from run to run have an influence on the overall mixture ratio (i.e. fuel-air ratio) for the experiment. The injectant mass flow rate also varies, which also influences the overall fuel-air ratio. The variations of these properties during a hypersonic tunnel run are significant. However, the runs are highly repeatable, so the run to run variations of these properties are a much less significant factor. For instance, the total pressure of the hypersonic tunnel typically varies +/- 5% from the average value during a run, but the average total pressure during a run is repeatable within about +/- 1% from run to run. Typical variations of the injectant mass flow rate and total temperature during a run are both about +/- 2% from their average values. The hypersonic tunnel does not have a total temperature sensor in the plenum chamber. To determine the typical variation of the total temperature in the plenum chamber during a run, a total temperature probe (refer to Section 2.3.6) was placed in the freestream flow at the exit of the nozzle. The total temperature of the freestream was then measured during multiple runs to determine the typical variation of this property. Then, an empirically determined recovery factor for the total temperature probe was used (refer to Section 2.3.6) to calculate the total temperature in the plenum chamber. Figure 2.27 shows a plot of the fuel-air ratio variation during typical hypersonic tunnel runs for different injectants and freestream Mach number conditions covering all of the different experimental cases. The amount of fuel-air ratio variation during a typical run was approximately +/- 5% from the average value during the run. This plot was generated by accounting for the variations in total pressure, total temperature, and injectant mass flow rate during a run. In Figure 2.27, only the portion of time when the tunnel is operating supersonically is shown (typically about 2.2-2.3 seconds out of a 3.2 second run).

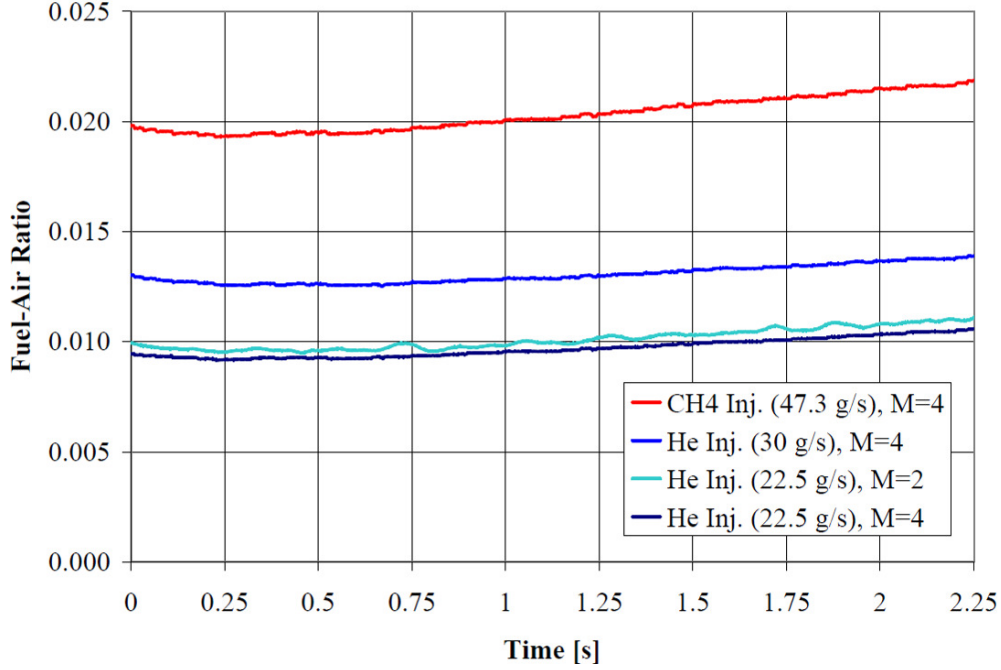


Figure 2.27: Fuel-air ratio variation during typical hypersonic tunnel runs for different injectants and freestream Mach numbers

To account for the influence of the fuel-air ratio variation on the experimental mixing results, a correction factor was used. The factor corrects a concentration measurement to correspond to a nominal (fixed) fuel-air ratio, f_{nom} , based on the actual concentration measured at a slightly varying fuel-air ratio, f_i . Using this method, all of the concentration data for each experimental case can be normalized to correspond to the nominal fuel-air ratio for that case. This is important for comparison to CFD results that are run at a fixed fuel-air ratio. The first-order concentration correction factor (c) is defined as:

$$c = \frac{f_{nom}}{f_i} \quad (2.23)$$

where f_{nom} is the nominal fuel-air ratio and f_i is the instantaneous fuel-air ratio measured at each concentration data point. The correction factor is then applied to each concentration data point by the following relation:

$$\alpha_{i,nom} = c\alpha_i = \frac{\alpha_i}{f_i} \times f_{nom} \quad (2.24)$$

where α_i is the instantaneous measured concentration and $\alpha_{i,nom}$ is the corrected concentration based on the nominal mixture ratio. The correction factor has a relatively small influence on the

concentration data (the $\alpha_{i,nom}$ values are typically within +/- 5% of the α_i values). Additionally, sometimes the concentration data is required to solve for values of Mach number and total pressure (refer to section 2.4.2). In this case, the concentration correction factor has a very small influence on the Mach number data (on the order of 0.25%) and a small influence on the total pressure data (on the order of 1%).

2.3.5 Cone-Static Probe

A cone-static probe was used to allow for the determination of Mach number and total pressure for a given flowfield using a multiple probe survey method. A cone-static probe was attached to the straight tip concentration probe (see Figure 2.21) to allow simultaneous concentration and cone-static measurements to be made. This cone-static probe was positioned in a location that is always outside of the oblique shock generated by the tip of the concentration probe. When the angled tip concentration probe was used, a separate survey using the cone-static probe from the triple-rake probe (see Figure 2.28) was performed. Both cone-static probes are nominally the same and consist of a 1.59 mm (1/16 in) outer diameter tube capped with a 10° half-angle cone. Four small pressure ports are located at 90° spacing around the surface of each cone.

2.3.6 Aero-Thermodynamic Triple-Rake Probe

Figure 2.28 shows a picture of the aero-thermodynamic triple-rake probe, which consists of three separate probes: a Pitot probe, a total temperature probe, and a cone-static probe. Each individual probe was built using 1.59 mm (1/16 in) outer diameter tubing. From center to center, each probe is spaced 6.35 mm (1/4 in) apart from the others. The recovery factor of the total temperature probe is defined as:

$$r = \frac{T_{02} - T_{\infty}}{T_{0\infty} - T_{\infty}} \quad (2.25)$$

where T_{02} is the total temperature measured by the probe, T_{∞} is the freestream static temperature, and $T_{0\infty}$ is the freestream total temperature. By placing the probe in the freestream of the supersonic tunnel and simultaneously measuring the plenum total temperature (considered to be the true freestream total temperature), the recovery factor of the total temperature probe was determined to be 0.98.



Figure 2.28: Picture of the triple-rake probe with Pitot probe (top), total temperature probe (middle), and cone-static probe (bottom)

2.3.7 Conical Five-Hole Pressure Probe

A miniature, fast-response, conical, five-hole pressure probe built by Aeroprobe, Inc. was used to measure local values of Mach number, total pressure, and flow angularity. These values can be determined based upon the port pressures of the probe using a calibration and data analysis procedure. A picture and diagram of the five-hole probe are shown in Figure 2.29. The probe uses five miniature piezoresistive pressure transducers, which are built into the probe housing near the tip. The tip of the probe is a 45° half-angle cone with an outer diameter of 1.65 mm. Each pressure port has a diameter of 0.25 mm. The amount of time required for the probe to achieve a 99% response to a step input is approximately 11 ms.

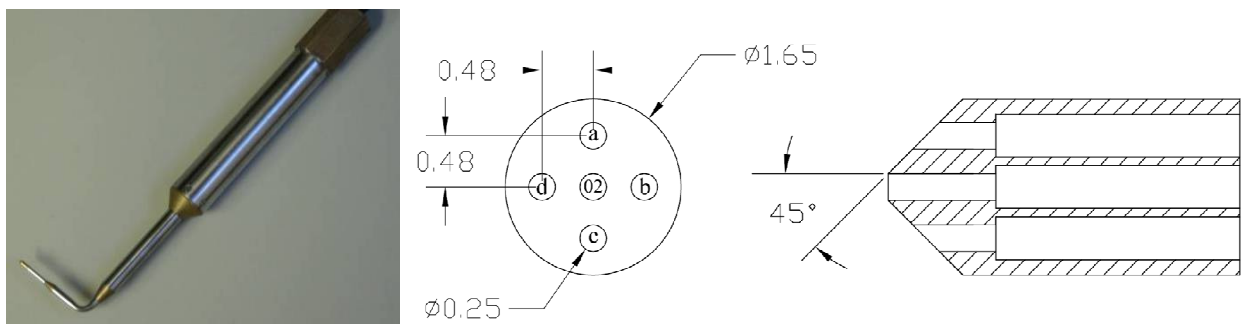


Figure 2.29: Picture of the five-hole probe (left) and drawing of the probe tip (right)

2.3.7.1 Calibration

Two separate calibrations were performed to allow for the determination of flow angularity and Mach number. First, the five-hole probe was calibrated to determine the flow angularity of an airstream as a function of its port pressures. The probe is sensitive to flow angularity based upon

the differences between the readings of its opposing peripheral ports (i.e. $p_c - p_a$ or $p_d - p_b$). The angular calibration was performed in the supersonic free-jet facility at Mach 3.1. The facility was run continuously while a traverse system programmed to perform an automated sequence of movements adjusted the pitch and roll of the probe while calibration data points were being taken. The angular calibration of the five-hole probe includes a total of 795 data points and covers an angularity range of $+18^\circ$ to -18° of pitch and $0-360^\circ$ of roll. The angular calibration data is shown in Figure 2.30 (note that this figure includes measurements for multiple pitch angles at a given roll angle). Once the angular calibration data was obtained, the data was then organized into non-dimensional pitch and roll coefficients using the method of Centolanzi⁴⁸:

$$C_{p\eta} = \frac{p_c - p_a}{q_1} \quad (2.26)$$

$$C_{p\xi} = \frac{p_d - p_b}{q_1} \quad (2.27)$$

When calculating the pitch and roll coefficients for any given situation, q_1 is defined as the local dynamic pressure. During the calibration, the probe is located in the freestream, so the freestream dynamic pressure is used for this case ($q_1 = q_\infty$ for the calibration). Once the pitch and roll coefficients were calculated, the angular calibration map shown in Figure 2.31 was created. The angular calibration map allows for the calculation of a set of pitch and roll angles, which correspond to a set of non-dimensional pitch and roll coefficients.

The work of Swalley⁴⁹ indicates that the angular calibration is valid over a wide range of Mach numbers and it is also valid for use in both air and gas mixtures. Using a 40° half-angle cone in experiments run at a Mach number of 3.55 in air and 21 in helium, Swalley confirmed the theory that only one calibration curve is required to determine flow angularity over a wide Mach number range in either air or helium for this type of instrument. In addition, angular calibrations were also performed for this type of instrument for various Mach numbers ranging from 1.72-4.32 by Centolanzi⁴⁸, Andrews et al.⁵⁰, and Naughton et al.⁵¹, which all indicate that the effects of Mach number on the calibration map are either negligible or small.

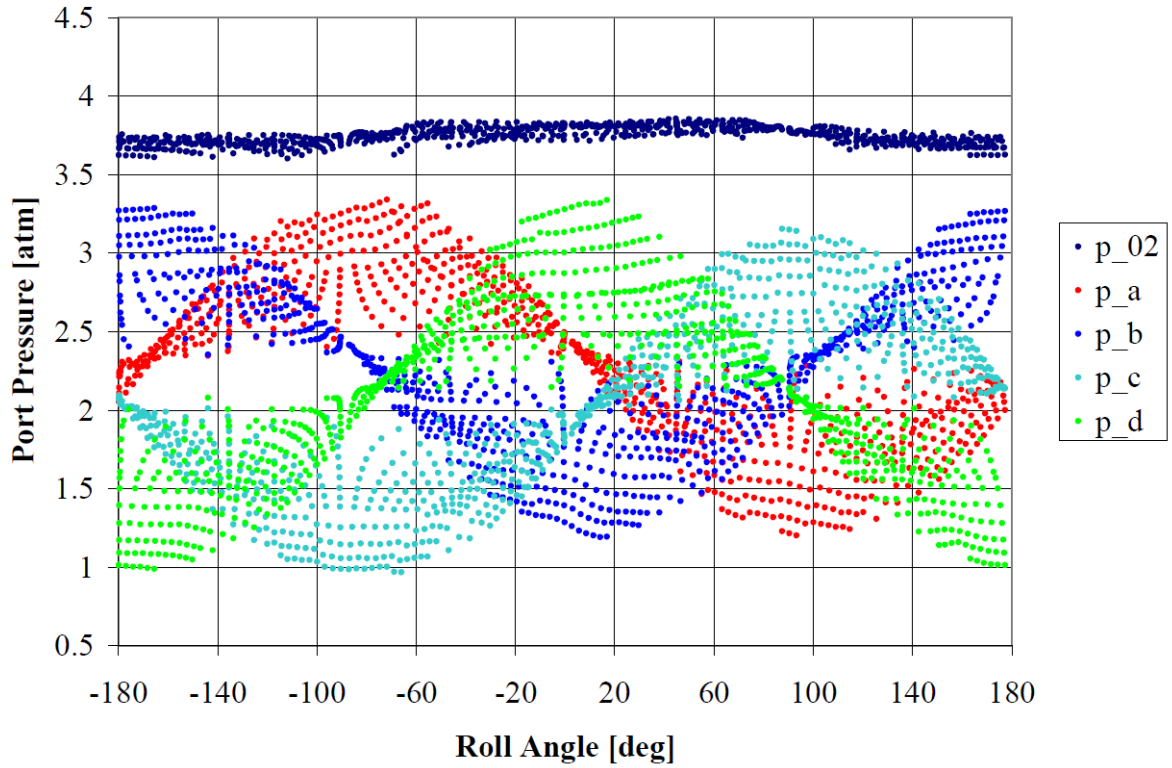


Figure 2.30: Five-hole probe angular calibration data

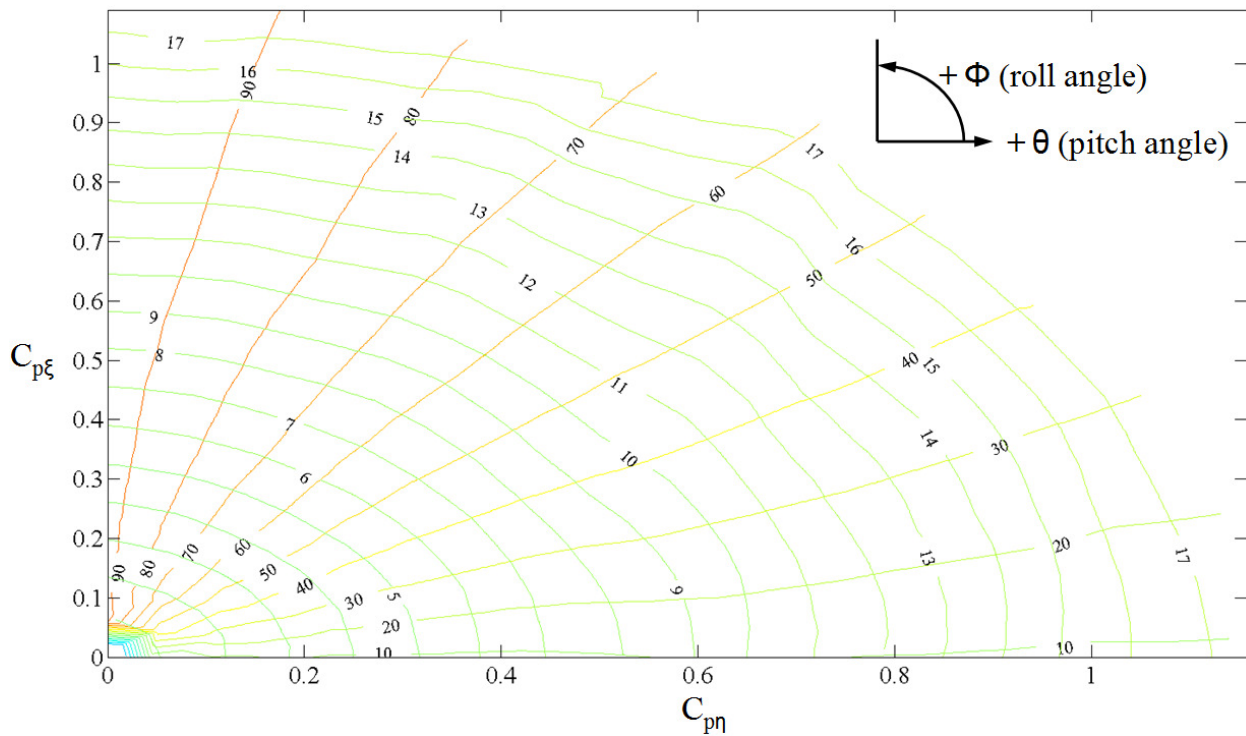


Figure 2.31: Five-hole probe angular calibration map

The five-hole probe was also calibrated to determine the Mach number of an airstream as a function of its port pressures. The probe is sensitive to Mach number based upon the ratio of the average of its peripheral port pressures (p_{avg}) to its center port pressure (p_{02}). The calibration of the five-hole probe to determine Mach number is necessary due to the geometry of the probe. The probe has a blunt tip where the center (Pitot) port is located, which is surrounded by four peripheral ports. Downstream of the blunt tip, flow expansion occurs resulting in a region of lower pressure behind the tip in comparison to a sharp cone with the same half-angle. Beyond the region affected by flow expansion, the pressure distribution will quickly recover to that of a sharp cone. However, the peripheral ports for the probe used in the current study are located in the region affected by flow expansion. Sharp cone theory cannot be used to predict the readings for these ports, therefore it is necessary to calibrate the probe to determine Mach number.

The Mach number calibration was performed by exposing the triple-rake probe and the five-hole probe to the same conditions in the supersonic wind tunnel. The Mach number measured by the triple-rake probe was then associated with the corresponding p_{avg} / p_{02} ratio measured by the five-hole probe. Variable Mach number conditions were obtained by passing the probes through the boundary layer of the supersonic tunnel wall. First, a survey with the triple-rake probe was performed to determine the Mach number at discrete points in the boundary layer. Next, a survey with the five-hole probe was performed to determine corresponding p_{avg} / p_{02} values for these points. This procedure was repeated using both the Mach 2.4 and Mach 4 nozzles of the tunnel to obtain a wide calibration data range. The resulting calibration data is shown in Figure 2.32. The calibration spans a range of Mach numbers from 1.6 – 3.9 and includes a total of 28 data points. Outside of the calibrated Mach number range, extrapolation down to Mach 1.32 and up to Mach 3.95 was used to estimate the Mach number from power curves fit to each end of the calibration data.

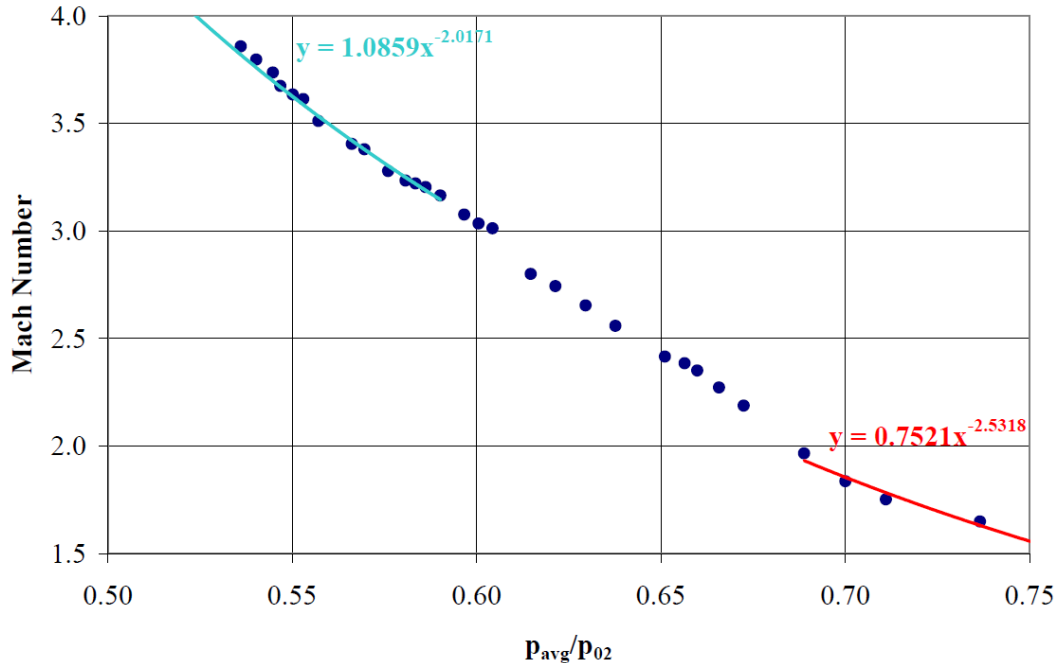


Figure 2.32: Five-hole probe Mach number calibration

There are several disadvantages associated with the method used to calibrate the five-hole probe to determine Mach number. First, any misalignment between the triple-rake probe and the five-hole probe induces error in the calibration results. Second, the pressures in the boundary layer are relatively low compared to that of the freestream flow, which makes these pressures more difficult for the five-hole probe to measure. The pressure transducers that are built into the five-hole probe have a differential range of +/- 3.40 atm (+/- 50 psi) with an accuracy rating of +/- 0.23% full-scale. These transducers work well for measuring pressures encountered in the freestream flow (typically in the range of 15-30 psia), but are somewhat less accurate for measuring pressures encountered in the boundary layer (typically in the range of 5-15 psia). Lastly, the amount of flow angularity that is present in the boundary layer is typically greater than that of the freestream flow. This is important because when the calibration data is used for data analysis (refer to Section 2.3.7.2), the analysis procedure assumes that no flow angularity is present in the Mach number calibration. Thus, any amount of flow angularity present in the Mach number calibration induces error in the final data analysis. Using the flow angularity calibration for the five-hole probe, it is possible to calculate the amount of flow angularity associated with each Mach number calibration data point and quantify this effect. The Mach number calibration data has an average flow angularity of 1.2° and a maximum flow angularity

of 3.3°. This amount of flow angularity in the Mach number calibration data has a very small effect on the final data analysis. This determination was made by accounting for and calculating the flow angularity effect as part of the uncertainty analysis for the five-hole probe (refer to Appendix C). It should also be noted that proving the amount of flow angularity in the boundary layer has a very small effect on the Mach number calibration also proves that the lateral gradients of velocity and other flow variables in the boundary layer have a very small effect on this calibration (and on the final data analysis). Nevertheless, there is potentially a better method that can be used to calibrate the five-hole probe to determine Mach number, which is to use a variable Mach number wind tunnel such as that used by Naughton⁵¹. This method reduces or eliminates the effects of the three issues discussed above. However, such a facility is not available at Virginia Tech, so the boundary layer survey method was employed instead.

2.3.7.2 Data Analysis

The data reduction process needed to convert the five-hole probe port pressures into incoming flow properties of Mach number, total pressure, and flow angularity follows that of Centolanzi⁴⁸. First, the average of the peripheral port pressures (p_{avg}) and the ratio p_{avg}/p_{02} is calculated. Next, the pitch angle (θ) is initially assumed to be zero and an initial estimate for the incoming Mach number (M_1) is obtained from Figure 2.32. The total pressure ratio across a normal shock is then found from the normal shock relation:

$$\frac{p_{02}}{p_{01}} = \frac{\left[\left(\frac{\gamma+1}{2} M_1^2 \right) / \left(1 + \frac{\gamma-1}{2} M_1^2 \right) \right]^{\frac{\gamma}{\gamma-1}}}{\left(\frac{2\gamma}{\gamma+1} M_1^2 - \frac{\gamma-1}{\gamma+1} \right)^{\frac{1}{\gamma-1}}} \quad (2.28)$$

The total pressure in front of the normal shock (i.e. in front of the probe) is then found by:

$$p_{01} = \frac{p_{02}}{p_{02}/p_{01}} \quad (2.29)$$

The ratio of the dynamic pressure to the total pressure in front of the normal shock is then found by:

$$\frac{q_1}{p_{01}} = \frac{\gamma p_1 M_1^2}{2 p_{01}} = \frac{\gamma M_1^2}{2 \left[1 + \frac{\gamma-1}{2} M_1^2 \right]^{\frac{\gamma}{\gamma-1}}} \quad (2.30)$$

The dynamic pressure in front of the normal shock is then found by:

$$q_1 = \left(\frac{q_1}{p_{01}} \right) p_{01} \quad (2.31)$$

The non-dimensional pitch and roll coefficients are then found from equations 2.26 and 2.27. Figure 2.31 is then used to find the pitch angle (θ) and the roll angle (ϕ). It is now necessary to make a small correction for the initial assumption that $\theta = 0$. To accomplish this, correction factors are used in an iterative procedure to account for the effect of flow angularity on the ratio p_{avg} / p_{02} . The correction factors for the probe can be calculated based upon the angular calibration data. Figure 2.33 shows a plot of the correction factors, which have the following form:

$$\psi = \frac{(p_{avg} / p_{02})_{\theta}}{(p_{avg} / p_{02})_{\theta=0}} \quad (2.32)$$

where $(p_{avg} / p_{02})_{\theta}$ is the quantity p_{avg} / p_{02} corresponding to a pitch angle of θ degrees and $(p_{avg} / p_{02})_{\theta=0}$ corresponds to a pitch angle of zero degrees. To proceed with the data analysis procedure, the corrected value of p_{avg} / p_{02} corresponding to $\theta = 0$ is calculated:

$$\left(\frac{p_{avg}}{p_{02}} \right)_{\theta=0} = \frac{(p_{avg} / p_{02})_{\theta}}{\psi} \quad (2.33)$$

Here, $(p_{avg} / p_{02})_{\theta}$ is the measured value of p_{avg} / p_{02} . The value $(p_{avg} / p_{02})_{\theta=0}$ is then used to obtain a second approximation for the Mach number from Figure 2.32, the calculations from equations 2.28 – 2.31 are repeated, and a second approximation for the pitch and roll angles are found from Figure 2.31. This process is then repeated iteratively until the dynamic pressure converges. At this point, the Mach number, total pressure, and flow angles have also converged. Once the flow angles are known, the Mach number components can be calculated by:

$$M_x = M_1 \sin \theta \sin \phi \quad (2.34)$$

$$M_y = -M_1 \sin \theta \cos \phi \quad (2.35)$$

$$M_z = M_1 \cos \theta \quad (2.36)$$

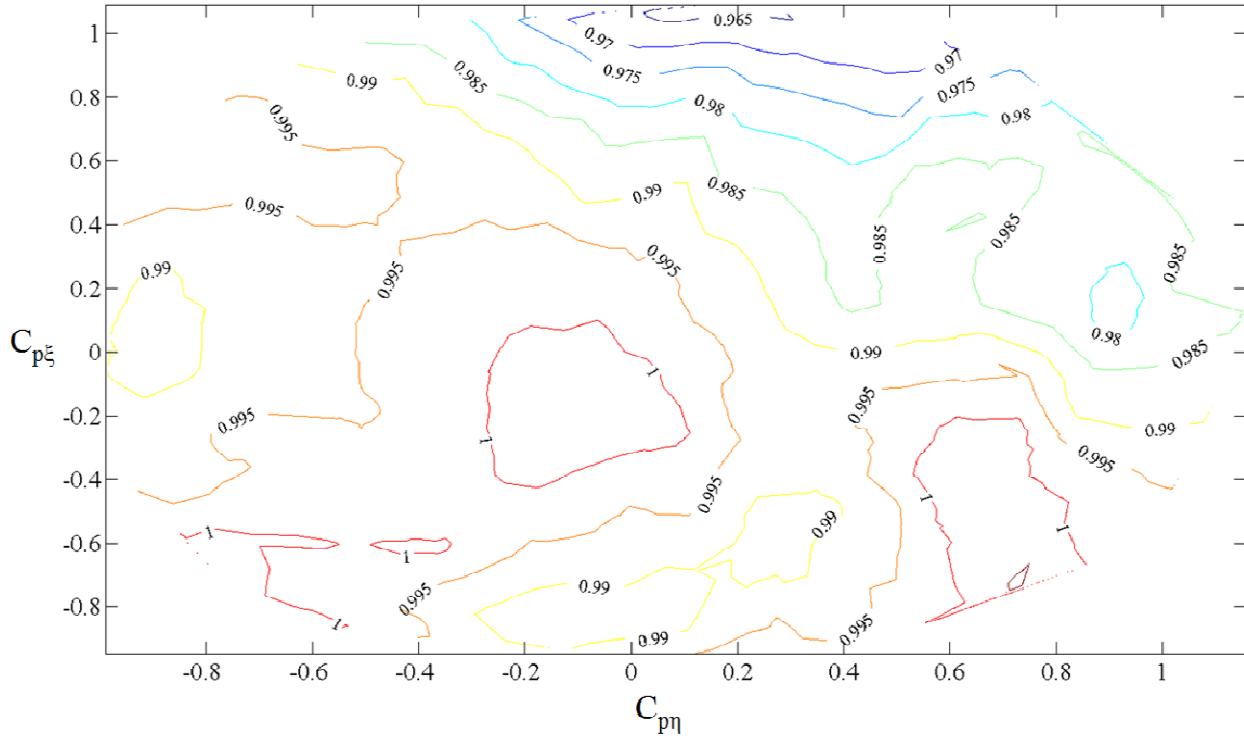


Figure 2.33: Five-hole probe correction factor map

The correction factor map shown in Figure 2.33 appears somewhat irregular in shape. The correction factor magnitudes are also very small due to the sharp, 45° half-angle of the probe. Nevertheless, using a validation procedure, it was proven that the correction factors improved the accuracy of the data analysis code when flow angularity was present (refer to Appendix C).

2.3.7.3 Measurement Uncertainty

Table 2.1 shows the estimated measurement uncertainties for the five-hole probe. An uncertainty analysis for the five-hole probe is presented in Appendix C. These uncertainties only apply when the probe is being used to measure an airflow (not a gas mixture). For the corresponding uncertainties that apply when a gas mixture is being measured, refer to Section 2.4.2.1. The measurement uncertainty of the probe varies depending on its operating conditions. Uncertainty values were computed based upon the typical operating conditions that the probe encounters at freestream Mach numbers of 2, 3, and 4.

	$M_\infty = 2$	$M_\infty = 3$	$M_\infty = 4$
Mach Number Uncertainty	3.3%	4.1%	2.4%
Total Pressure Uncertainty	4.3%	10.5%	8.0%

Table 2.1: Mach number and total pressure uncertainties (+/- percent of reading) that apply when an airflow is being measured

The Mach number calibration data for the probe was obtained using boundary layer surveys at freestream Mach numbers of 2.4 and 4. This ultimately resulted in a higher uncertainty level at $M_\infty = 3$, which could likely be reduced if a boundary layer survey was also performed at $M_\infty = 3$. However, the experiments were performed at Mach 2 and 4 freestream conditions, so the uncertainties associated with these conditions are probably the most applicable to this study.

2.4 Multiple Probe Survey Method and Data Analysis Procedure

Multiple probes including the concentration probe, cone-static probe, and five-hole probe were used to determine the properties of the flowfield downstream of the injection position. Different measurement procedures were required depending on whether the measurements were being taken within the region of the injectant plume or outside the region of the plume. Additionally, there are different uncertainties associated with the measurements taken in the two different regions due to the variations in the measurement procedures. The measurement procedures were different for these two regions primarily due to limitations in the applicability of certain calibration data.

2.4.1 Outside of the Region of the Injectant Plume

Outside of the region of the plume, the gas composition is known to be entirely air, so the concentration probe is not used in this region. The five-hole probe Mach number calibration is valid and the angular calibration is most accurate in this region. Therefore, the five-hole probe alone can be used outside of the plume to determine local values of Mach number, total pressure, and flow angularity. The data reduction process needed to convert the port pressures into incoming flow properties exactly follows that of Centolanzi⁴⁸ as shown in Section 2.3.7.2.

2.4.1.1 Measurement Uncertainty

Outside of the region of the injectant plume, the uncertainties shown in Table 2.1 apply.

2.4.2 Within the Region of the Injectant Plume

Inside the region of the plume, the properties of the mixture must be accounted for, and the data analysis procedure is more complex. First, a concentration probe survey is used to determine the local gas composition. Next, a method is needed to solve for the Mach number in the region of the plume, since the five-hole probe Mach number calibration is not valid for gas mixtures. To determine the Mach number in this region, a multiple probe survey method is used. Corresponding data points are taken with the concentration probe, the cone-static probe, and the five-hole probe. The helium or methane concentration data is then used with a combination of normal shock relations and a numerical solution of the Taylor-Maccoll equation for the local gas composition to determine the local Mach number at each measurement location (refer to Appendix A for further detail). Once the Mach number at each measurement location is known, the total pressure and flow angularity can be solved for using equations 2.28 – 2.31 and Figure 2.31, since the five-hole probe flow angularity calibration is valid for gas mixtures. However, no iterations are performed using the correction factors shown in Figure 2.33, since the influence of mixture composition on the correction factor map is unknown. The uncertainty that results from not using the correction factors for gas mixtures is accounted for and calculated as part of the uncertainty analysis for this procedure.

2.4.2.1 Measurement Uncertainty

Table 2.2 shows the estimated uncertainties for Mach number and total pressure that apply when a gas mixture is being measured using the multiple probe survey method. An uncertainty analysis for the multiple probe survey method is presented in Appendix C. The accuracy of the method degrades as flow angularity increases due to the lack of iterations to correct for flow angularity. However, the flow angles encountered in the experiments were typically small (usually in the range of 0° - 5°), so the effect of flow angularity on the data analysis procedure is minimal. Furthermore, the uncertainty of the concentration probe was found to make a negligible contribution to the overall uncertainty of this procedure (regardless of whether a

helium-air mixture or methane-air mixture was being measured). Finally, the uncertainty in the Mach number measurement was not found to be highly influenced by the Mach number itself for the range of Mach numbers considered here. However, the uncertainty in the total pressure measurement is highly dependent on Mach number.

Flow Angularity (Pitch Angle)	Mach Number Uncertainty	Total Pressure Uncertainty		
		$M_\infty = 2$	$M_\infty = 3$	$M_\infty = 4$
0° - 5°	0.9%	1.2%	2.3%	3.0%
5° - 10°	1.9%	2.5%	4.9%	6.4%
10° - 15°	2.6%	3.4%	6.7%	8.8%

Table 2.2: Mach number and total pressure uncertainties (+/- percent of reading) that apply when a gas mixture is being measured

Chapter 3: Studies of a Flush-Wall Injector Array for Circular Scramjet Combustors

A flush-wall injector model for circular scramjet combustors was experimentally studied under cold-flow (non-combusting) conditions to determine its fuel-air mixing behavior. The injector model consists of sixteen inclined, round, sonic injectors distributed around the wall of a circular duct. The experiments investigated the effects of injectant molecular weight, freestream Mach number, and jet-to-freestream momentum flux ratio (\bar{q}) on the fuel-air mixing process. Helium, methane, and air injectants were studied to vary the injectant molecular weight. Furthermore, the effects of the freestream Mach number on the mixing process were also investigated by running experiments at nominal freestream Mach numbers of 2 and 4, which simulates combustor conditions for nominal flight Mach numbers of 5 and 10. Additionally, experiments were also performed that independently varied the value of \bar{q} . These experiments were performed to support the needs of an integrated experimental and computational research program, which has the goal of upgrading the turbulence models that are used for CFD predictions of the flow inside a scramjet combustor. This chapter focuses primarily on the experiments that were performed for this research program, but a supporting CFD analysis for one of the experimental cases is also presented for discussion purposes.

3.1 Test Conditions

An array of experimental cases was studied to assess the fuel-air mixing behavior of the flush-wall injector model under different operating conditions. Table 3.1 summarizes the nominal experimental conditions for the five different test cases that were performed, identifies the extent of the measurements that were performed for each case, identifies any variations in the instrumentation used for each case, and shows the number of experimental data points measured for each case.

For the flush-wall injector, a plane 172.3 mm (83.6 injector diameters or 1.72 duct diameters) downstream of the circular injector centers was selected for data measurement purposes. At this measurement plane, which is about 2 mm beyond the end of the duct where the flow enters the test cabin, the flowfield downstream of one circular injector was surveyed. Species

concentration, Mach number, and total pressure values in the flow downstream of the injector were measured across a section of the duct. Flow angles were also measured, but these results are not presented as no regular vortical patterns were detected at the measurement plane. The lack of strong vortical structures at the measurement plane is most likely due to the far field location of the measurements. Concentration measurements began at the duct wall and continued until $\alpha < 0.01$, whereas Mach number and total pressure values were measured all the way from the duct wall to the duct centerline. Typically, only one half side of the injectant plume created by a single injector was surveyed in detail, but points were also measured on the opposite side of the plume to check for symmetry about the injector centerline. For some cases, data was only measured in a vertical profile along the centerline of the injector. For these cases, points were still measured on each lateral side of the injector to check for symmetry.

The experimental cases and the extent of the measurements performed for each case were mainly selected based upon the needs of the computational side of the research program, which required validation data for turbulence model upgrades under a certain range of conditions. Moreover, particular parameters for the different experimental cases were matched for cross comparison purposes. Values that were matched between cases are highlighted in blue in Table 3.1. The jet-to-freestream momentum flux ratio (\bar{q}) was matched for several cases with varying injectants to obtain a similar amount of injectant plume penetration for each injectant. The total injectant mass flow rate for the combination of all 16 injectors ($\dot{m}_{j,total}$) was also matched between certain cases for cross comparison purposes.

The boundary layer thickness was measured at the exit of each nozzle for the hypersonic tunnel and found to be approximately 3 mm and 7 mm at Mach numbers 2 and 4, respectively. The nozzle exit is located 100 mm upstream of the injection position, but the growth of the boundary layer in this region is expected to be small. Therefore, for the flush-wall injector model, $\delta/d \approx 1.5$ at Mach 2 conditions and $\delta/d \approx 3.4$ at Mach 4 conditions.

Experimental Conditions					
Injectant	Helium	Methane	Air	Helium	Helium
M_∞	3.9	3.9	3.9	3.9	2.0
\bar{q}	1.71	1.71	1.71	2.28	2.24
$\dot{m}_{j,total}$ [g/s]	22.5	47.3	62.7	30.0	22.5
f	0.0098	0.0206	0.0273	0.0131	0.0106
u_j / u_∞	1.31	0.62	0.47	1.31	1.71
ρ_j / ρ_∞	0.99	4.38	7.69	1.32	0.77
$p_{0j} / p_{0\infty}$	0.35	0.39	0.38	0.46	1.97
M_j	1.0	1.0	1.0	1.0	1.0
$p_{0\infty}$ [atm]	13.0	13.0	13.0	13.0	2.28
$T_{0\infty}$ [K]	295	295	295	295	295
Test Details					
Conc. Measurements	Half Plume	Injector Centerline	N/A	Half Plume	Injector Centerline
5-Hole Measurements	Half Plume	Injector Centerline	Half Plume	None	Half Plume
Injection System	Fig. 2.14 (Conc. & Cone-Static)	Figure 2.15	Figure 2.15	Figure 2.14	Figure 2.15
	Fig. 2.15 (5-Hole)				
Conc. Probe	Angled	Angled	N/A	Angled	Straight
Data Points (Conc.)*	116	42	N/A	90	30
Data Points (5-Hole)	131	40	132	N/A	123

Table 3.1: Flush-wall injector test matrix (includes nominal experimental conditions)

* Includes points measured to check for symmetry. The number of data points measured with the cone-static probe was slightly less than or equal to the number of points measured with the concentration probe.

For the $M_\infty = 2$, helium injection case, concentration measurements were initially performed across half of the injectant plume. However, due to the fast mixing that was encountered for this case, the relative uncertainties in the measured concentration values were found to be large (since the helium concentration levels were low). Thus, concentration measurements are only presented along the injector centerline for this case, where the concentrations are the highest so the uncertainties are the lowest. Nevertheless, Mach number and total pressure measurements were made for half of the plume by applying the assumption that the gas composition was entirely air. Due to the low helium concentration levels, this assumption induces only a small amount of error. Accounting for this assumption, the uncertainties associated with the Mach number and total pressure measurements for this case are approximately 3.7% and 4.8%, which is only a small increase to the uncertainty values for $M_\infty = 2$ conditions that were reported in Table 2.1. The uncertainty increase was estimated by solving the Taylor-Maccoll equation for a 45° cone for both the true gas composition and the assumed gas composition, which allowed the uncertainty contribution from the gas composition assumption to be calculated. This uncertainty contribution was then combined with the $M_\infty = 2$ uncertainty values from Table 2.1 using the method presented in Appendix C.

3.2 Concentration Measurements

The results of the concentration measurements for the $M_\infty = 4$ cases with helium injection where the flowfield downstream of one half of the injector was surveyed are shown in Figure 3.1. The results are presented as mass fraction contours across a section of the duct and assume symmetry about the injector centerline, which was verified. Additionally, the results of the concentration measurements performed along the injector centerline for all cases are shown in Figure 3.2. Furthermore, calculations were performed for each case to provide parameters that characterize the injectant plume and mixing behavior, which are shown in Table 3.2. Here, α_{max} is the maximum injectant mass fraction, $y_{\alpha,max}$ is the vertical distance from the duct wall to the location of α_{max} , y_{CM} is the vertical distance from the duct wall to the center of mass of the plume, A_{pl} is the over-stoichiometric plume area, and w_{pl} is the over-stoichiometric plume width. A_{pl} and w_{pl} were only calculated for the $M_\infty = 4$, helium injection cases, since these were the only cases where sufficient data was taken to perform these calculations. Helium was used to safely

simulate hydrogen fuel for these cases, so the stoichiometric value for a hydrogen-air mixture (.0292) was used as a metric for the calculations of A_{pl} and w_{pl} .

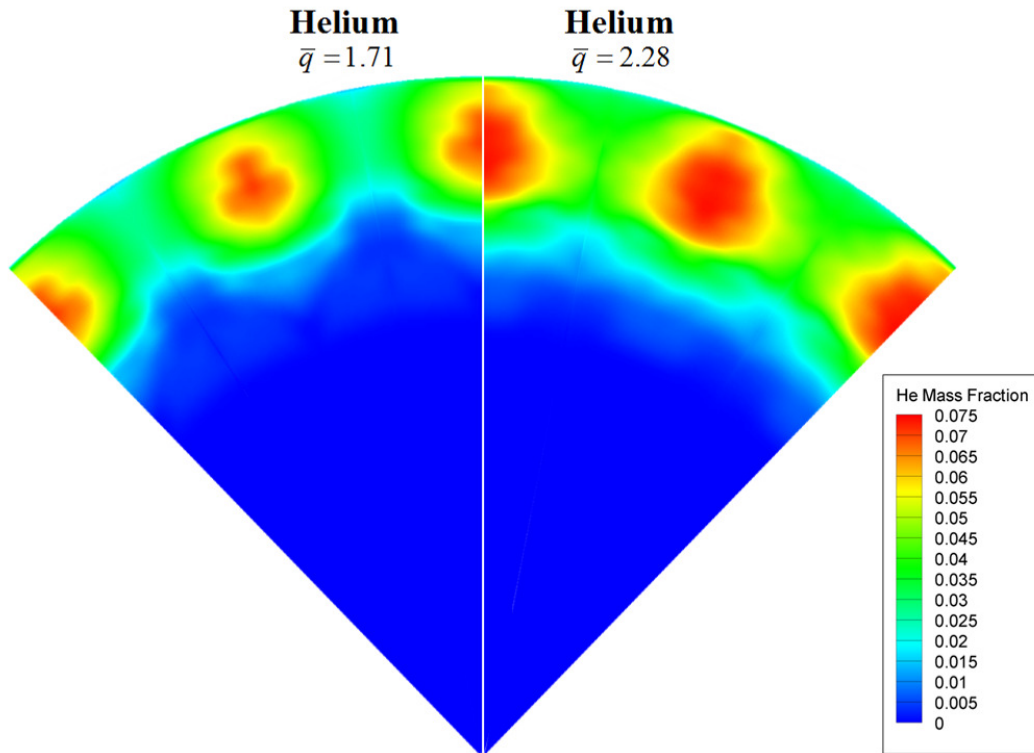


Figure 3.1: Experimental mass fraction contours for the flush-wall injector, $M_\infty = 4$, He injection cases

$Y / D = 0.5$ represents the duct wall location and $Y / D = 0$ represents the duct centerline

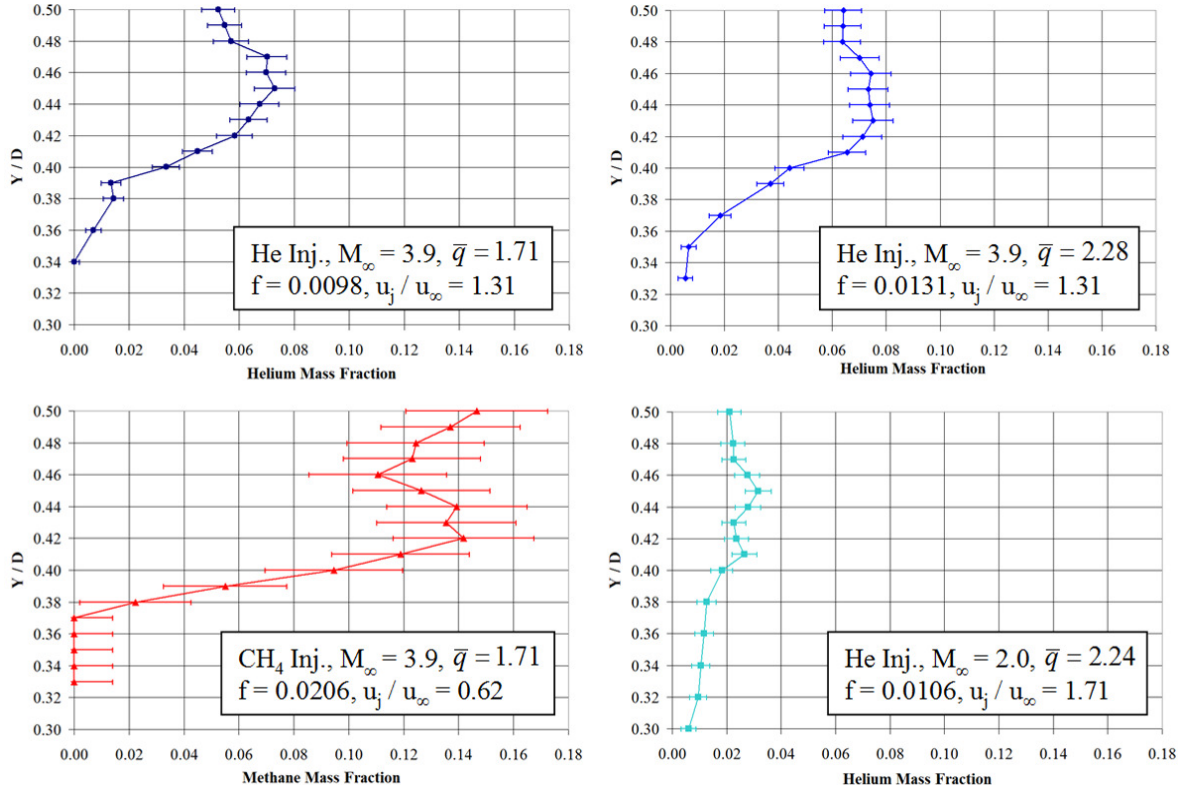


Figure 3.2: Experimental mixing results along the injector centerline for the flush-wall injector model

Injectant	Experimental Case			
	Helium (Baseline)	Methane	Helium	Helium
M_∞	3.9	3.9	3.9	2.0
\bar{q}	1.71	1.71	2.28	2.24
f	0.0098	0.0206	0.0131	0.0106
u_j / u_∞	1.31	0.62	1.31	1.71
α_{max}	0.073	0.142*	0.075	0.032
$y_{a,max}$ [mm]	5.0	8.0*	7.0	5.0
y_{CM} [mm]	5.1	5.2	5.6	7.4
A_{pl} [mm ²]	126.0	-	184.1	-
w_{pl} [mm]	15.3	-	19.5	-

Table 3.2: Flush-wall injector mixing results (for the plume created by a single circular injector)

* Excludes data point measured at the duct wall ($\alpha = 0.147$)

Considering the helium injection, $M_\infty = 4$, $\bar{q} = 1.71$ case as the baseline, comparisons to the other cases can be made using Figures 3.1-3.2 and Table 3.2 to determine the effects of the parameters that were independently varied. Molecular weight effects can be examined by comparing the baseline case to the corresponding methane injection case (M_∞ and \bar{q} were held constant). Mach number effects can be analyzed by comparing the baseline case to the corresponding $M_\infty = 2$ case [injectant gas (helium) and $\dot{m}_{j,total}$ were held constant]. Furthermore, the effects of \bar{q} can be examined by comparing the baseline case to the corresponding $\bar{q} = 2.28$ case [injectant gas (helium) and M_∞ were held constant].

The relative mixing rates for the different cases can be evaluated by comparing values of the maximum injectant mass fraction (α_{max}) while also considering the fuel-air ratio (f) for each case (since α_{max} scales with f). Furthermore, how the velocity ratio compares to 1 (i.e. is u_j / u_∞ greater than, less than, or equal to 1) for each case also influences α_{max} , so this effect must be accounted for as well. If $u_j / u_\infty \approx 1$, turbulence and mixing will be inhibited. If $u_j / u_\infty \gg 1$ or if $u_j / u_\infty \ll 1$, turbulence will be produced by shear and mixing will be promoted (refer to Section 1.4.2 for further detail). The effect of the velocity ratio on α_{max} can be summarized as follows: α_{max} dependent upon the absolute value $|u_j / u_\infty - 1|$.

The relative amount of injectant plume penetration for the different cases can be evaluated by comparing values of y_{CM} or $y_{\alpha,max}$. In the following discussion, only values of y_{CM} are compared as these values are based upon multiple data points, whereas the value of $y_{\alpha,max}$ is based upon a single data point resulting in higher uncertainty for $y_{\alpha,max}$ in comparison to y_{CM} .

Using Figure 3.2 and Table 3.2 to compare the methane injection case to the baseline case reveals that α_{max} for the methane case is approximately double that of the baseline case. However, the fuel-air ratio for the methane case is also about double that of the baseline case. Thus, since α_{max} scales with fuel-air ratio, there is not a significant difference in the mixing rates for the two cases. Furthermore, the values of $|u_j / u_\infty - 1|$ for the two cases are similar, so this factor is not likely to have a strong effect on the mixing behavior. Additionally, the location of the center of mass of the plume (y_{CM}) is nearly the same for both cases. Thus, both cases showed

about the same amount of injectant plume penetration for the same \bar{q} as might be expected. Therefore, we can conclude that for these experimental cases, molecular weight effects did not significantly influence the amount of penetration or mixing rate of the injectant.

Comparing the $M_\infty = 2$ case with helium injection to the baseline case reveals that α_{max} for the $M_\infty = 2$ case is less than half that of the baseline case. Furthermore, the fuel-air ratio for the $M_\infty = 2$ case is slightly higher than that of the baseline case. With these considerations, it is evident that the mixing rate for the $M_\infty = 2$ case was faster than that of the baseline case. The differing mixing rates can be explained for the most part by the differences in the velocity ratios of the two cases. The value of $|u_j / u_\infty - 1|$ for the $M_\infty = 2$ case has a larger value than that of the baseline case (0.71 vs. 0.31), which lead to faster mixing. In addition, the $M_\infty = 2$ case has a 45% higher value of y_{CM} than the baseline case, which indicates greater penetration for this case. This is expected as the $M_\infty = 2$ case has a higher value of \bar{q} than the baseline case. Thus, it can be concluded that for these experimental cases, reducing the Mach number from 4 to 2 results in an increase in both the penetration and the rate of mixing of the injectant.

Comparing the $M_\infty = 4$, helium injection, $\bar{q} = 2.28$ case to the baseline case using Figure 3.1, Figure 3.2, and Table 3.2 shows that the penetration, plume area, and plume width all increased for the $\bar{q} = 2.28$ case. The penetration increased by 10% (according to y_{CM}), the plume area increased by 46%, and the plume width increased by 27%. Moreover, α_{max} was only 3% higher for the $\bar{q} = 2.28$ case despite a 34% increase in the fuel-air ratio and no change in velocity ratio in comparison to the baseline case. This indicates a faster rate of mixing for the $\bar{q} = 2.28$ case. The conditions for the $\bar{q} = 2.28$ case are likely more desirable, because there was more fuel coverage across the combustor cross-section, yet the value of α_{max} was nearly the same at the measurement plane indicating approximately the same required combustor length. To summarize the comparison of these two cases, as the value of \bar{q} increased from 1.71 to 2.28, these measurements demonstrated an increase in penetration, plume area, plume width, and a faster rate of mixing.

3.3 Mach Number and Total Pressure Measurements

The results of the Mach number and total pressure measurements for the cases where the flowfield downstream of one half of the injector was surveyed are shown in Figures 3.3 – 3.5. The results are presented as Mach number and total pressure contours across a section of the duct and assume symmetry about the injector centerline. Additionally, the results of the Mach number and total pressure measurements performed along the injector centerline for all cases are shown in Figures 3.6 – 3.7. For the $M_\infty = 4$, helium and methane injection cases, these plots were generated using the multiple probe survey method and data analysis procedure (refer to Section 2.4.2). For the air injection case and the $M_\infty = 2$, helium injection case, the plots were generated based upon the five-hole probe data alone (refer to Section 2.4.1). In the case of the $M_\infty = 2$, helium injection case, this involved the assumption that the gas composition was entirely air due to the low measured helium concentrations, which was discussed earlier. In all of these figures, the local total pressure is normalized with the freestream total pressure. When making total pressure comparisons between cases, it should be noted that the total pressure of the injector manifold varies depending upon the injectant (refer to Table 3.1), which has a small influence on the total pressure results presented in Figures 3.4 and 3.7.

For all of the experimental cases, the Mach number and total pressure are reduced in the region of the plume. The reduction in Mach number is partly due to the sonic conditions of the fuel jet and partly because the incoming airstream has passed through the bow shock ahead of and around each jet. Total pressure is dependent upon Mach number, so a reduction in Mach number generally results in a corresponding reduction in total pressure as well. Some of the experimental cases exhibit singularities in the total pressure plots, which are likely due to shock waves that form inside the duct. According to the supporting CFD analysis (refer to Section 3.4), the data measurement plane is downstream of a three-dimensional shock system that forms inside the duct due to the interaction of multiple injector bow shocks. The properties of Mach number and total pressure change rapidly across a shock wave. Furthermore, if an oblique shock impinges upon the tip of the five-hole probe, this can result in localized errors in the data analysis.

A comparison of the $M_\infty = 4$, helium, methane, and air injection cases yields further insights regarding injectant molecular weight effects. All of these cases show nearly the same amount of injectant penetration according to the Mach number and total pressure data. Thus, molecular weight effects did not have a significant effect on penetration. Moreover, the Mach number and total pressure results along the injector centerline in the region of the injectant plume are similar for all three cases. Therefore, molecular weight did not have a strong effect on the properties of Mach number and total pressure along the injector centerline. However, the helium jet reduces the Mach number and total pressure in a much wider lateral region than the air jet, which is shown in Figures 3.3 – 3.4. This results in higher overall total pressure losses for the helium injection case. Therefore, injectant molecular weight may influence both the amount of lateral spreading of a jet and the overall magnitude of the total pressure losses associated with jet injection.

The increased lateral spreading of the helium jet is likely due to the higher injectant volumetric flow rate for the helium injection case. The helium injection case has an injectant volumetric flow rate that is 2.6 times that of the corresponding air injection case. Both jets penetrate about the same distance from the duct wall, which is expected as the value of \bar{q} was matched for the two jets, but the higher volume of helium must occupy a larger region of space. This ultimately results in increased lateral spreading of the jet plume for the helium injection case.

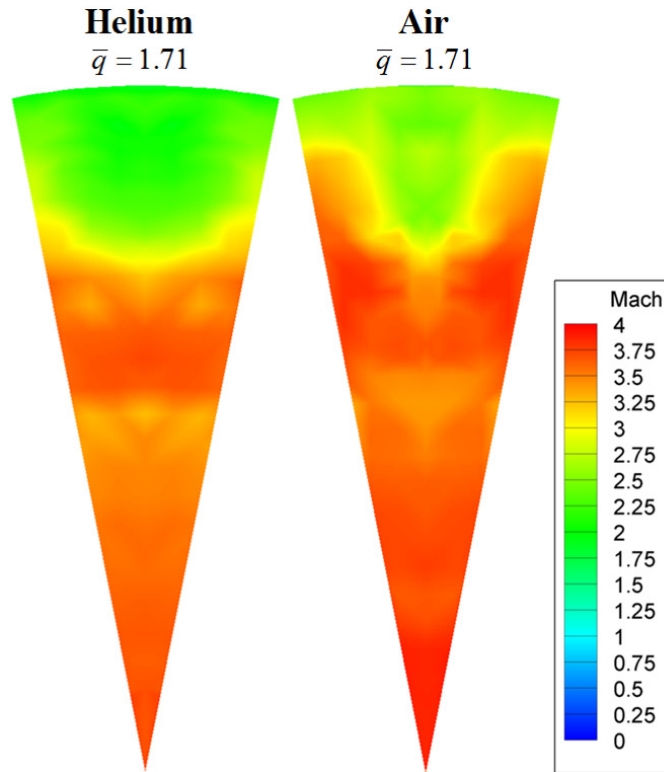


Figure 3.3: Experimental Mach number contours for the flush-wall injector, $M_\infty = 4$, He and air injection cases

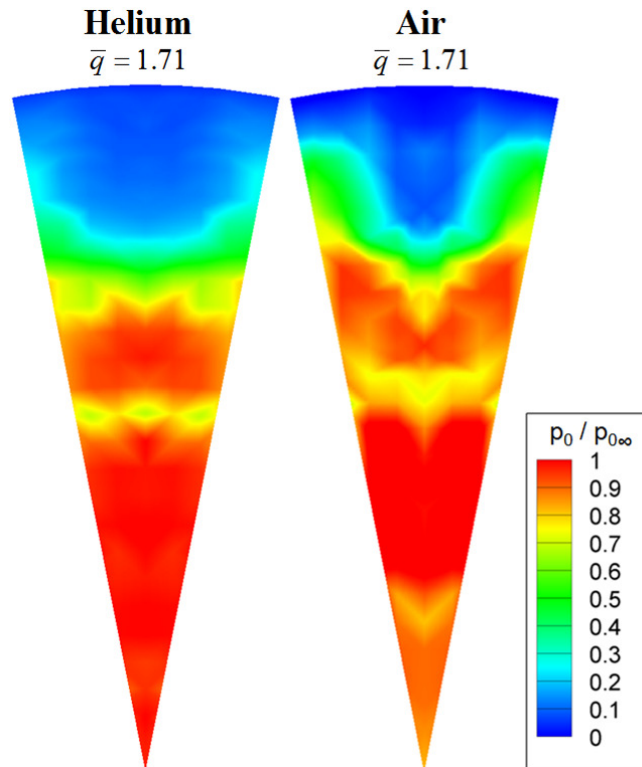


Figure 3.4: Experimental total pressure contours for the flush-wall injector, $M_\infty = 4$, He and air injection cases

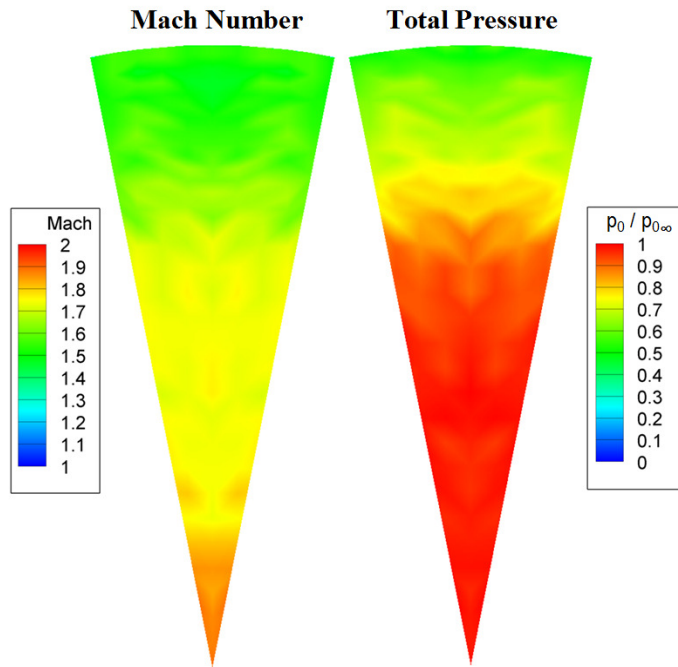


Figure 3.5: Experimental Mach number and total pressure contours for the flush-wall injector, $M_\infty = 2$, He injection case

$Y / D = 0.5$ represents the duct wall location and $Y / D = 0$ represents the duct centerline

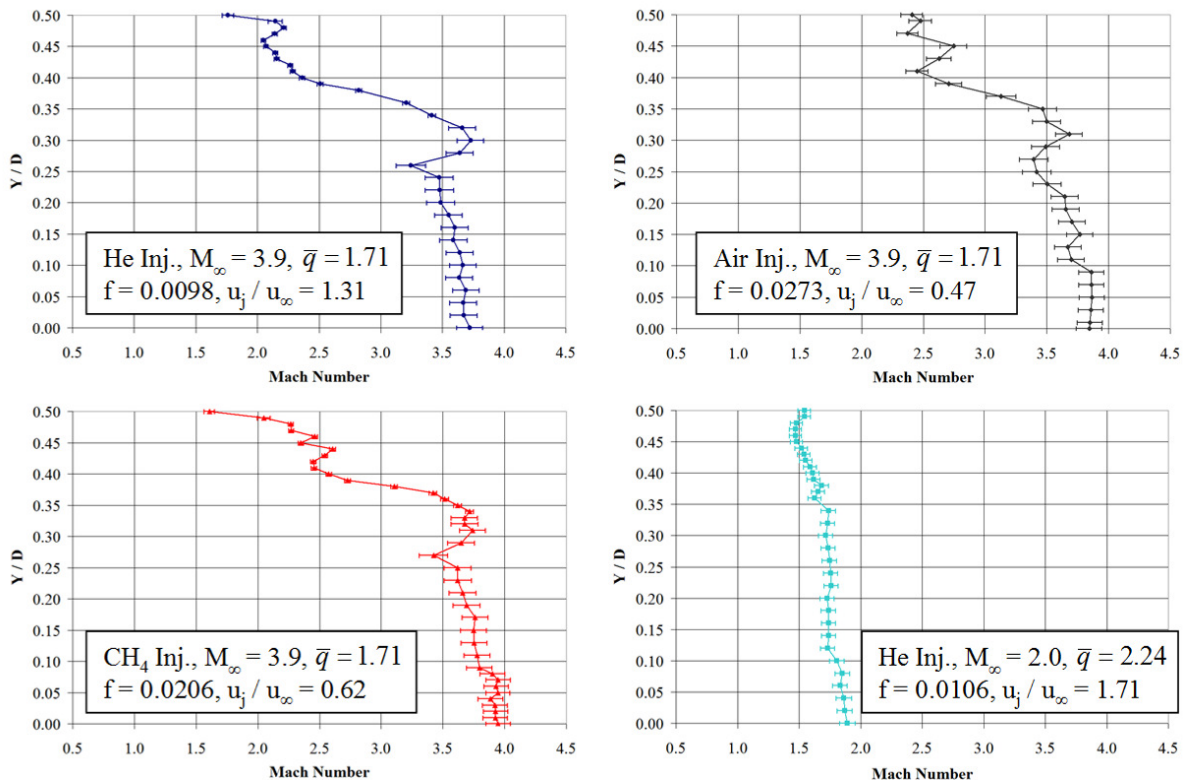


Figure 3.6: Experimental Mach number results along the injector centerline for the flush-wall injector model

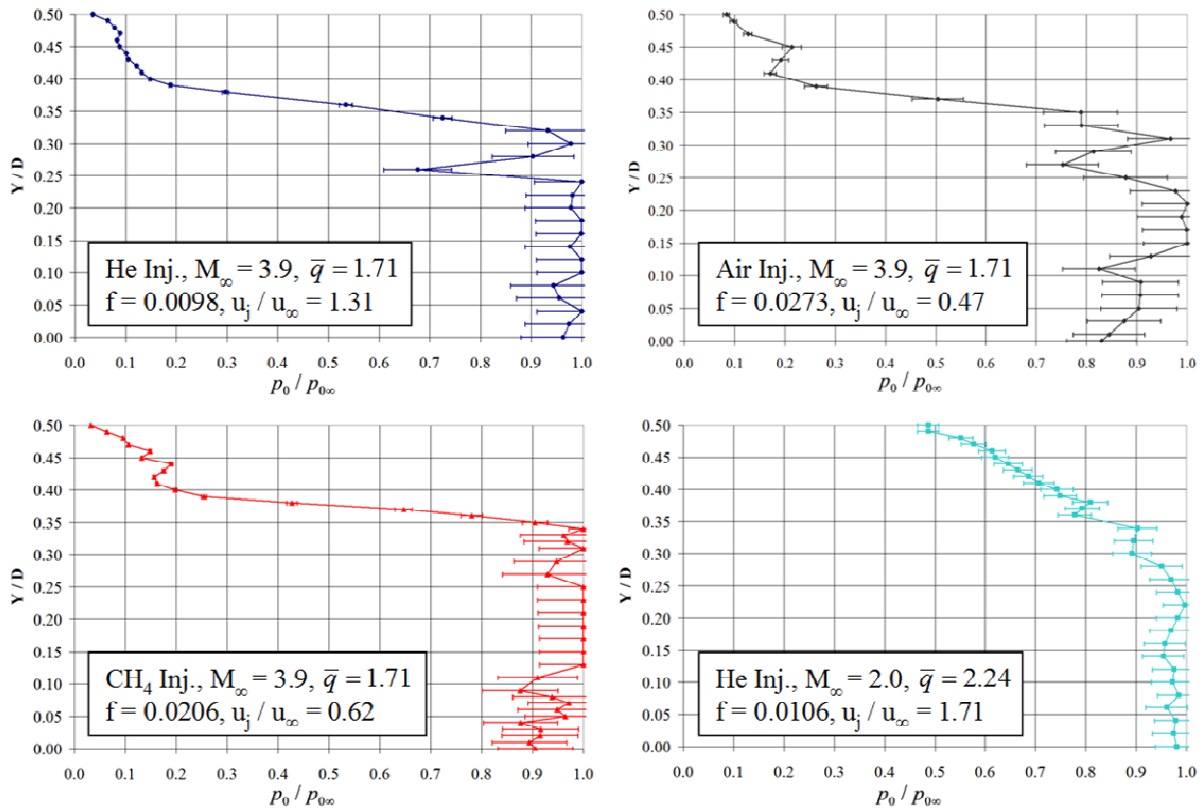


Figure 3.7: Experimental total pressure results along the injector centerline for the flush-wall injector model

This experimental data provided a substantial amount of information regarding the fuel-air mixing behavior of the flush-wall injector model under different operating conditions. Approximately 200 man hours were required to obtain this set of data, which was measured at a single axial plane downstream of the injector array. A supporting CFD analysis can complement the experiment by providing more detail about the fuel-air mixing at more locations than can be experimentally measured. For instance, the CFD analysis can predict how the injectant plume develops upstream and downstream of the measurement plane. A supporting CFD analysis for the baseline case is presented in the following section.

3.4 Supporting CFD Analysis from Collaborators

As part of the overall integrated experimental and computational study, a CFD analysis of each experimental case was performed. The CFD was performed by Ron Ungewitter from CRAFT Tech. The results of the CFD analysis provided for the baseline case (helium injection, $M_\infty = 4$, $\bar{q} = 1.71$) are presented here for discussion purposes.

The flow solver that was used for this analysis was the CRAFT Tech CRUNCH CFD[®] code, which is a RANS (Reynolds-Averaged Navier-Stokes) based unstructured CFD code that has been used extensively for scramjet calculations. The code is a multi-element flow solver for viscous, real gas systems. It incorporates a compressibility-corrected, k - ϵ turbulence model with wall functions. The turbulence model includes an additional baroclinic torque term, which was developed as part of the current research program. The baroclinic torque term is a modification to the turbulence model to account for the effects of strong density gradients, which occur in high-speed mixing flows. In high-speed mixing flows, the flow conditions deviate significantly from those used in the standard k - ϵ model derivation. The baroclinic torque term was tested and validated for a wide range of experimental cases originating from different researchers and test facilities and consisting of various flush-wall and in-stream injector designs, varying molecular weight fuels, and varying freestream Mach numbers⁴⁰. The computational grid simulates one half of one injector or 11.25 degrees of the whole model. The grid includes a section of the internal injector manifold and a total of approximately three million cells, which are primarily hexahedral in shape. Symmetry was used to represent the entire injector model with a total of 16 injectors. Additional details about the flow solver and grid as well as computational results for additional experimental cases are given in Rock et al.⁵²

Figure 3.8 shows the CFD mixing predictions of helium mass fraction for the baseline case with a side view of the duct, a three-dimensional isometric view, and a cross-sectional view of the experimental data plane. In the isometric view, several axial cuts of helium mass fraction are included along the length of the duct to show how the injectant plume develops. The injectant plume initially develops a horseshoe shape as it moves down the length of the duct. The red, three-dimensional surface shown in the isometric view encloses a region with a helium mass fraction greater than or equal to 50%, which extends approximately 12 jet diameters downstream.

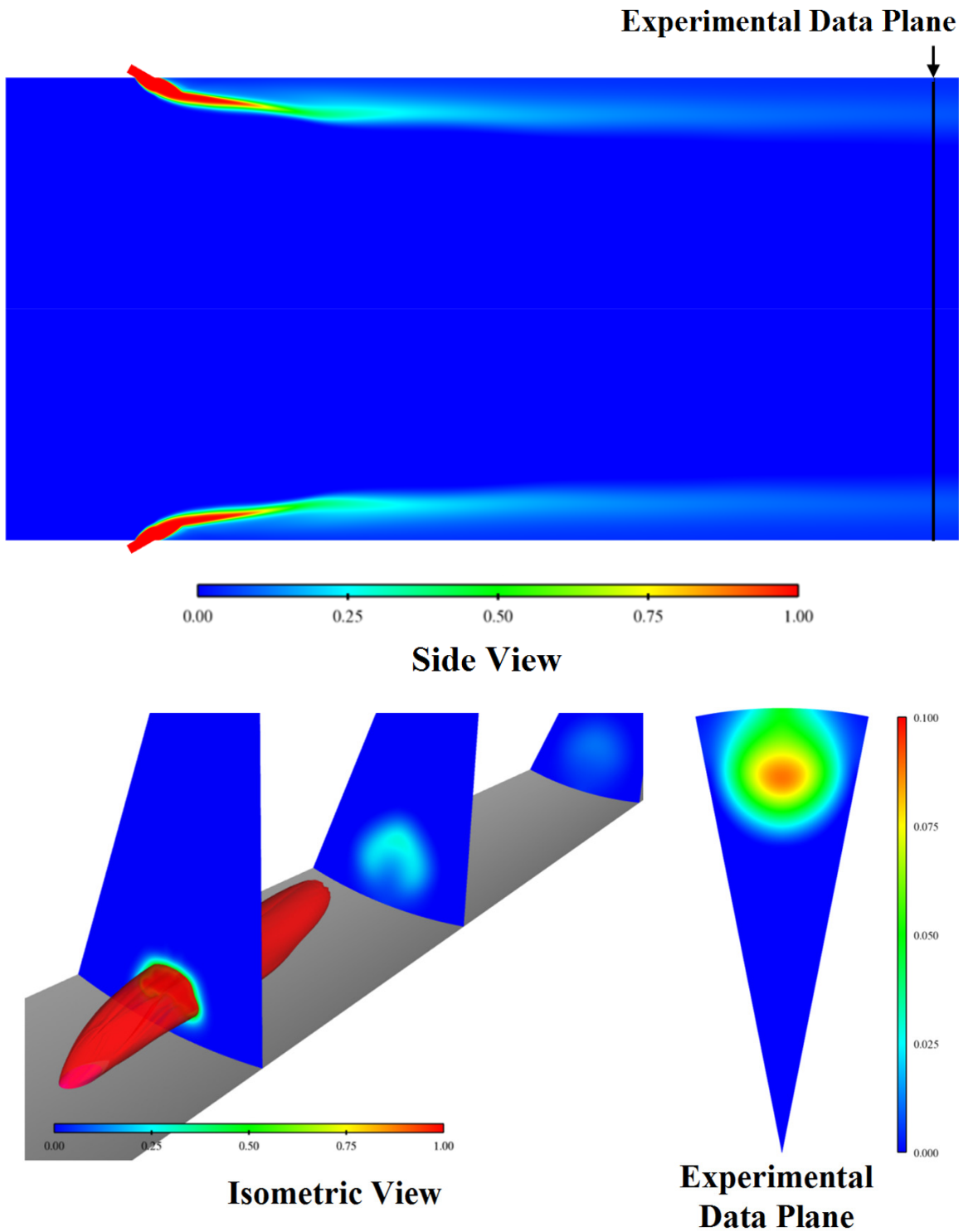


Figure 3.8: CFD mass fraction contours for the flush-wall injector, $M_\infty = 4$, He injection ($\bar{q} = 1.71$) case

Figure 3.9 shows the CFD Mach number predictions along the length of the duct with a cross-sectional view of the experimental data plane. According to the Mach number predictions, the bow shocks from opposing injectors on opposite sides of the duct interact and form a three-dimensional shock system. The experimental data plane is located downstream of the shock system that forms due to the interaction of the injector bow shocks.

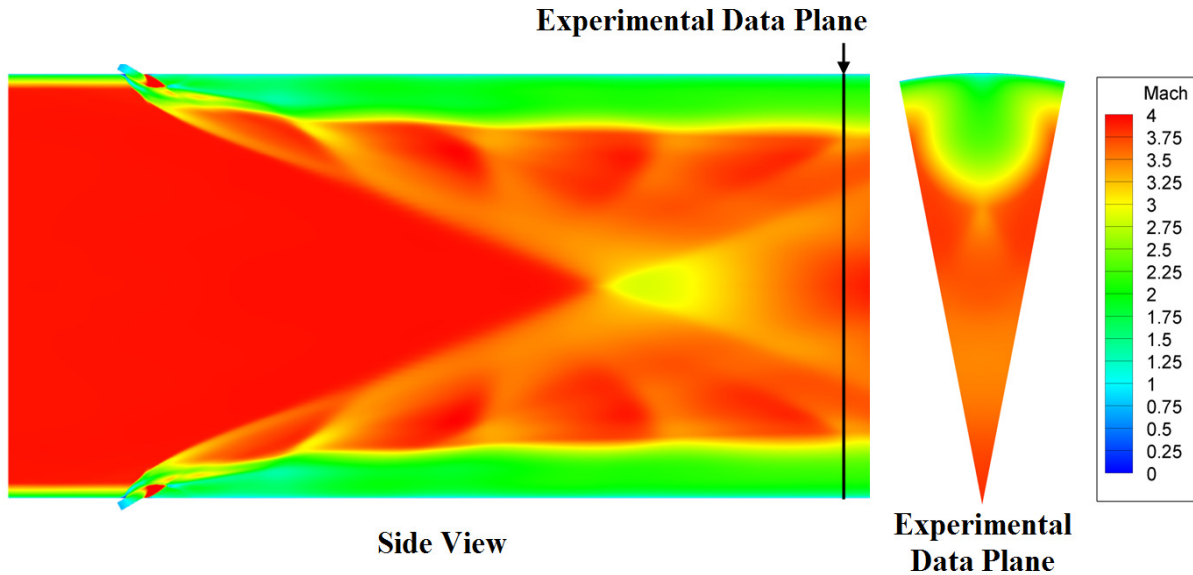


Figure 3.9: CFD Mach number contours for the flush-wall injector, $M_\infty = 4$, He injection ($\bar{q} = 1.71$) case

Figures 3.10 and 3.11 compare the mixing results from the experiment to the CFD predictions at the measurement plane. The CFD predicts the mixing reasonably well, but the penetration of the injectant plume is somewhat over-predicted. Figure 3.11 also shows the effect of the additional baroclinic torque term that was included in the k- ϵ turbulence model, which substantially improves the CFD predictions. It is also noteworthy that the uncertainties in the experimental mixing results are small enough such that the experimental results can be used to support improvements to the turbulence modeling (as evidenced by Figure 3.11).

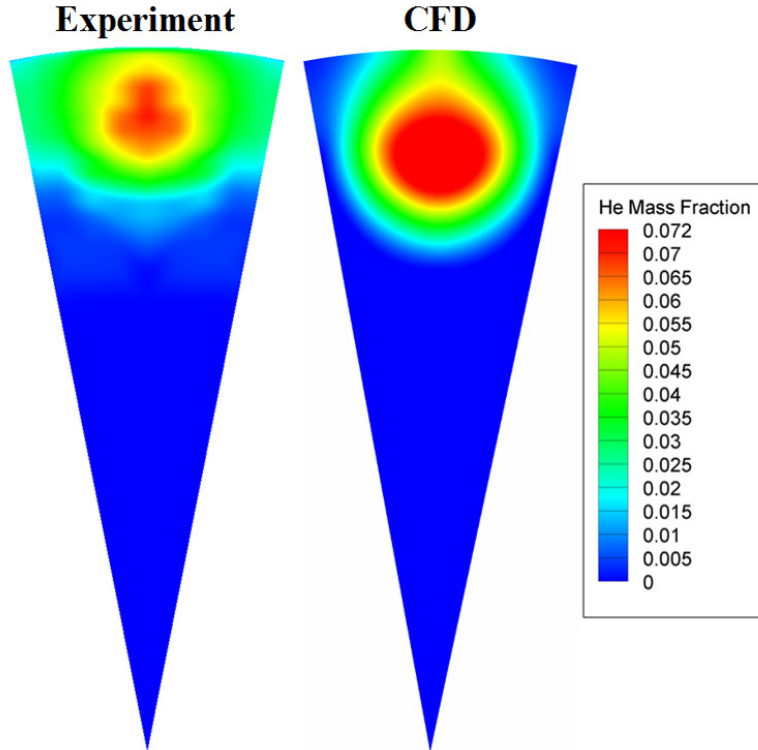


Figure 3.10: Experiment vs. CFD mass fraction contour comparison for the flush-wall injector, $M_\infty = 4$, He injection ($\bar{q} = 1.71$) case

$Y / D = 0.5$ represents the duct wall location and $Y / D = 0$ represents the duct centerline

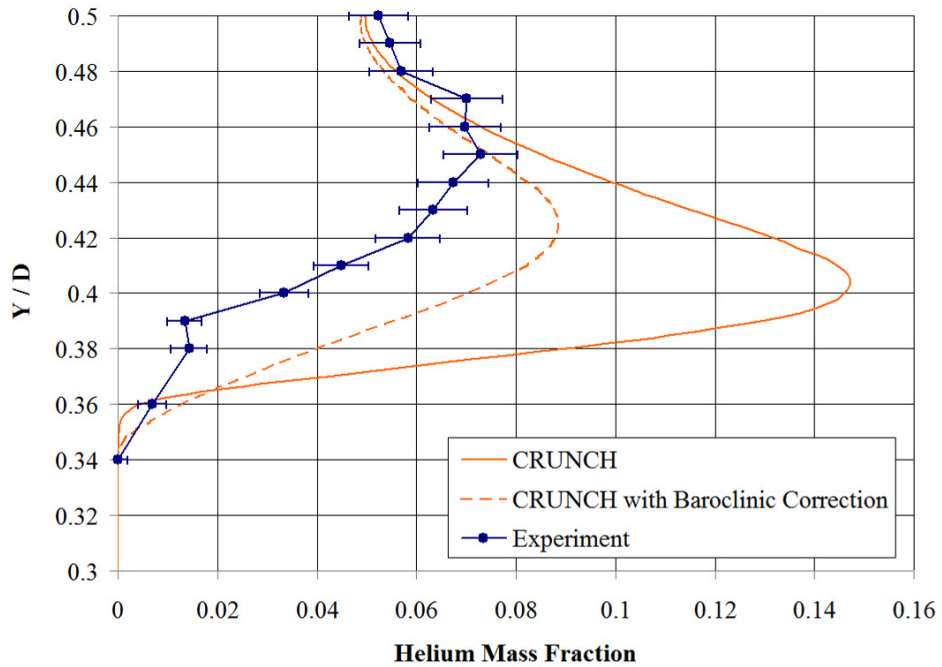


Figure 3.11: Experiment vs. CFD comparison of the mixing results along the injector centerline for the flush-wall injector, $M_\infty = 4$, He injection ($\bar{q} = 1.71$) case

Figures 3.12 and 3.13 compare the Mach number and total pressure results from the experiment to the CFD predictions at the measurement plane. In terms of the Mach number and total pressure properties, the CFD predicts the jet penetration well (not over-predicted as it was in terms of the mixing results). However, the amount of lateral spreading of the injectant plume is slightly under-predicted. Overall, the CFD predictions for the flush-wall injector model show good agreement with the experimental data.

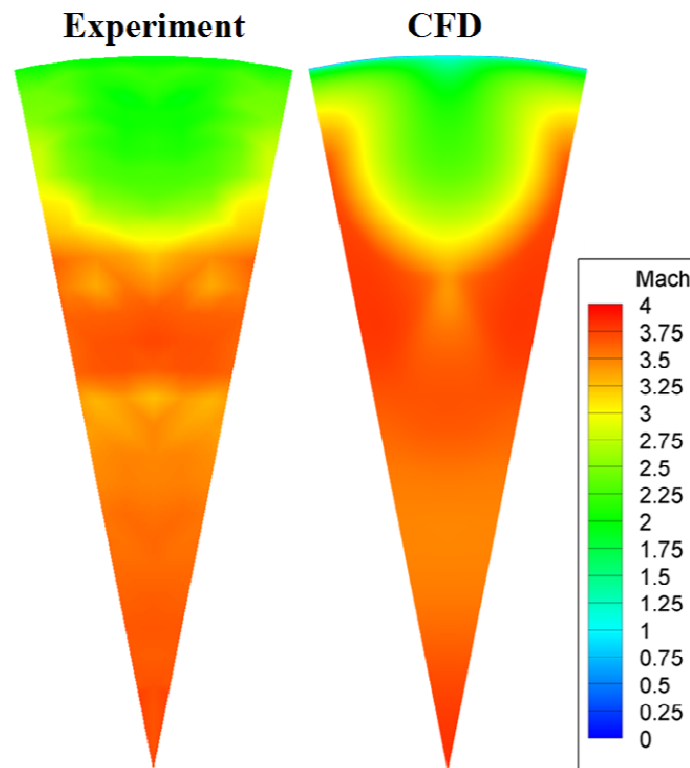


Figure 3.12: Experiment vs. CFD Mach number contour comparison for the flush-wall injector, $M_\infty = 4$, He injection ($\bar{q} = 1.71$) case

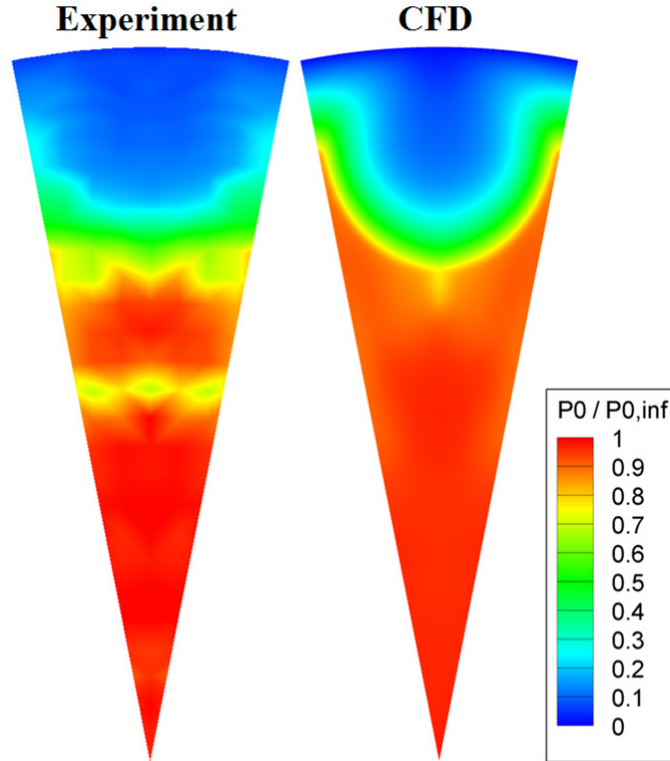


Figure 3.13: Experiment vs. CFD total pressure contour comparison for the flush-wall injector, $M_\infty = 4$, He injection ($\bar{q} = 1.71$) case

3.5 Conclusions

A flush-wall injector model for circular scramjet combustors was experimentally studied under cold-flow (non-combusting) conditions to determine its fuel-air mixing behavior. The experiments investigated the effects of injectant molecular weight, freestream Mach number, and jet-to-freestream momentum flux ratio (\bar{q}) on the fuel-air mixing process. Helium, methane, and air injectants were studied to vary the injectant molecular weight and the experiments were run at nominal freestream Mach numbers of 2 and 4. The main goal of the study was to provide validation data to support the development of turbulence model upgrades. Other goals were to assess the penetration and mixing of the simulated fuel jets and to quantify the uncertainties of the CFD predictions for the injector design.

The experimental results for the flush-wall injector obtained at 1.72 duct diameters downstream showed reasonable mixing. The maximum injectant concentrations had decayed significantly and there were modest regions of fuel-rich concentrations in the plumes (using either the

stoichiometric ratio of a hydrogen-air mixture or a methane-air mixture as a metric). Note that the overall helium-air or methane-air mixture in the duct was lean, on the same basis. The penetration of the injectant across the combustor cross-section was modest for all experimental cases, which left a substantial region of pure air along the duct centerline. Furthermore, the total pressure losses for all cases were also modest.

The primary conclusions found from the flush-wall injector study regarding the effects of injectant molecular weight, freestream Mach number, and jet-to-freestream momentum flux ratio (\bar{q}) on the fuel-air mixing process were:

- The injectant molecular weight did not significantly influence the amount of penetration or the mixing rate of the injectant.
- The injectant molecular weight influenced the amount of lateral spreading of the injectant plume. An increase in molecular weight resulted in a decrease in lateral spreading, which in turn resulted in lower overall total pressure losses.
- For helium injection, reducing the Mach number from 4 to 2 while maintaining a constant injectant mass flow rate resulted in an increase in both the penetration and the rate of mixing of the injectant. The increase in penetration can be attributed to an increase in \bar{q} , whereas the increase in mixing rate can be attributed to an increase in the quantity $|u_j / u_\infty - 1|$.
- For helium injection into a Mach 4 freestream, an increase in the value of \bar{q} from 1.71 to 2.28 resulted in an increase in penetration, plume area, plume width, and a faster rate of mixing.

CFD with a RANS formulation was used to provide detailed simulations of penetration and mixing. The CFD model was able to provide good predictions overall. Mixing and penetration were both predicted reasonably well. This level of agreement required an upgraded turbulence model, which was developed using this experimental work and also the work of other independent researchers.

Chapter 4: Studies of a Strut Injector Array for Circular Scramjet Combustors

A strut injector model for circular scramjet combustors was experimentally studied under cold-flow (non-combusting) conditions to determine its fuel-air mixing behavior. The strut injector has sixteen inclined, round, sonic injectors distributed across four struts within a circular duct. The struts are slender, inclined at a low angle to minimize drag, and have two injectors on each side. The experiments investigated the effects of injectant molecular weight and freestream Mach number on the fuel-air mixing process. Helium, methane, and air injectants were studied to vary the injectant molecular weight. Furthermore, the effects of the freestream Mach number on the mixing process were also investigated by running experiments at nominal freestream Mach numbers of 2 and 4, which simulates combustor conditions for nominal flight Mach numbers of 5 and 10. These experiments were performed to support the needs of an integrated experimental and computational research program, which has the goal of upgrading the turbulence models that are used for CFD predictions of the flow inside a scramjet combustor. This chapter focuses primarily on the experiments that were performed for this research program, but a supporting CFD analysis for one of the experimental cases is also presented for discussion purposes.

4.1 Test Conditions

An array of experimental cases was studied to assess the fuel-air mixing behavior of the strut injector model under different operating conditions. Table 4.1 summarizes the nominal experimental conditions for the four different test cases that were performed, identifies the extent of the measurements that were performed for each case, identifies any variations in the instrumentation used for each case, and shows the number of experimental data points measured for each case.

For the strut injector, a plane 180.5 mm (119 injector diameters or 1.81 duct diameters) downstream of the circular injector centers was selected for data measurement purposes. At this measurement plane, which is about 2 mm beyond the end of the duct where the flow enters the test cabin, the flow field downstream of one half of one strut was surveyed. To check for

symmetry, data points were also measured on the opposite side of the strut. For all cases, the symmetry plane for the injectant plume was found to be shifted approximately 1 to 2 mm laterally in the $-X$ direction relative to the centerline of the strut. This slight 1-2 mm shift of the injectant plume over a length of 178.3 mm is most likely attributed to a small, but undetected misalignment of the experimental hardware. For some cases, data was only measured in a vertical profile along the centerline (symmetry plane) of the injectant plume. Before these measurements were performed, points were first measured at several lateral positions to locate the centerline of the injectant plume.

Species concentration, Mach number, and total pressure values in the flow downstream of the strut were measured across a section of the duct. Concentration measurements began at the duct wall and continued until α was either zero or rapidly declining towards zero. Mach number and total pressure values were measured all the way from the duct wall to the duct centerline. Flow angles were also measured, but these results are not presented as no regular vortical patterns were detected at the measurement plane. The lack of strong vortical structures at the measurement plane is most likely due to the far field location of the measurements.

The experimental cases and the extent of the measurements performed for each case were primarily selected based upon the needs of the computational side of the research program, which required validation data for turbulence model upgrades under a certain range of conditions. Certain parameters for the different experimental cases were matched for cross comparison purposes. Values were matched for comparing corresponding strut injector cases and also for comparison of the flush-wall injector to the strut injector. For a comparison of the experimental conditions for the flush-wall injector vs. the strut injector, refer to Table 5.1. Values that were matched between corresponding strut injector cases are highlighted in blue in Table 4.1. The jet-to-freestream momentum flux ratio (\bar{q}) was matched for several cases with varying injectants to obtain a similar amount of injectant plume penetration for each injectant. The total injectant mass flow rate for the combination of all 16 injectors ($\dot{m}_{j,total}$) was also matched between certain cases for comparison purposes.

Experimental Conditions				
Injectant	Helium	Methane	Air	Helium
M_∞	3.9	3.9	3.9	2.0
\bar{q}	3.13	3.13	3.13	4.10
$\dot{m}_{j,total}$ [g/s]	22.5	47.3	62.7	22.5
f	0.0098	0.0206	0.0273	0.0106
u_j / u_∞	1.31	0.62	0.47	1.71
ρ_j / ρ_∞	1.82	8.02	14.09	1.41
p_{0j} / p_{0_∞}	0.63	0.72	0.70	3.62
M_j	1.0	1.0	1.0	1.0
p_{0_∞} [atm]	13.0	13.0	13.0	2.28
T_{0_∞} [K]	295	295	295	295
Test Details				
Conc. Measurements	Half Plume	Plume Centerline	N/A	Plume Centerline
5-Hole Measurements	Half Plume	Plume Centerline	Half Plume	Plume Centerline
Injection System	Figure 2.16	Figure 2.16	Figure 2.16	Figure 2.16
Conc. Probe	Straight	Angled	N/A	Angled
Data Points (Conc.)*	127	46	N/A	37
Data Points (5-Hole)	186	30	176	29

Table 4.1: Strut injector test matrix (includes nominal experimental conditions)

* Includes points measured to check for symmetry. The number of data points measured with the cone-static probe was slightly less than or equal to the number of points measured with the concentration probe.

The boundary layer thickness was measured at the exit of each nozzle for the hypersonic tunnel and found to be approximately 3 mm and 7 mm at Mach numbers 2 and 4, respectively. The struts begin at the end of the nozzle and the centers of the injectors are located 92 mm from the leading edge of each strut. All of the injectors on each strut are located in positions that are expected to be outside of the duct wall boundary layer.

4.2 Concentration Measurements

The results of the concentration measurements for the case where the flowfield downstream of one half of one strut was surveyed are shown in Figure 4.1. The results are presented as helium mass fraction contours across a section of the duct. The projected outlines of the strut and the circular injectors are shown for reference. Additionally, the results of the concentration measurements performed along the centerline of the plume for all cases are shown in Figure 4.2, where the outer edge of the strut is indicated by a dashed line. Calculations were performed for each case to provide parameters that characterize the injectant plume and mixing behavior, which are shown in Table 4.2. Again, α_{max} is the maximum injectant mass fraction, $y_{\alpha,max}$ is the vertical distance from the duct wall to the location of α_{max} , y_{CM} is the vertical distance from the duct wall to the center of mass of the plume, A_{pl} is the over-stoichiometric plume area, and w_{pl} is the over-stoichiometric plume width. A_{pl} and w_{pl} were only calculated for the $M_\infty = 4$, helium injection case, since this was the only case where sufficient data was taken to perform these calculations. Helium was used to safely simulate hydrogen fuel for this case, so the stoichiometric value for a hydrogen-air mixture (.0292) was used to perform the calculations of A_{pl} and w_{pl} .

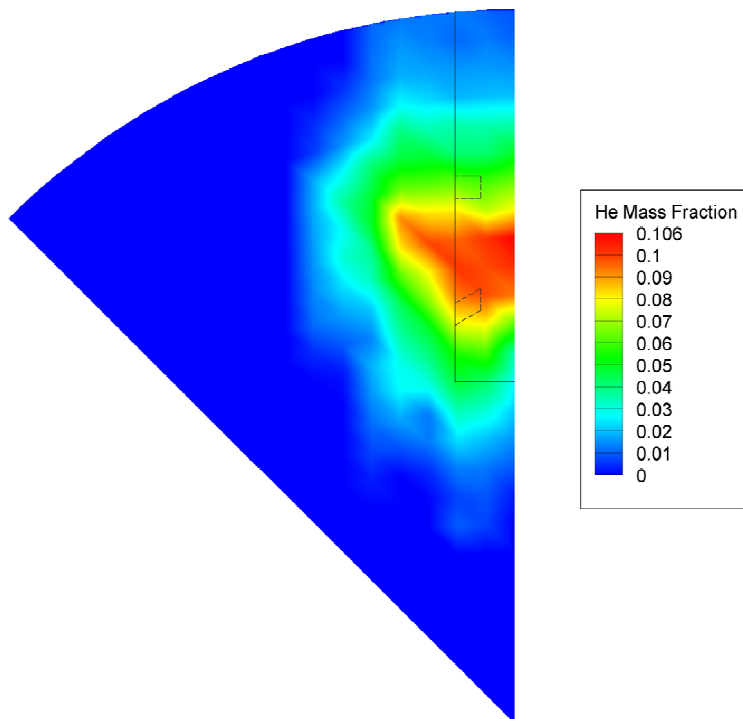


Figure 4.1: Experimental mass fraction contours for the strut injector, $M_\infty = 4$, He injection case

$Y / D = 0.5$ represents the duct wall location and $Y / D = 0$ represents the duct centerline

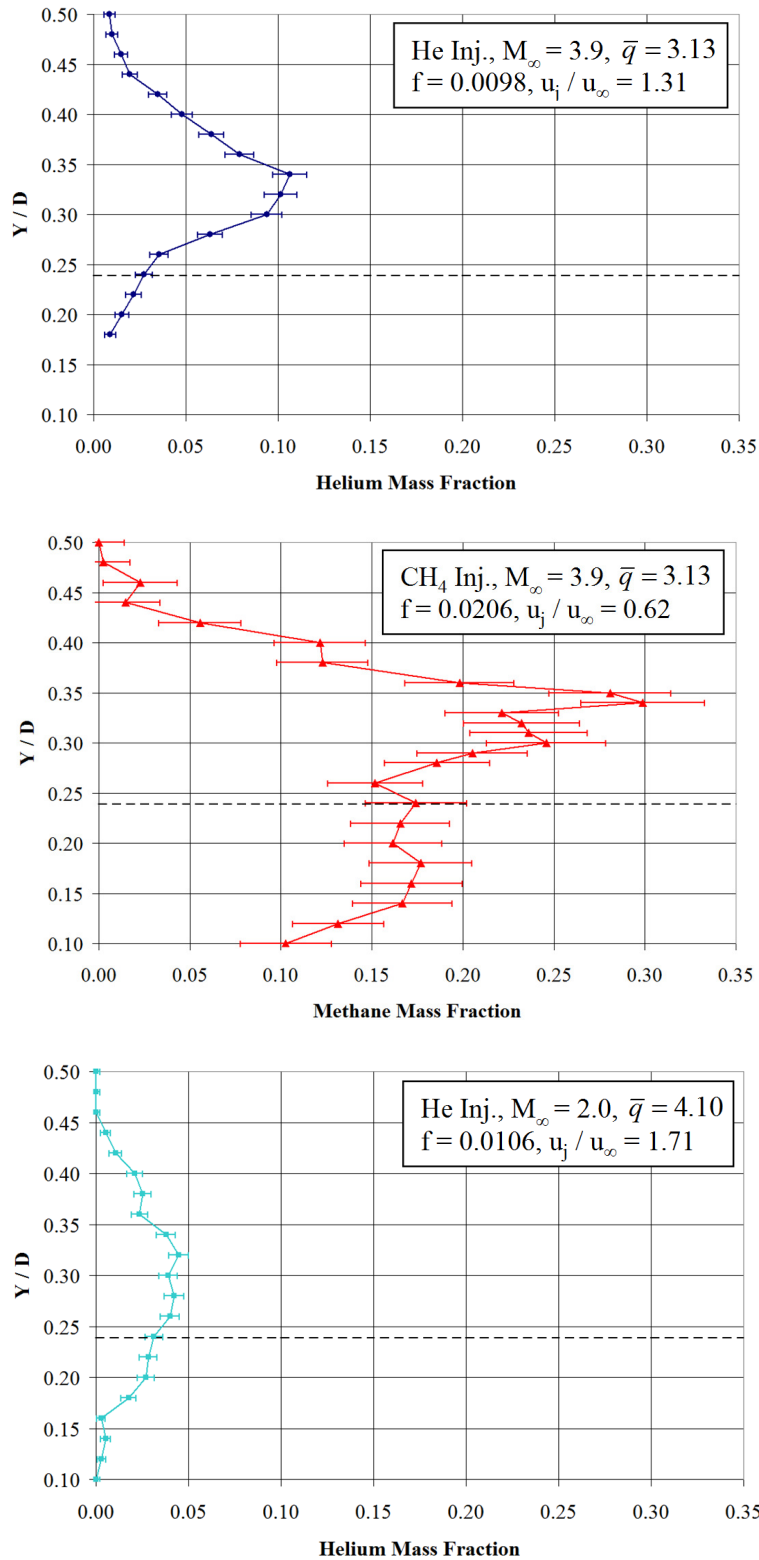


Figure 4.2: Experimental mixing results along the centerline of the injectant plume for the strut injector (the dashed line indicates the outer edge of the strut)

Injectant	Experimental Case		
	Helium (Baseline)	Methane	Helium
M_∞	3.9	3.9	2.0
\bar{q}	3.13	3.13	4.10
f	0.0098	0.0206	0.0106
u_j / u_∞	1.31	0.62	1.71
α_{max}	0.106	0.299	0.045
$y_{a,max}$ [mm]	16.0	16.0	18.0
y_{CM} [mm]	16.7	22.1	20.8
A_{pl} [mm ²]	409.0	-	-
w_{pl} [mm]	25.5	-	-

Table 4.2: Strut injector mixing results (for the plume created by an entire strut with four circular injectors)

Considering the helium injection, $M_\infty = 4$, $\bar{q} = 3.13$ case as the baseline, cross comparisons to the other cases can be made to determine the effects of the parameters that were independently varied. Molecular weight effects can be examined by comparing the baseline case to the corresponding methane injection case (M_∞ and \bar{q} were held constant). Mach number effects can be analyzed by comparing the baseline case to the corresponding $M_\infty = 2$ case [injectant gas (helium) and $\dot{m}_{j,total}$ were held constant]. The logic for comparing the relative mixing rates for the different cases follows that presented in Section 3.2. Comparisons of the amount of injectant penetration for corresponding strut injector cases cannot be made using the concentration data, because this data was only measured along the plume centerline for all cases except the baseline case. Penetration is generally considered to be measured perpendicular to the plane of an injector. Thus, the $y_{a,max}$ and y_{CM} values for the strut injector are not truly representative of penetration, but these values can be used to compare the relative location of the injectant plume within the duct. In the following discussion, the y_{CM} values are used to compare the plume location as these values have lower uncertainties.

Using Figure 4.2 and Table 4.2 to compare the methane injection case to the baseline helium case reveals that α_{max} for the methane case is approximately 2.8 times greater than that of the baseline

helium case. However, the fuel-air ratio for the methane case is only about double that of the baseline helium case. Thus, the methane injection case mixed slower than the baseline helium injection case. Furthermore, the values of $|u_j / u_\infty - 1|$ for the two cases are similar, so this factor is not likely to have had a strong effect on the mixing behavior. The location of the center of mass of the plume (y_{CM}) is 32% further from the duct wall for the methane injection case. Thus, the methane injection case projected the plume further into the combustor cross-section than the baseline helium injection case. The value of \bar{q} for these two cases was matched, so this value is not likely to contribute to this effect. Therefore, we can conclude that for these experimental cases, the higher molecular weight gas (methane) had significantly slower mixing than the lower molecular weight gas (helium) and the molecular weight difference between the two gases also influenced the location of the plume within the duct.

Comparing the $M_\infty = 2$ case to the baseline case reveals that α_{max} for the $M_\infty = 2$ case is less than half that of the baseline case. The fuel-air ratio for the $M_\infty = 2$ case is slightly higher than that of the baseline case. With these considerations, it is evident that the mixing rate for the $M_\infty = 2$ case was faster than that of the baseline case. The differing mixing rates can be explained for the most part by the differences in the velocity ratios of the two cases. The value of $|u_j / u_\infty - 1|$ for the $M_\infty = 2$ case has a larger value than that of the baseline case (0.71 vs. 0.31), which lead to faster mixing. In addition, the $M_\infty = 2$ case has a 25% higher value of y_{CM} than the baseline case, which indicates that the plume was projected further into the combustor cross-section for this case. The higher value of \bar{q} for the $M_\infty = 2$ case is a likely explanation for the plume being projected further into the combustor cross-section for this case. The injectors on each strut that are nearest to the duct centerline are inclined at a 30° angle relative to the plane of the strut (refer to Figure 4.1). These injectors generate a component of momentum in the $-Y$ direction. Therefore, increasing the value of \bar{q} for these injectors can shift the center of mass of the plume further into the combustor cross-section. To summarize, it can be concluded that for these experimental cases, reducing the Mach number from 4 to 2 results in both an increase in the rate of mixing of the injectant and further projection of the plume into the combustor cross-section.

4.3 Mach Number and Total Pressure Measurements

The results of the Mach number and total pressure measurements for the cases where the flowfield downstream of one half of one strut was surveyed are shown in Figures 4.3 – 4.4. The results are presented as Mach number and total pressure contours across a section of the duct. In addition, the results of the Mach number and total pressure measurements performed along the centerline of the injectant plume for all cases are shown in Figures 4.5 – 4.6, where the outer edge of the strut is indicated by a dashed line. The Mach number and total pressure results along the plume centerline for the $M_\infty = 4$ cases are also compared in Figures 4.7 – 4.8. For the helium and methane injection cases, these plots were generated using the multiple probe survey method and data analysis procedure (refer to Section 2.4.2). For the air injection case, the plots were generated based upon the five-hole probe data alone (refer to Section 2.4.1). In all of these figures, the local total pressure is normalized with the freestream total pressure. When making total pressure comparisons between cases, it should be noted that the total pressure of the injector manifold varies depending upon the injectant (refer to Table 4.1), which has a small influence on the total pressure results presented in Figures 4.4, 4.6, and 4.8.

In all of the experimental cases, a complex three-dimensional shock system forms downstream of the injector array, which includes oblique shocks from the struts and bow shocks from the injectors. According to the supporting CFD analysis (refer to Section 4.4), the data measurement plane is located far downstream of a region where a large number of shock interactions occur. The physical obstacle of the strut and the shock system that forms within the duct reduces the Mach number of the flow downstream of the strut as shown in Figure 4.3. Also, the injectant jets are at sonic conditions, whereas the freestream is nominally at Mach 2 or 4 conditions. There is also a substantial total pressure loss downstream of the strut itself as shown in Figure 4.4.

A comparison of the $M_\infty = 4$, helium, methane, and air injection cases yields further insights regarding injectant molecular weight effects. According to the Mach number and total pressure data, all of these cases show that the plume was projected nearly the same distance into the combustor cross-section. This is contrary to the species concentration data, which showed that the methane injection case projected the plume further into the combustor cross-section.

Comparing the Mach number results in the region of the injectant plume using Figures 4.3 and 4.7 reveals that the Mach number increases as injectant molecular weight increases. One factor that may contribute to this effect is the decrease in the injectant volumetric flow rate that occurs as the injectant molecular weight increases. The injectant volumetric flow rates are 7560 SLPM (standard liters per minute) for the helium injection case, 3970 SLPM for the methane injection case, and 2883 SLPM for the air injection case. As the injectant volumetric flow rate decreases, the obstruction to the flow becomes smaller, and the result is an increase in the Mach number of the flow in the region of the plume. Total pressure is dependent on Mach number, so the total pressure in the region of the plume also increases as injectant molecular weight increases, which is shown in Figures 4.4 and 4.8. This ultimately results in lower overall total pressure losses for higher molecular weight injectants. To summarize the comparison of these cases, some conclusions were drawn:

- According to the Mach number and total pressure data, the molecular weight of the injectant did not significantly influence how far the plume was projected into the duct cross-section.
- As the injectant molecular weight increases, the Mach number in the region of the injectant plume increases.
- As the injectant molecular weight increases, the overall total pressure losses are reduced.

This experimental data provided a substantial amount of information regarding the fuel-air mixing behavior of the strut injector model under different operating conditions. Approximately 200 man hours were required to obtain this set of data, which was measured at a single axial plane downstream of the injector array. A supporting CFD analysis can complement the experiment by providing more detail about the fuel-air mixing at more locations than can be experimentally measured. Again, the CFD analysis can predict how the injectant plume develops upstream and downstream of the measurement plane. A supporting CFD analysis for the baseline case is presented in the following section.

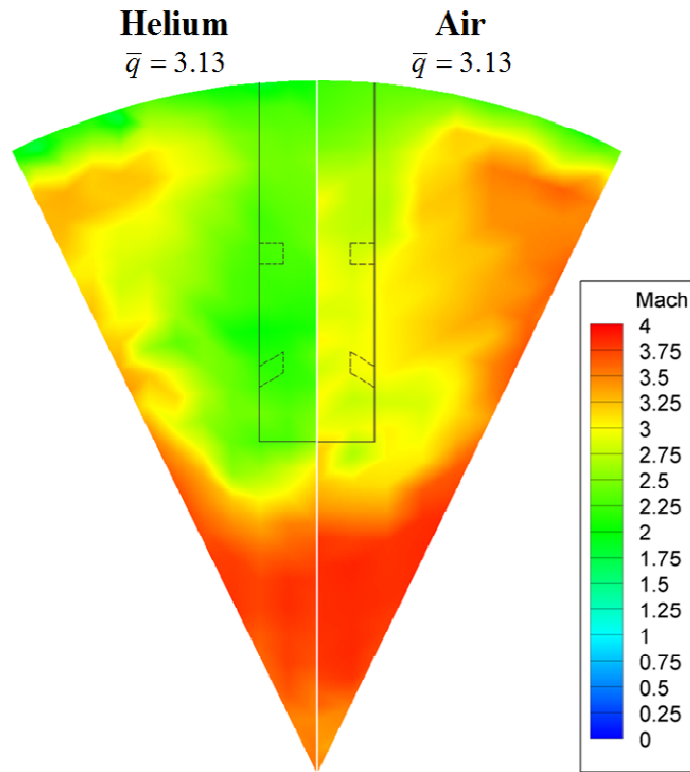


Figure 4.3: Experimental Mach number contours for the strut injector, $M_\infty = 4$, He and air injection cases

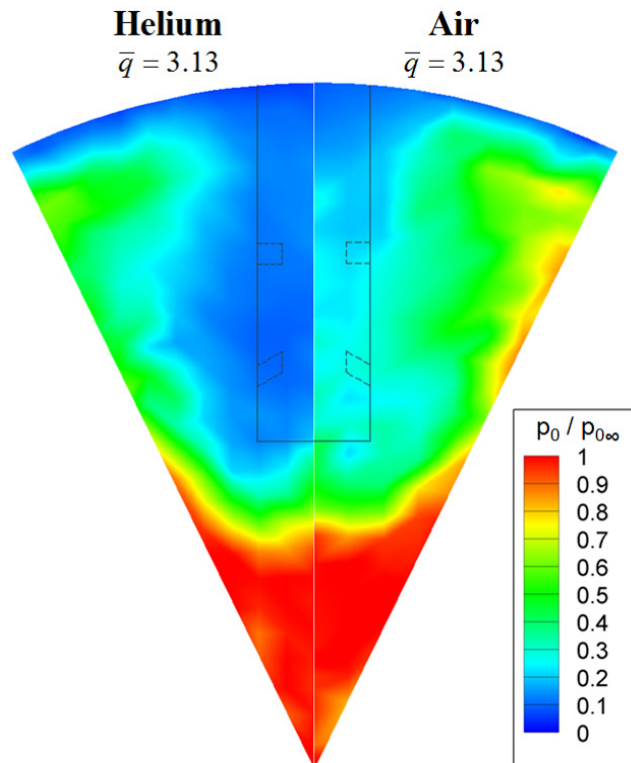


Figure 4.4: Experimental total pressure contours for the strut injector, $M_\infty = 4$, He and air injection cases

$Y / D = 0.5$ represents the duct wall location and $Y / D = 0$ represents the duct centerline

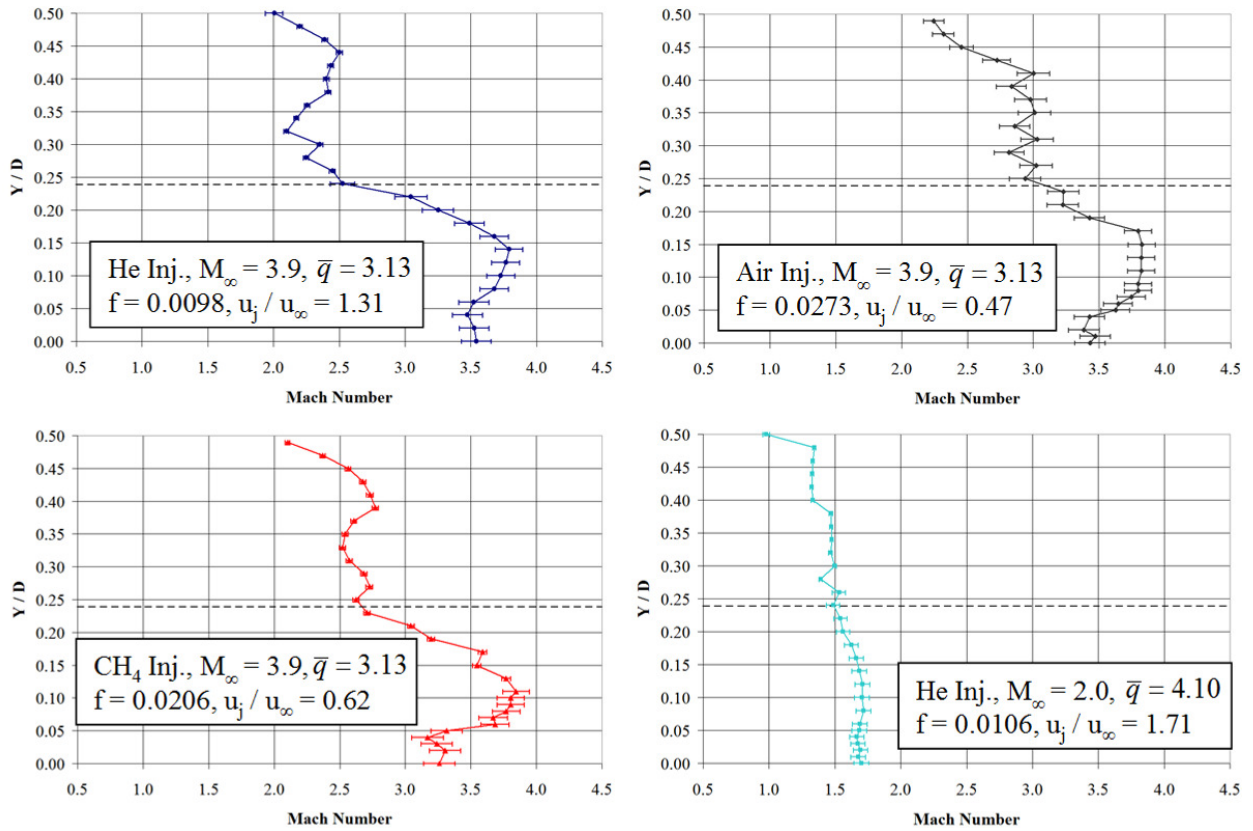


Figure 4.5: Experimental Mach number results along the centerline of the injectant plume for the strut injector model

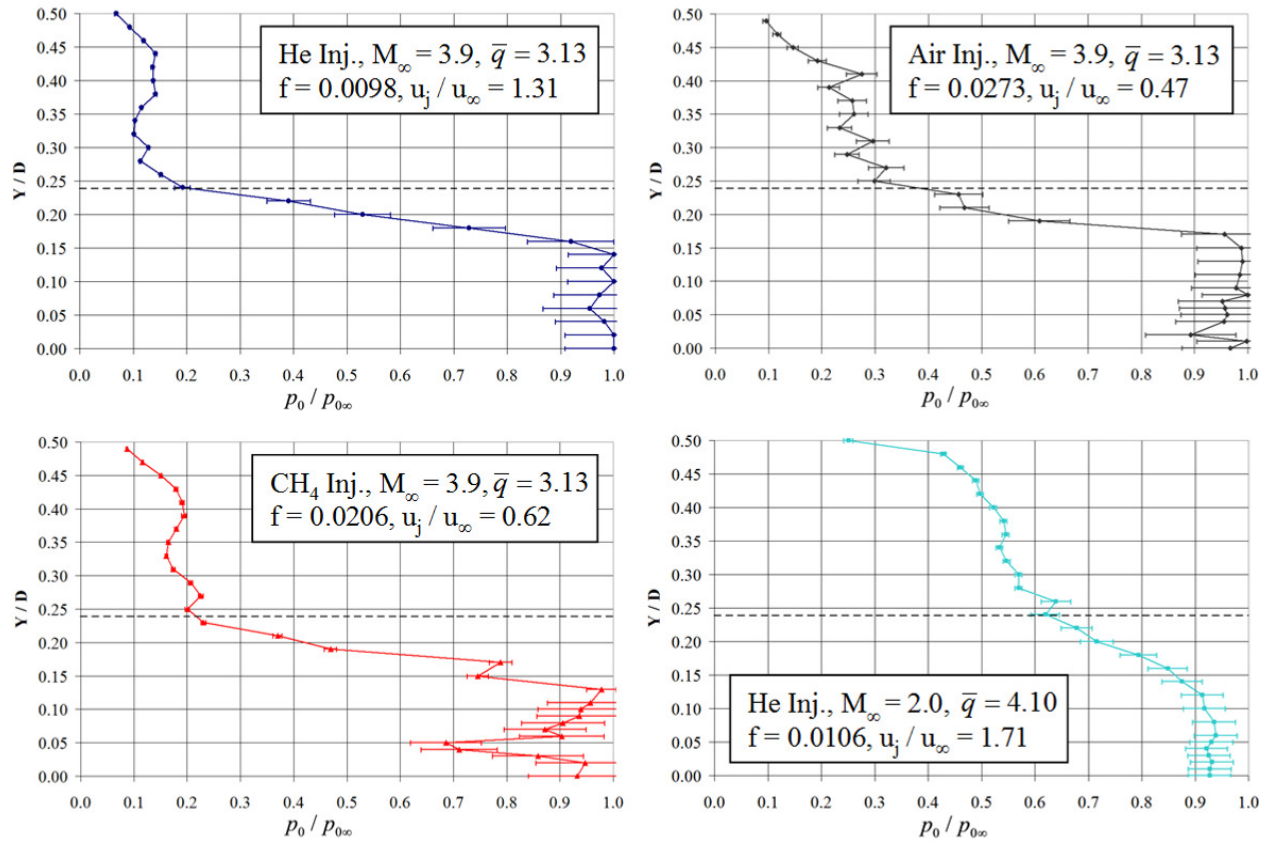


Figure 4.6: Experimental total pressure results along the centerline of the injectant plume for the strut injector model

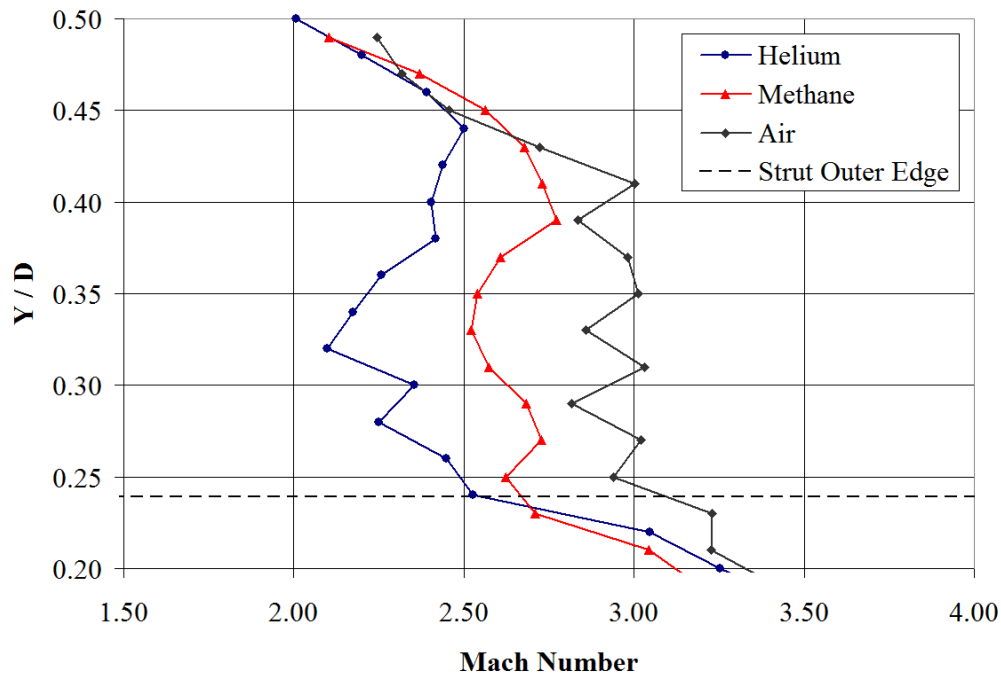


Figure 4.7: Comparison of the experimental Mach number results along the centerline of the injectant plume for the strut injector, $M_\infty = 4$ cases

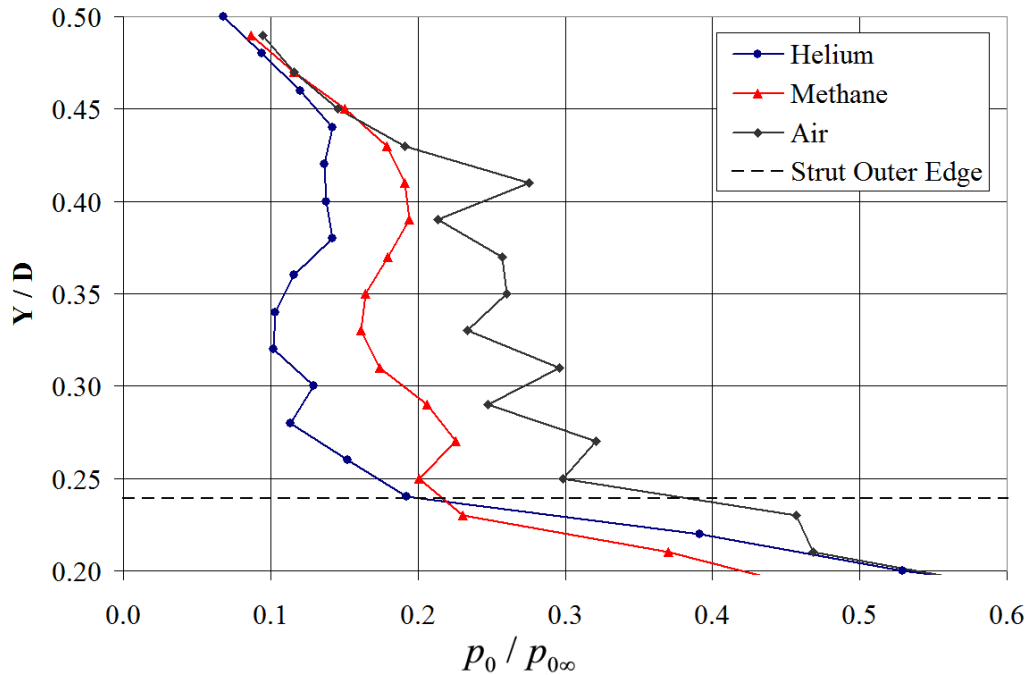


Figure 4.8: Comparison of the experimental total pressure results along the centerline of the injectant plume for the strut injector, $M_\infty = 4$ cases

4.4 Supporting CFD Analysis from Collaborators

A CFD analysis of each experimental case was performed by CRAFT Tech to support the development of the turbulence model upgrades. The results of the CFD analysis for the baseline case (helium injection, $M_\infty = 4$, $\bar{q} = 3.13$) provided by Ron Ungewitter from CRAFT Tech are presented here for discussion purposes. The flow solver that was used for this analysis was the CRAFT Tech CRUNCH CFD[®] code. For a description of the code and the basic assumptions of the analysis, refer to Section 3.4.

The computational grid for the strut injector extends from half-way between two struts to the middle of a strut and is a 45 degree slice of the actual hardware. The grid includes a section of the internal injector manifold and a total of approximately 6.05 million cells, which are primarily hexahedral in shape. Symmetry was used to represent all four struts with a total of 16 injectors. For additional details about the flow solver and grid as well as additional computational results, refer to Rock et al.⁵²⁻⁵³

Figure 4.9 shows the CFD mixing predictions of helium mass fraction for the baseline case with a three-dimensional isometric view of the duct, a side view of the duct, and cross-sectional views at six axial locations including the experimental data plane. The brown, three-dimensional surfaces shown in the isometric view enclose a region with a helium mass fraction greater than or equal to 20%. The CFD results show that the individual injectant plumes quickly merge into a single large plume, which remains entrained in the strut base region as it moves down the length of the duct.

Figure 4.10 shows the CFD Mach number predictions along the length of the duct for the baseline case. A complex three-dimensional shock system forms within the duct that includes oblique shocks from the struts, bow shocks from the injectors, and multiple shock interactions. The experimental data plane is located far downstream of a region where a large number of shock interactions occur.

Figures 4.11 and 4.12 compare the mixing results from the experiment to the CFD predictions at the experimental data plane. The CFD predicts the mixing well and also predicts the amount of lateral penetration relative to the strut well. However, the distance that the plume is projected into the combustor cross-section is somewhat under-predicted. Figure 4.12 also shows the effect of the additional baroclinic torque term that was included in the $k-\epsilon$ turbulence model, which substantially improves the CFD predictions.

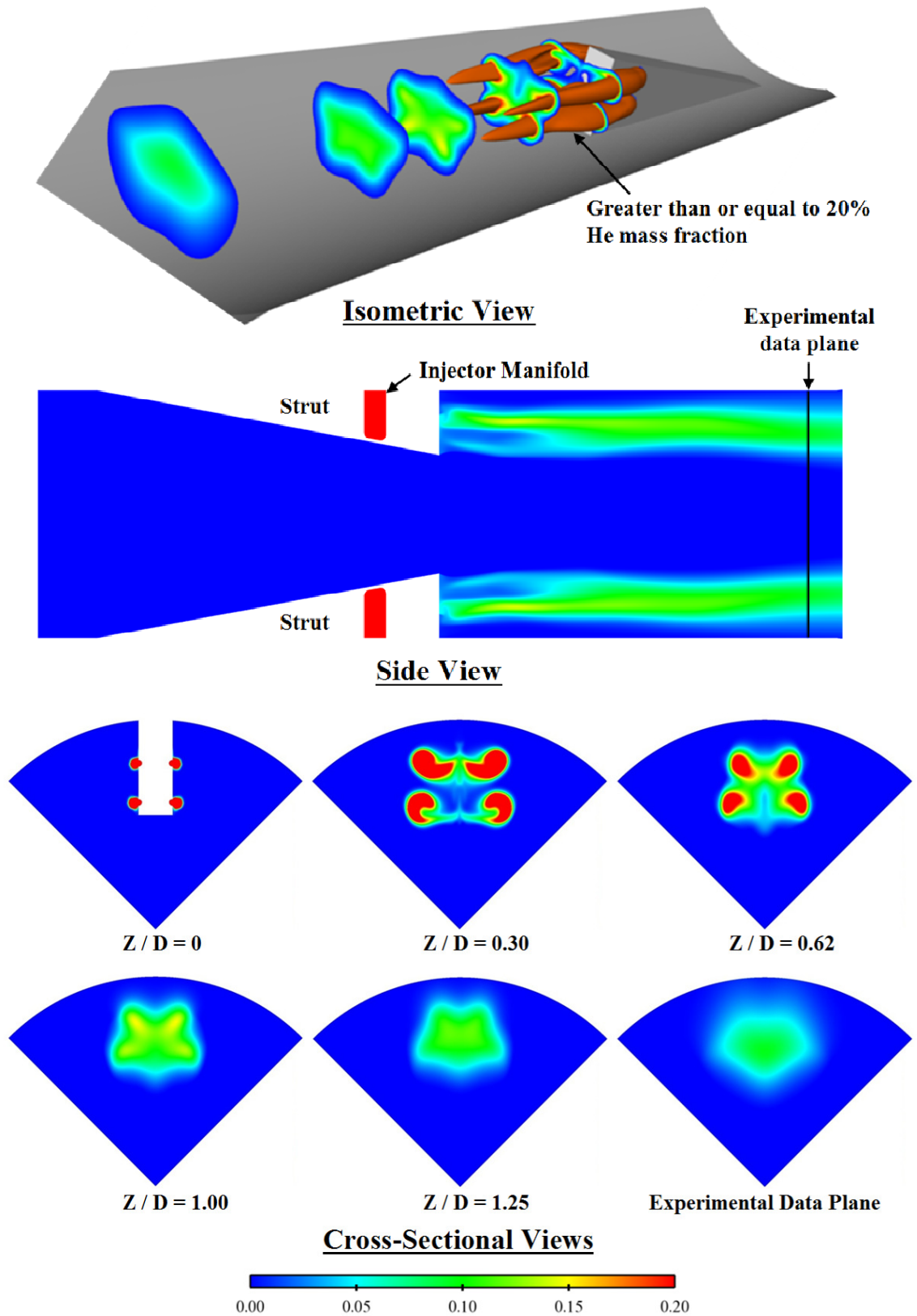


Figure 4.9: CFD mass fraction contours for the strut injector, $M_\infty = 4$, He injection ($\bar{q} = 3.13$) case

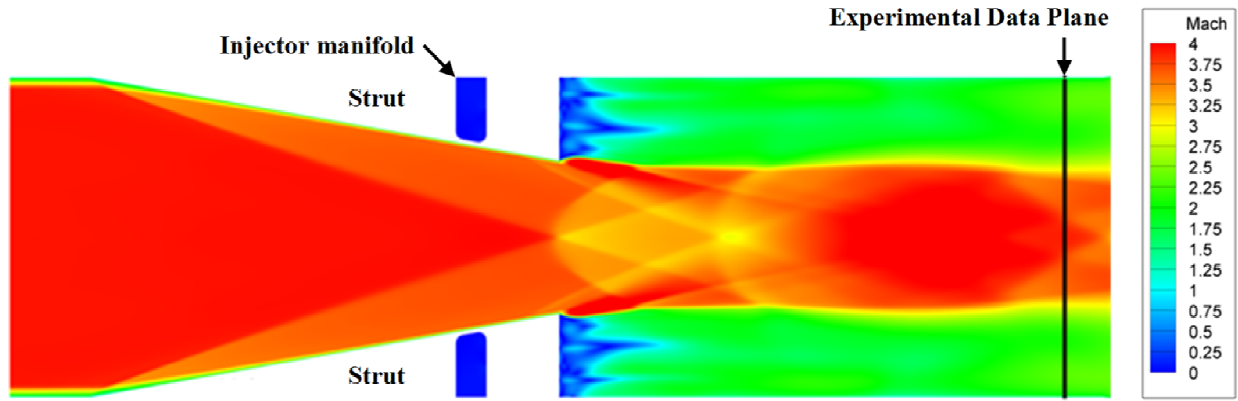


Figure 4.10: CFD Mach number contours along the length of the duct for the strut injector, $M_\infty = 4$, He injection ($\bar{q} = 3.13$) case

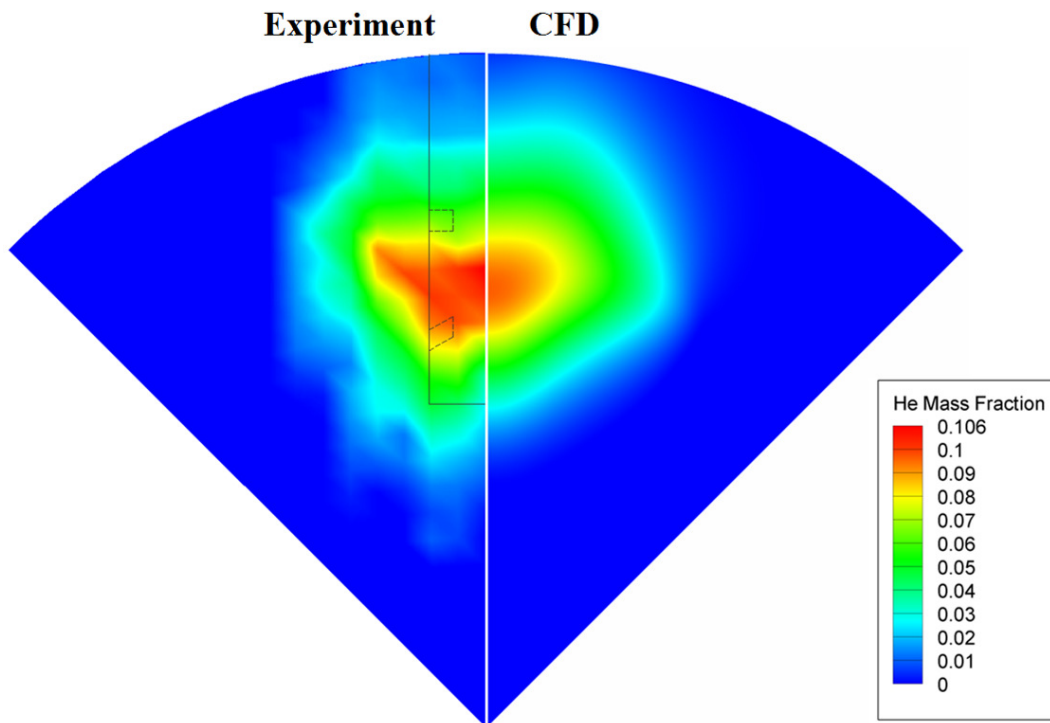


Figure 4.11: Experiment vs. CFD mass fraction contour comparison for the strut injector, $M_\infty = 4$, He injection ($\bar{q} = 3.13$) case

$Y / D = 0.5$ represents the duct wall location and $Y / D = 0$ represents the duct centerline

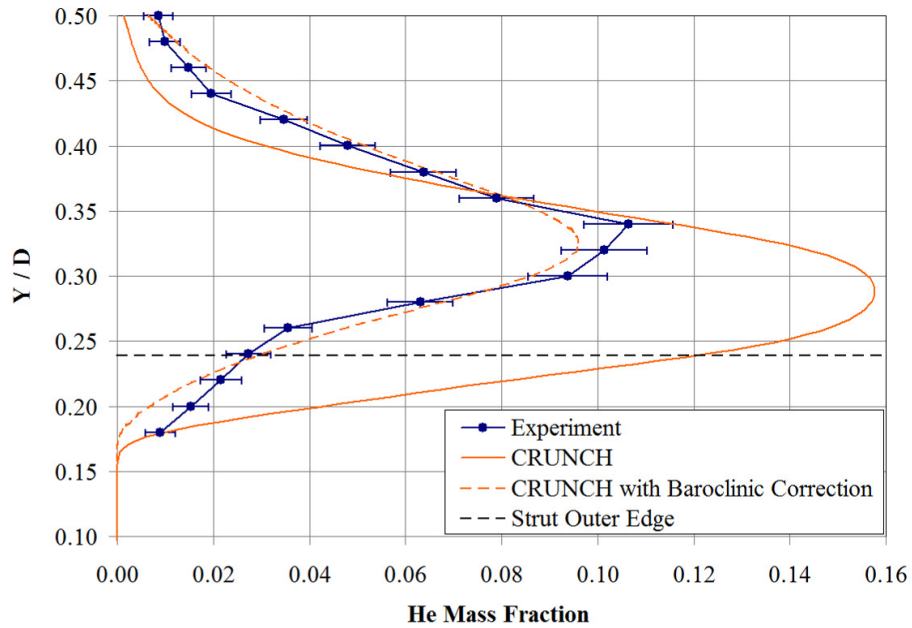


Figure 4.12: Experiment vs. CFD comparison of the mixing results along the plume centerline for the strut injector, $M_\infty = 4$, He injection ($\bar{q} = 3.13$) case

Figures 4.13 and 4.14 compare the Mach number and total pressure results from the experiment to the CFD predictions at the measurement plane. The experimental data was measured over a 26 degree section of the duct, whereas the numerical results show a 45 degree section of the duct. In Figures 4.13 and 4.14, the end of the experimental data plane is indicated by a dashed line. Overall, the CFD predictions for the strut injector model show excellent agreement with the experimental data.

The CFD predictions for the strut injector show a somewhat higher level of agreement with the experimental data than the corresponding predictions for the flush-wall injector. Both analyses were performed using the same code with the same underlying assumptions. One possible explanation behind the better CFD predictions for the strut injector is that CFD often predicts inviscid phenomena better than viscous phenomena. In the case of the strut injector, there are strong inviscid flow features such as the oblique shocks from the struts. Moreover, the boundary layer incoming to the injectors on the struts is probably thin, since the injectors are located outside of the duct wall boundary layer. However, in the case of the flush-wall injector, viscous effects are likely a much larger factor as the boundary layer incoming to the injectors is relatively thick.

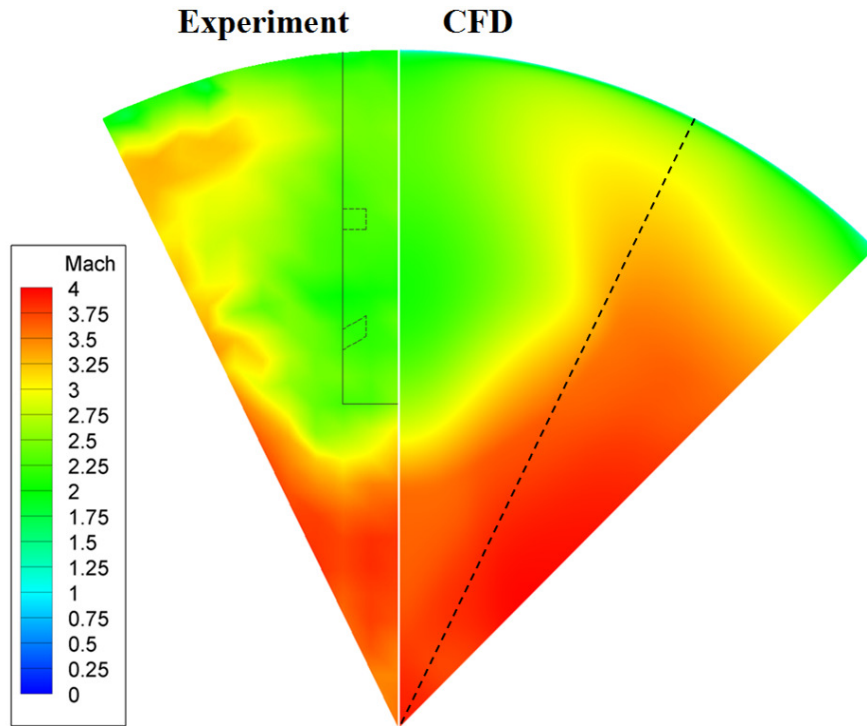


Figure 4.13: Experiment vs. CFD Mach number contour comparison for the strut injector, $M_\infty = 4$, He injection ($\bar{q} = 3.13$) case

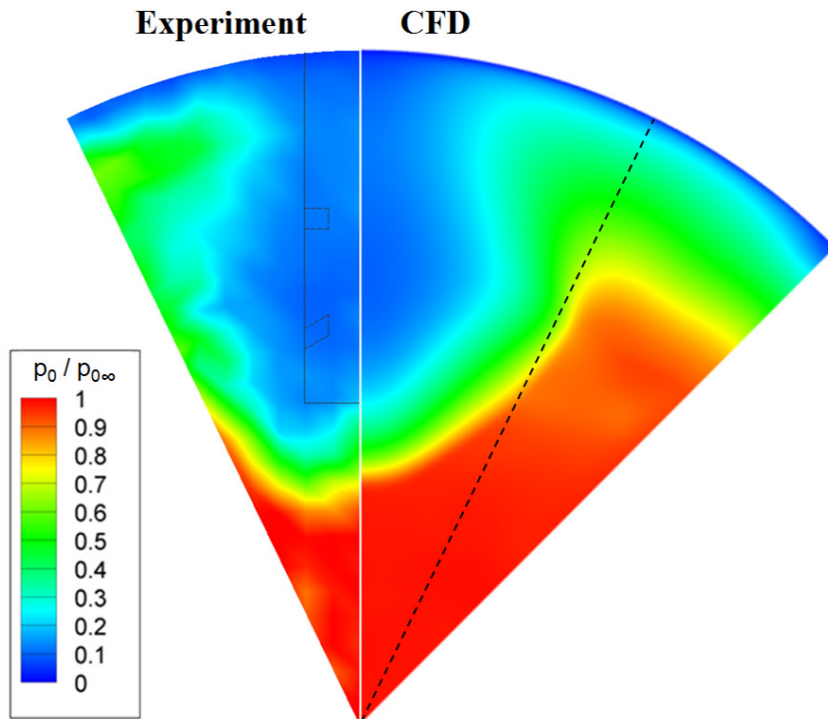


Figure 4.14: Experiment vs. CFD Mach total pressure contour comparison for the strut injector, $M_\infty = 4$, He injection ($\bar{q} = 3.13$) case

4.5 Conclusions

A strut injector model for circular scramjet combustors was experimentally studied under cold-flow (non-combusting) conditions to determine its fuel-air mixing behavior. The experiments investigated the effects of injectant molecular weight and freestream Mach number on the fuel-air mixing process. Helium, methane, and air injectants were studied to vary the injectant molecular weight and the experiments were run at nominal freestream Mach numbers of 2 and 4. The primary goal of the study was to provide validation data to support the development of turbulence model upgrades. Secondary goals were to assess the penetration and mixing of the simulated fuel jets and to quantify the uncertainties of the CFD predictions for the injector design.

The main reason for considering an intrusive injector design for application in such a challenging thermal environment as a scramjet combustor is the goal of minimizing the combustor length in the low aspect ratio combustors currently being considered for such applications. An in-stream injector inherently yields better penetration and airstream coverage in short axial distances than a flush-wall injector. If adequate mixing can also be achieved in a short distance, then the drag and thermal load penalties of the in-stream injector can be overcome.

The experimental results for the strut injector obtained at 1.81 duct diameters downstream showed good distribution of the injectant into the combustor cross-section, but the individual jets had merged into a single large plume and the rate of mixing was somewhat slow. In addition, a substantial total pressure loss occurred in the flow downstream of the strut. There were substantial regions of fuel-rich (using either the stoichiometric ratio of a hydrogen-air mixture or a methane-air mixture as a metric) concentrations in the plumes, even though the overall mixture in the duct was lean, on the same basis. One might have expected better mixing based on simple, isolated injector correlations (refer to Section 1.4.8).

The primary conclusions found from the strut injector study regarding the effects of injectant molecular weight and freestream Mach number on the fuel-air mixing process were:

- An increase in injectant molecular weight resulted in further projection of the plume into the combustor cross-section according to the species concentration measurements.

However, no noticeable differences in the plume position for different molecular weight injectants were evident in the Mach number or total pressure measurements.

- An increase in injectant molecular weight resulted in a slower mixing rate according to the species concentration measurements.
- For helium injection, reducing the Mach number from 4 to 2 while maintaining a constant injectant mass flow rate resulted in an increase in both the rate of mixing of the injectant and further projection of the plume into the combustor cross-section. The increase in mixing rate can be attributed to an increase in the quantity $|u_j / u_\infty - 1|$, whereas the further projection of the plume can be attributed to an increase in \bar{q} .
- As the injectant molecular weight increases, the Mach number in the region of the injectant plume increases. This effect was also present in the wall injector study, but to a much lesser extent. One factor that may contribute to this effect is the decrease in the injectant volumetric flow rate that occurs as the injectant molecular weight increases.
- As the injectant molecular weight increases, the total pressure loss in the region of the injectant plume decreases due to the increase in Mach number.

CFD with a RANS formulation was used to provide detailed simulations of penetration and mixing. The CFD model was able to provide excellent predictions overall. Mixing was predicted very well and penetration was predicted reasonably well. This level of agreement required an upgraded turbulence model, which was developed using this experimental work and also the work of other independent researchers.

Chapter 5: Discussion

5.1 Summary of Conclusions

A flush-wall injector model and a strut injector model for circular scramjet combustors were experimentally studied under cold-flow (non-combusting) conditions to determine their fuel-air mixing behavior. The flush-wall injector model consists of sixteen inclined, round, sonic injectors distributed around the wall of a circular duct. The strut injector model has sixteen inclined, round, sonic injectors distributed across four struts within a circular duct. The struts are slender, inclined at a low angle to minimize drag, and have two injectors on each side. The experiments investigated the effects of injectant molecular weight, freestream Mach number, and jet-to-freestream momentum flux ratio (\bar{q}) on the fuel-air mixing process. Helium, methane, and air injectants were studied to vary the injectant molecular weight. The effects of freestream Mach number on the mixing process were also investigated by running experiments at nominal freestream Mach numbers of 2 and 4, which simulates combustor conditions for nominal flight Mach numbers of 5 and 10. Additionally, experiments were also performed that independently varied the value of \bar{q} . All of these experiments were performed to support the needs of an integrated experimental and computational research program, which has the goal of upgrading the turbulence models that are used for CFD predictions of the flow inside a scramjet combustor. The main goal of the experiments was to provide validation data to support the development of turbulence model upgrades. Other goals of the experiments were to assess the penetration and mixing of the simulated fuel jets in comparison with the expectations upon which the arrangements were designed and also to quantify the uncertainties of the CFD predictions for such injector designs. Lastly, the experiments sought to add to the sparse database of high-speed mixing results applicable to scramjet combustors.

To assess the mixing behavior of the two different injector models, measurements of species concentration, Mach number, and total pressure were taken in the far field. The data measurement plane for the flush-wall injector model was 83.6 injector diameters or 1.72 duct diameters downstream of the injectors, whereas the measurement plane for the strut injector model was 119 injector diameters or 1.81 duct diameters downstream. Species concentration was measured using an aspirating type concentration probe, which was attached to a vacuum

pump. The method for measuring Mach number and total pressure was dependent on the flow conditions. Outside of the injectant plume, a conical five-hole pressure probe was used to determine these values. Inside of the injectant plume, the Mach number and total pressure values were determined using a multiple probe survey method that utilized data from the concentration probe, five-hole probe, and a cone-static probe.

The experimental results for the flush-wall injector obtained at 1.72 duct diameters downstream showed reasonable mixing based on simple, isolated injector correlations. In this configuration, the penetration of the injectant across the combustor cross-section was modest, which left a substantial region of pure air along the duct centerline. The total pressure losses for this configuration were also modest.

The experimental results for the strut injector obtained at 1.81 duct diameters downstream showed good distribution of the injectant into the combustor cross-section. However, the individual jets had merged into a single large plume and the rate of mixing was somewhat slow based on simple, isolated injector correlations. A substantial total pressure loss occurred in the flow downstream of the strut.

Injectants with molecular weights ranging from 4-29 were utilized in this study. The jet-to-freestream momentum flux ratio (\bar{q}) was matched for the different injectants for cross comparison purposes. An increase in injectant molecular weight at the same \bar{q} resulted in the following effects on the fuel-air mixing process in the far field:

- Penetration that was approximately the same as lower molecular weight injectants
- A mixing rate that was the same as or slower than lower molecular weight injectants depending on the flow conditions
- Higher Mach numbers in the region of the jet plume than lower molecular weight injectants
- Less overall total pressure losses than lower molecular weight injectants
- Less lateral spreading of the jet plume in terms of the Mach number and total pressure properties than lower molecular weight injectants

In the case of the flush-wall injector model, molecular weight effects did not significantly influence the amount of penetration or mixing rate of the injectant. In the case of the strut injector model, the relative amount of penetration for the different injectants could not be evaluated based upon the concentration measurements that were performed. However, in the strut injector configuration, methane (molecular weight = 16) mixed significantly slower than the helium (molecular weight = 4). Additionally, the methane plume was projected about 32% further into the combustor cross-section than the helium plume according to the species concentration measurements for the strut injector. This suggests that the response of an injectant to a mixing enhancement technique can potentially differ significantly depending on its molecular weight.

Several other researchers have also investigated the effects of injectant molecular weight on a jet in supersonic crossflow, but these studies have mostly been performed in the near field. In a shock-tunnel experiment, Ben-Yakar et al.²⁹ investigated the penetration of ethylene (molecular weight = 28) and hydrogen (molecular weight = 2) jets in the near field region less than 10 injector diameters downstream. They found that the ethylene jet penetrated deeper into the supersonic freestream than hydrogen for the same jet-to-freestream momentum flux ratio (\bar{q}). The increased penetration of the ethylene jet was attributed to significant differences in the development of the jet shear layer for the two different gases. Burger⁵⁴ investigated the effects of injectant molecular weight on the near field jet penetration of a single flush-wall injector in supersonic crossflow for injectants with molecular weights ranging from 4-44 operated at the same \bar{q} . Measurements from this study performed at 13 injector diameters downstream typically indicated a weak increase in penetration with increasing molecular weight. Lastly, Portz and Segal³¹ studied the penetration of helium (molecular weight = 4) and argon (molecular weight = 40) jets in supersonic crossflow using Schlieren images taken from 3-30 injector diameters downstream. At 30 injector diameters downstream, they found that the penetration of the argon jets was equal to or slightly greater than that of the helium jets at the same \bar{q} . Considering the effects of injectant molecular weight observed in the current far field mixing study and also the effects observed in near field studies by other researchers leads to the following conclusion: injectants with higher molecular weights can slightly increase the near field penetration of a jet, but this effect is not noticeable in the far field.

The effects of freestream Mach number and jet-to-freestream momentum flux ratio (\bar{q}) on the fuel-air mixing process were also investigated as part of this study. The following conclusions were found regarding these effects:

- For helium injection from 30° inclined, sonic, circular injectors, reducing the freestream Mach number from 4 to 2 while maintaining a constant injectant mass flow rate resulted in an increase in both the penetration and the rate of mixing of the injectant. The increase in penetration can be attributed to an increase in \bar{q} , whereas the increase in mixing rate can be attributed to an increase in the quantity $|u_j / u_\infty - 1|$.
- For helium injection from 30° inclined, sonic, circular injectors into a Mach 4 freestream, an increase in the value of \bar{q} from 1.71 to 2.28 resulted in an increase in penetration, plume area, plume width, and a faster rate of mixing.

Both of these results are also applicable to hydrogen-fueled scramjet combustors as the work of Torrence³⁷ demonstrated that the penetration and mixing of helium and hydrogen are nearly the same in cold flow mixing studies with equivalent dynamics pressure ratios.

The experimental studies of the flush-wall injector model and the strut injector model presented here contributed to the sparse database of high-speed mixing experiments in two main areas. First, these experiments investigated the effects of confinement within a circular duct on the fuel-air mixing process, which is an important issue that very few of the previous studies in the literature investigated. Second, these experiments investigated injectant molecular weight effects on the fuel-air mixing process, which is another sparsely investigated area. Most of the previous high-speed mixing studies available focused on low molecular weight injectants such as hydrogen and helium, whereas these experiments also utilized heavier molecular weight injectants (methane and air). Additionally, previous studies of injectant molecular weight effects were primarily performed in the near field region, whereas these studies were performed in the far field. Lastly, in addition to the contributions made in these two main areas, these experiments also investigated the effects of freestream Mach number and jet-to-freestream momentum flux ratio (\bar{q}) on the fuel-air mixing process.

CFD with a RANS formulation was able to provide good predictions of mixing and reasonable predictions of penetration. This level of agreement required an upgraded turbulence model, which was developed using this experimental work and also the work of other independent researchers. In both the case of the flush-wall injector and the case of the strut injector, the CFD model had sufficient accuracy such that it could be a valuable tool to a scramjet engine designer. Thus, the goal of using these experiments to quantify the uncertainty of CFD predictions for typical scramjet engine injector configurations was realized. Furthermore, even though this was a cold-flow study, higher confidence in the CFD predictions for hot-flow, combusting conditions can now be expected due to the improvements that were made under cold-flow conditions. Ultimately, the primary goal of upgrading the turbulence modeling using this combined experimental and numerical study was achieved, which clearly demonstrates the value of an integrated experimental and numerical approach.

5.2 Comparison of the Flush-Wall and Strut Injector Configurations

The primary goals of this study were to use injector models that represent state of the art scramjet engine combustion chambers to provide validation data to support the development of turbulence model upgrades and to add to the sparse database for mixing results in such configurations. Comparing a flush-wall injector configuration to a strut injector configuration was not a highly prioritized goal. Instead, we sought to develop and test a well-designed flush-wall injector model and a well-designed strut injector model. A well-designed flush-wall injector does not have exactly the same characteristics as a well-designed strut injector, which resulted in some inherent differences between the two models. Nevertheless, the experiments were run in such a way as to allow direct comparisons to be made between the results for the two different injector models.

When comparing the two injector models and the experimental conditions under which they were tested, the following similarities are evident:

- Both injector models are confined within a 100 mm diameter circular duct
- Both injector models have a total of 16 inclined, sonic, circular injectors

- For four experimental cases for each injector model, the following items were matched for cross comparison purposes between the two models:
 - Injectant gas (helium, methane, or air)
 - Freestream Mach number
 - Total injectant mass flow rate

Matching the three items listed above also resulted in matched fuel-air ratios and velocity ratios for corresponding cases.

The primary differences between the two models and experimental conditions include the following:

- Injector diameter: 2.06 mm for the flush-wall injector model vs. 1.52 mm for the strut injector model
- Data measurement plane location: 1.72 duct diameters downstream for the flush-wall injector vs. 1.81 duct diameters downstream for the strut injector

Table 5.1 compares the experimental conditions and mixing results for the flush-wall injector model to the strut injector model. In this table, a new performance parameter is utilized. The parameter h_{pl} is used to describe the penetration of the plume relative to the injector location and is defined as follows:

- For the flush-wall injector model, h_{pl} is the over-stoichiometric plume height measured perpendicular to the duct wall
- For the strut injector model, h_{pl} is the maximum distance from the strut side wall to the stoichiometric concentration contour (measured perpendicular to the strut side wall)

For the calculations of h_{pl} and A_{pl} in Table 5.1, the stoichiometric value for a hydrogen-air mixture was used as a metric.

Injector Model	Experimental Case							
	Wall	Strut	Wall	Strut	Wall	Strut	Wall	Strut
Injectant	Helium	Helium	Methane	Methane	Air	Air	Helium	Helium
M_∞	3.9	3.9	3.9	3.9	3.9	3.9	2.0	2.0
\bar{q}	1.71	3.13	1.71	3.13	1.71	3.13	2.24	4.10
$\dot{m}_{j,total}$ [g/s]	22.5	22.5	47.3	47.3	62.7	62.7	22.5	22.5
f	0.0098	0.0098	0.0206	0.0206	0.0273	0.0273	0.0106	0.0106
u_j / u_∞	1.31	1.31	0.62	0.62	0.47	0.47	1.71	1.71
ρ_j / ρ_∞	0.99	1.82	4.38	8.02	7.69	14.09	0.77	1.41
$p_{0j} / p_{0\infty}$	0.35	0.63	0.39	0.72	0.38	0.70	1.97	3.62
α_{max}	0.073	0.106	0.142	0.299	-	-	0.032	0.045
$y_{a,max}$ [mm]	5.0	16.0	8.0	16.0	-	-	5.0	18.0
y_{CM} [mm]	5.1	16.7	5.2	22.1	-	-	7.4	20.8
h_{pl} [mm]	10.2	8.7	-	-	-	-	-	-
A_{pl}^* [mm ²]	2016	1636	-	-	-	-	-	-

Table 5.1: Experimental conditions and mixing results for the flush-wall injector vs. the strut injector

* Sum of the plume areas for the entire injector model including all 16 injectors

Figure 5.1 shows a comparison of the experimental mass fraction contours for the flush-wall injector vs. the strut injector for the corresponding helium injection, $M_\infty = 4$, $f = 0.0098$ cases. The mixing results along the plume centerline for all comparable cases for the two injector models are shown in Figure 5.2. From the results presented in Table 5.1 and Figures 5.1 – 5.2, it is clear that the flush-wall injector mixed significantly faster than the strut injector in all of the experimental cases. The injectant mass fractions measured for the flush-wall injector were significantly lower than those measured for the strut injector, even though the data measurement plane for the flush-wall injector was slightly further upstream. In terms of the penetration relative to the injectors, which is described by the parameter h_{pl} , the flush-wall injector showed greater penetration. The flush-wall injector also provided better airstream coverage as its plume

area covered 26% of the duct cross-section, whereas the plume area for the strut injector covered 21% of the duct cross section. On the other hand, the strut injector produced injectant plumes that were located further away from the duct wall, which is a desirable condition as this should reduce wall heating during combustion.

One possible explanation for the slower mixing of the strut injector model is that the injectors on the sides of each strut were positioned too close together. The injectors for the strut injector model were spaced 5.8 injector diameters apart, whereas the injectors for the flush-wall injector model were spaced 9.5 injector diameters apart. The critical value for transverse injector spacing to prevent mixing from being inhibited is about 9 injector diameters²⁴. However, achieving this amount of injector spacing is certainly a design challenge in a strut injector configuration, where the size of the struts must be minimized to reduce drag and limit total pressure losses. The positioning of the injectors in a strut configuration is further limited by the thickness of the duct wall boundary layer. Theoretical indications are that better mixing is achieved if the injectors are positioned outside of the duct wall boundary layer, so that the boundary layer incoming to the injectors is thin. All of these considerations are important factors when developing a strut injector design for a scramjet combustor.

A comparison of the Mach number and total pressure results along the plume centerline for all experimental cases for the two injector models is shown in Figure 5.3. For the strut injector, the Mach number downstream of the strut is substantially reduced and it is also moderately reduced at the duct centerline. The strut injector also has substantially greater total pressure losses than the flush-wall injector. Both of these effects are expected due to the protrusion of the struts into the duct.

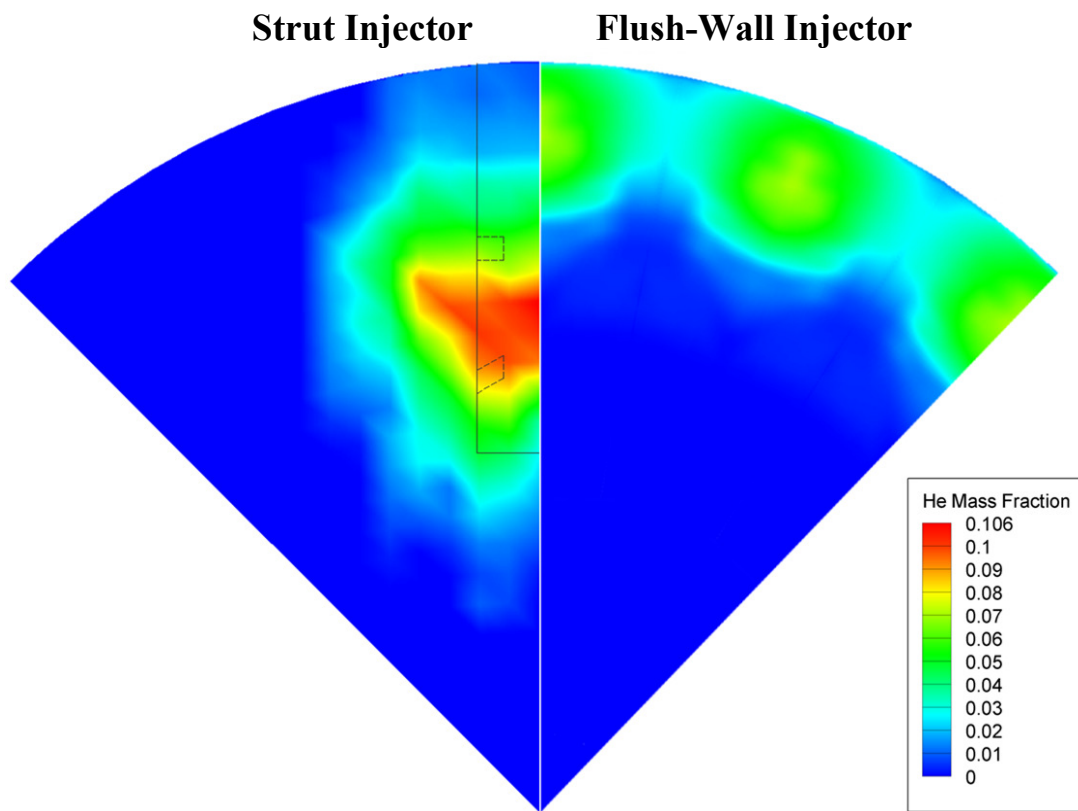


Figure 5.1: Comparison of the experimental mass fraction contours for the flush-wall injector vs. the strut injector (for He injection, $M_\infty = 4$, $f = 0.0098$)

$Y / D = 0.5$ represents the duct wall location and $Y / D = 0$ represents the duct centerline

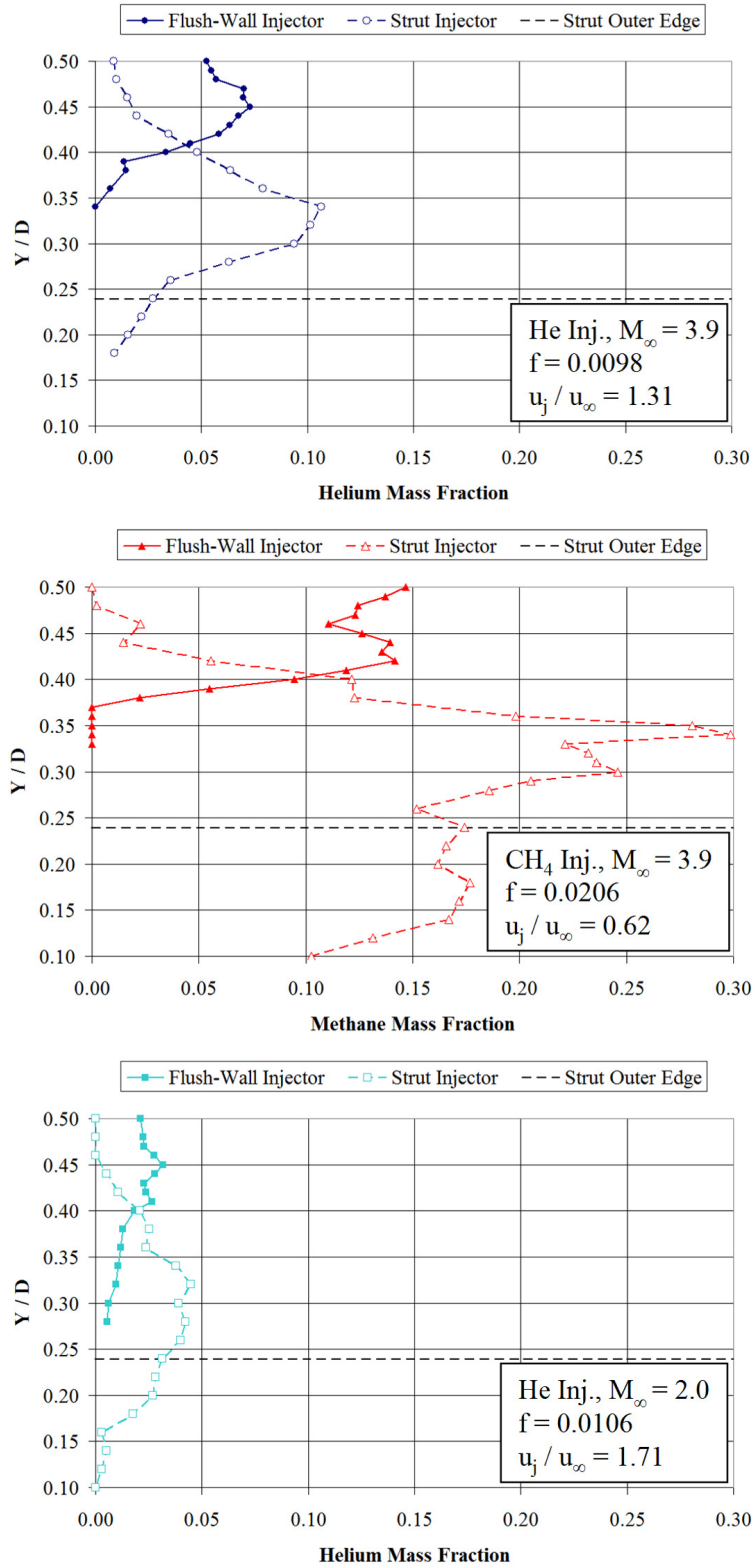


Figure 5.2: Comparison of the experimental mixing results along the plume centerline for the flush-wall injector vs. the strut injector

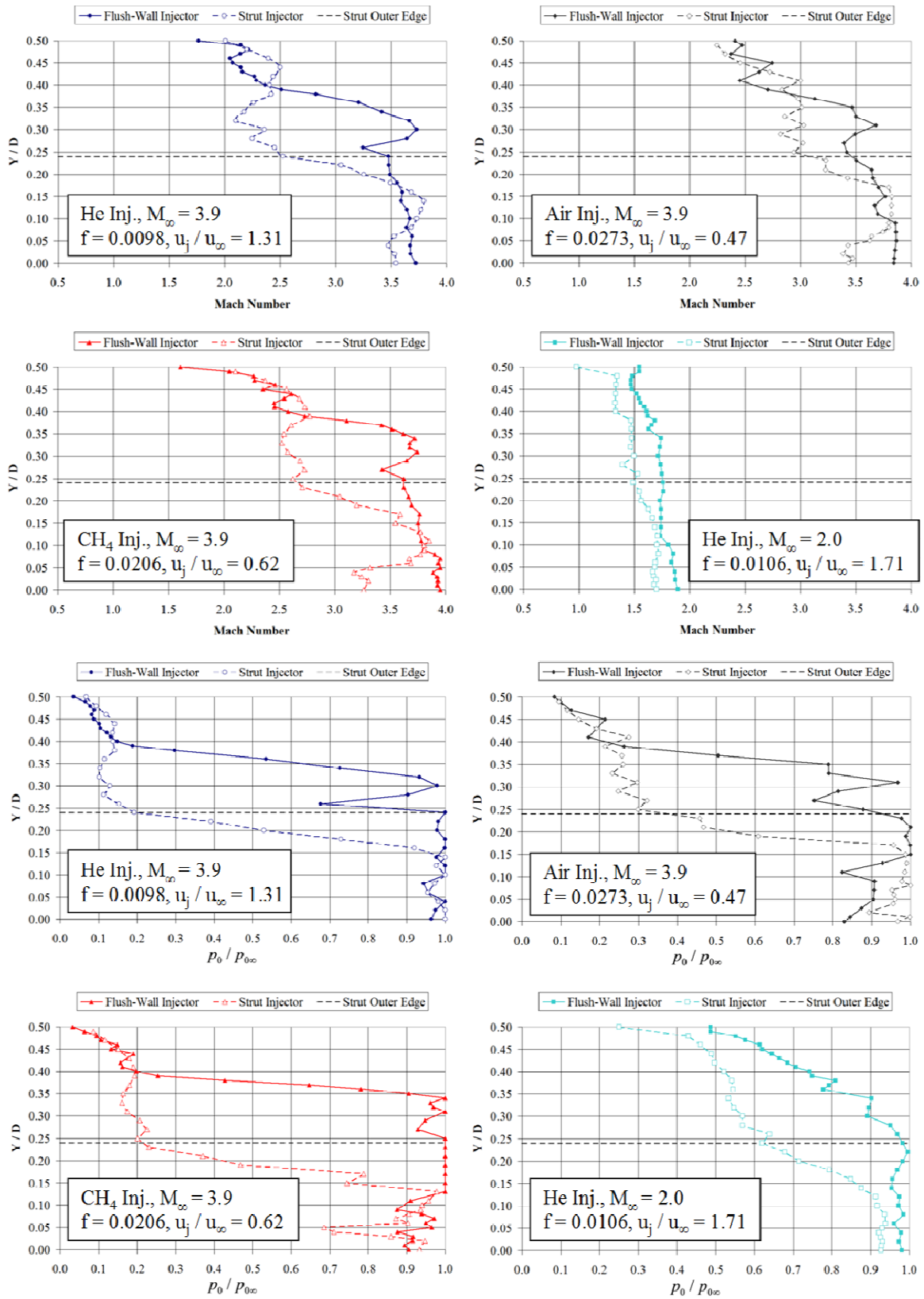


Figure 5.3: Comparison of the experimental Mach number and total pressure results along the plume centerline for the flush-wall injector vs. the strut injector

5.3 Recommendations for Future Work

As a continuation of the work completed for this dissertation, several recommendations for future work are made. These items include continued experimental research, facility upgrades, and instrumentation improvements.

5.3.1 Cold-Flow Optical Concentration Measurements

The species concentration measurements performed for this study were intrusive (i.e. probe) type measurements. Non-intrusive (i.e. optical) measurements are often preferred over intrusive measurements as the non-intrusive methods minimize the influence on the flow being measured. Optical measurements are also generally more efficient than probe type measurements. Probes measure single data points, whereas certain optical methods can obtain an entire plane of data at once. However, optical measurements are generally much more costly than probe type measurements. The concentration measurements performed for this study obtained data at a single axial plane for each injector model, which provided sufficient data to achieve the goals of the research program at limited cost. If a large number of measurements at multiple axial planes were desired to more fully characterize the flow, optical methods could be a cost effective option. One example of an optical method that can be used to measure species concentration is Raman Scattering. For instance, Lin et al.¹² used Raman Scattering to study ethylene injection into a Mach 2 crossflow. If Raman Scattering were used to study methane injection from the flush-wall and strut injector models utilized in the current study to more fully characterize the flowfield, valuable high-speed mixing data would be obtained. This data could be used to improve the understanding of the fuel-air mixing process in circular scramjet combustors, expand the sparse database of high-speed mixing experiments, and help further improve CFD models.

5.3.2 Combustion Experiments

The next logical step in the progression of this research is to perform combustion experiments. For this study, a large amount of fuel-air mixing data for circular scramjet combustors was gathered under cold-flow conditions, which was used to substantially improve the CFD predictions under such conditions. Now that the CFD predictions for cold-flow conditions have

been very much improved, the foundation has been created to improve the predictions for hot-flow, combusting conditions. The combustion experiments that represent a continuation of the current study should be performed using a high-speed wind tunnel with an axisymmetric nozzle as circular cross-section combustors are currently of interest. The experiments would improve the knowledge of the combustion behavior of circular scramjet combustors and provide validation data for potential improvements to CFD models. Experiments under the hot-flow conditions of interest are extremely challenging, but necessary to support continued scramjet development. These experiments would likely need to rely heavily on optical measurement techniques due to the extremely high temperature of the flow. Alternatively, a combination of optical and in-stream measurements could be used. Several useful optical measurement techniques for supersonic combustion experiments include PLIF^{55,56,57} (planar laser-induced fluorescence), TDLAS^{57,58} (tunable diode laser-based absorption spectroscopy), and Rayleigh Scattering⁵⁵. If in-stream measurements are to be performed, some method for cooling the probing would probably be necessary. For instance, Smith et al.⁵⁹ used water-cooled Pitot probe rakes to perform measurements at the exit of an axisymmetric supersonic combustor.

5.3.3 Test Facility Improvements

The potential exists at Virginia Tech to build a new facility with the same basic design and dimensions as the existing hypersonic wind tunnel facility, which would have a run time of approximately one minute. The time required to charge the new facility in between runs would be about 15 minutes, whereas the existing hypersonic wind tunnel requires about one hour to charge between runs. This new facility could dramatically reduce the amount of time required to perform experiments that currently require a large number of 2-3 second runs. For example, about 400 runs of 3.2 seconds each were required to complete the current study. Therefore, about 400 man hours were required to achieve 21 minutes of actual tunnel run time. If this new facility were built, 21 minutes of tunnel run time could be achieved in only 5.25 man hours. Thus, this new facility could enable a dramatic improvement in experimental efficiency.

The new long duration run facility would be connected to the existing compressor and air supply for the supersonic wind tunnel, which has a much higher flow and storage capacity than that of the existing hypersonic tunnel. Thus, the use of this compressor and air supply would enable

much longer run times. Spare parts from the existing hypersonic tunnel facility including a spare plenum chamber, set of nozzles, and test section could be utilized as the primary components of the new facility. The existing hypersonic tunnel facility would be maintained in its current state for operation from Mach 2 to 7 with run times of 2-3 seconds and flow heating capability. The new long duration run facility would be capable of operating from Mach 2 to 4 with run times of about one minute, but without flow heating capability.

The primary design challenge related to the development of the new long duration run facility is the design of a system to control the tunnel plenum pressure. The following options have been considered for the plenum pressure control system:

- The use of a high flow capacity dome regulator
- The use of the combination of a gate valve and a dome regulator (or an electronic pressure regulator)
- The use of a pressure regulating valve with PID control such as the valve that is currently used to operate the supersonic wind tunnel

The use of a single high flow capacity dome regulator is probably the simplest and least expensive option for controlling the tunnel plenum pressure. Control within +/- 5% of the desired plenum pressure could be achieved with this option. Only one commercial manufacturer was found that currently builds dome regulators with high enough flow capacity for this application. If a single dome regulator with high enough flow capacity could not be procured, the flow could be divided between the combination of a gate valve and a dome regulator with lower flow capacity. The gate valve would be opened to a fixed setting allowing a portion of the airflow to pass through it. The dome regulator would then be used to control the remaining portion of the airflow to achieve the desired plenum pressure. Again, control of the plenum pressure within about +/- 5% could be achieved with this option for limited cost. Finally, a pressure regulating valve with PID control could also be used to control the tunnel plenum pressure. This option is probably the most complex and expensive, but also gives the best performance. With this design, the tunnel plenum pressure could potentially be controlled within +/- 1% of the desired value.

5.3.4 Concentration Probe Improvements

As demonstrated by the current study, a concentration probe can be a valuable resource for high-speed mixing research. This is especially true if the probe is small in size, fast response, robust, and inexpensive. To improve upon the existing concentration probe design, a concept for a new concentration probe was developed with the primary goals of achieving both a reduction in size and a faster response time. Figure 5.4 shows a diagram of the proposed new concentration probe design. Just like the existing probe, the new probe is an aspirating type design that is based upon the fundamental concept developed by Ninnemann and Ng⁴³. The primary differences between the new probe design and the existing probe design are:

- The new design uses a miniature hot-film sensor that is positioned perpendicular to the freestream flow, whereas previously the hot-film sensor was positioned at a 20° angle to the freestream flow.
- The new design uses a miniature piezoresistive pressure transducer that is built directly into the housing of the probe, whereas previously the pressure transducer was located externally and connected via tubing

The repositioning of the hot-film sensor greatly reduces the overall size of the probe and allows the probe to be better streamlined. Additionally, this change has a minimal impact on the operation of the probe, because the time required for a flow sample to travel from the probe tip to the hot-film sensor is only about 5 ms. The use of the integrated piezoresistive pressure transducer substantially improves the response time of the probe.

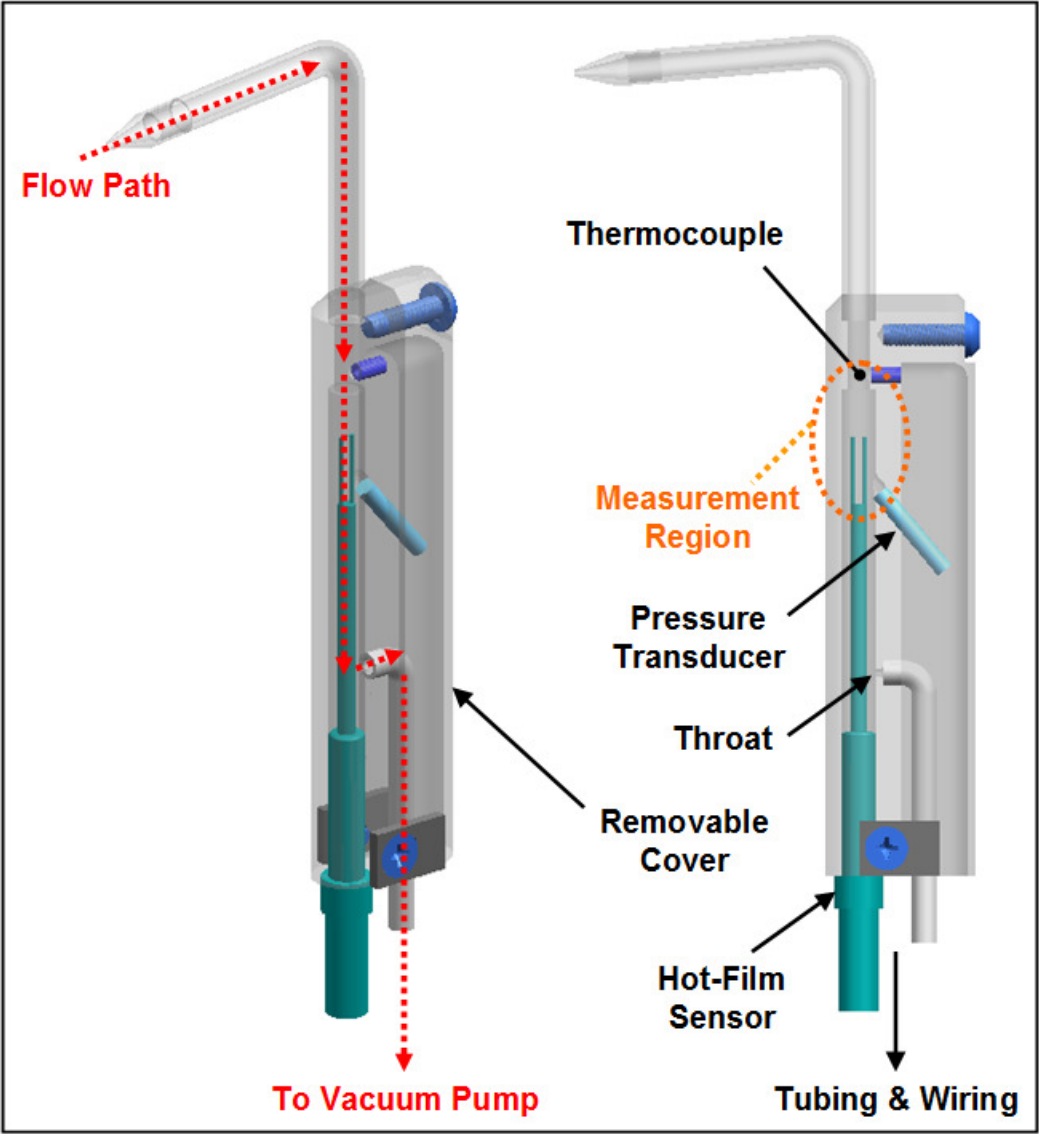


Figure 5.4: Proposed new concentration probe design

A size comparison of the proposed new concentration probe vs. the existing concentration probe is shown in Figure 5.5. In the region of the probe that is exposed to the flow, its size has been greatly reduced. For the new design, it is estimated that the pause time required to obtain a mean concentration data point will be reduced from 200 ms to about 50 ms. Likewise, the maximum frequency response of the probe will be improved from 20 Hz to about 50 Hz. The limiting factor in the response time of the probe now becomes the thermocouple, which requires 20 ms to sufficiently respond to a step input. If this new concentration probe design were used with the existing traverse system that is already in place, the number of data points that could be measured during each run would be increased by about 50%. The use of a different form of temperature measurement has also been considered to further improve the response of the probe. However, this results in increased size and complexity and still results in about the same 50% increase in measurement efficiency, because the speed of the current traverse system then becomes the limiting factor. It is also noteworthy that the use of this probe would decrease the injectant gas cost for species concentration measurements by about 33% due to the reduced amount of time required to measure each data point. Thus, even if the long duration run test facility discussed in Section 5.3.3 were built, it could still be worthwhile to build this new probe as well. For additional details about the design and analysis of the proposed new concentration probe, refer to Appendix D.

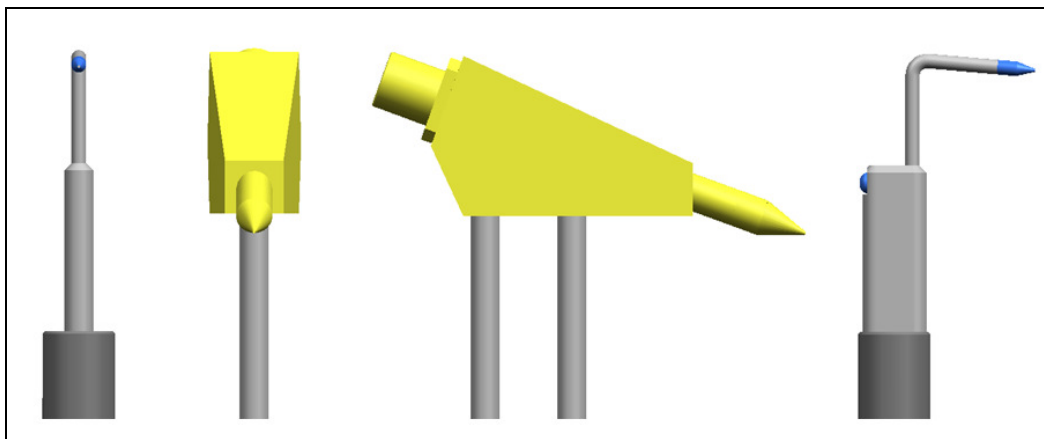


Figure 5.5: Size comparison of the proposed new concentration probe vs. the existing concentration probe

Appendix A: Taylor-Maccoll Solution for a 10 Degree Sharp Cone with Variable Specific Heat Ratio

A method is described here to determine the Mach number of a supersonic flow using a combination of two pressure measurements, Pitot pressure (p_{02}) and cone-static pressure (p_{cone}). This method is valid both inside and outside of the boundary layer as long as the flow is supersonic and attached to the cone. Furthermore, this method can be used for the measurement of gas mixtures. The theoretical foundation for the method is based upon a combination of the Taylor-Maccoll solution for a sharp cone and normal shock relations. The current study involved measurements of gas mixtures under a range of different Mach number conditions. In the theory used to derive the solution for this method, the only variable that is influenced by the gas composition is the ratio of specific heats (γ). Therefore, the solution for this method was derived for the range of different Mach numbers and values of γ encountered in the experiments. Additionally, the solution was derived for a 10° half-angle cone, which was the angle of the cone-static probe that was used to perform these measurements. Figure A.1 shows generalized diagrams of a Pitot probe and a cone-static probe in supersonic flow.

The first step in the solution procedure is to use the Taylor-Maccoll solution to solve for the ratio of the static pressure on the surface of the cone (p_{cone}) to the local static pressure ahead of the oblique shock (p_1):

$$\frac{p_{cone}}{p_1} = f(M_1, \gamma, \theta_{cone}) \quad (\text{A.1})$$

The numerical method used for the Taylor-Maccoll solution is described in Anderson⁶⁰. Next, the ratio of p_{01} / p_1 is determined using the isentropic relation:

$$\frac{p_{01}}{p_1} = \left(1 + \frac{\gamma - 1}{2} M_1^2\right)^{\frac{\gamma}{\gamma - 1}} \quad (\text{A.2})$$

The ratio of p_{02} / p_{01} is then found using equation 2.28, which is a normal shock relation. The final step in the solution procedure is to determine the ratio of p_{cone} / p_{02} :

$$\frac{p_{cone}}{p_{02}} = \frac{p_{cone}}{p_1} \frac{p_1}{p_{01}} \frac{p_{01}}{p_{02}} = f(M_1, \gamma, \theta_{cone}) \quad (\text{A.3})$$

Thus, if θ_{cone} , γ , and the ratio of p_{cone} / p_{02} are known, M_1 can be determined. The solution for equation A.3 is tabulated in Table A.1 for $\theta_{cone} = 10^\circ$ over a range of values for M_1 and γ . This solution was verified for the $\gamma = 1.4$ case using tables and charts from NACA 1135⁶¹. It should be emphasized that this solution requires the use of two separate probes, a Pitot probe and a cone-static probe, and knowledge of the mixture composition, which can be obtained from a concentration probe.

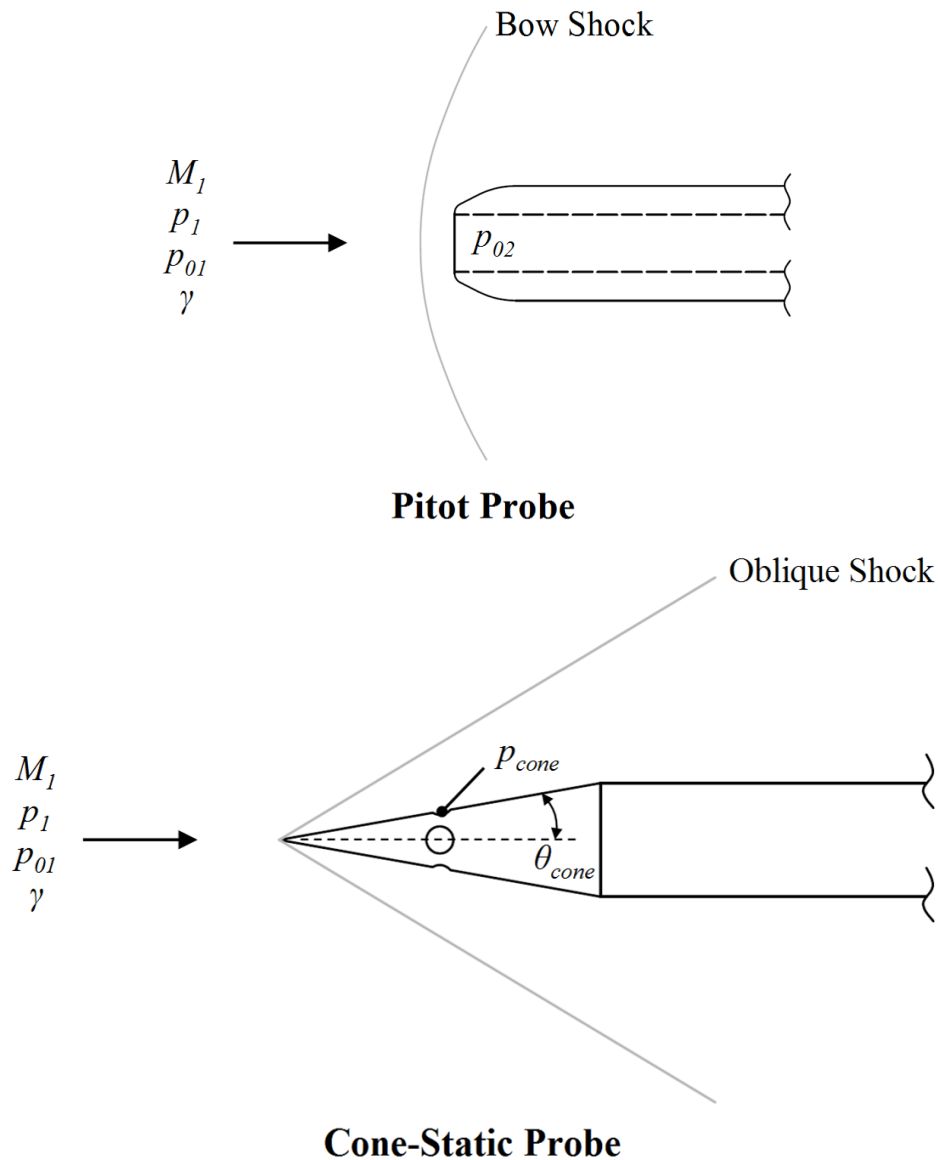


Figure A.1: Diagrams of a Pitot probe and a cone-static probe in supersonic flow

p_{cone} / p_{02} values as a function of M_1 and γ :

		Ratio of specific heats (γ)									
		1.34	1.36	1.38	1.4	1.42	1.44	1.46	1.48	1.50	1.52
M_1	1.06	0.5819	0.5793	0.5768	0.5743	0.5719	0.5696	0.5673	0.5650	0.5629	0.5608
	1.1	0.5484	0.5455	0.5427	0.5401	0.5373	0.5347	0.5321	0.5296	0.5270	0.5246
	1.2	0.4874	0.4846	0.4818	0.4789	0.4765	0.4739	0.4713	0.4688	0.4663	0.4639
	1.3	0.4370	0.4344	0.4318	0.4293	0.4266	0.4242	0.4218	0.4194	0.4171	0.4148
	1.4	0.3939	0.3914	0.3890	0.3867	0.3843	0.3820	0.3797	0.3775	0.3753	0.3732
	1.5	0.3568	0.3545	0.3523	0.3501	0.3480	0.3459	0.3437	0.3417	0.3397	0.3378
	1.6	0.3248	0.3227	0.3207	0.3185	0.3167	0.3148	0.3128	0.3109	0.3091	0.3073
	1.7	0.2971	0.2952	0.2933	0.2914	0.2896	0.2878	0.2861	0.2844	0.2827	0.2811
	1.8	0.2731	0.2713	0.2695	0.2679	0.2661	0.2645	0.2629	0.2614	0.2598	0.2584
	1.9	0.2520	0.2504	0.2488	0.2472	0.2457	0.2442	0.2427	0.2413	0.2399	0.2385
	2	0.2335	0.2321	0.2306	0.2291	0.2277	0.2264	0.2250	0.2237	0.2225	0.2212
	2.1	0.2173	0.2159	0.2146	0.2133	0.2119	0.2107	0.2094	0.2082	0.2071	0.2059
	2.2	0.2029	0.2016	0.2004	0.1992	0.1980	0.1969	0.1957	0.1946	0.1936	0.1925
	2.3	0.1901	0.1890	0.1878	0.1867	0.1856	0.1845	0.1835	0.1825	0.1815	0.1805
	2.4	0.1787	0.1777	0.1766	0.1755	0.1745	0.1736	0.1726	0.1717	0.1708	0.1699
	2.5	0.1685	0.1675	0.1665	0.1656	0.1646	0.1637	0.1629	0.1621	0.1612	0.1604
	2.6	0.1593	0.1584	0.1575	0.1566	0.1558	0.1550	0.1542	0.1534	0.1526	0.1519
	2.7	0.1511	0.1502	0.1494	0.1485	0.1478	0.1470	0.1463	0.1456	0.1449	0.1442
	2.8	0.1436	0.1428	0.1420	0.1413	0.1405	0.1398	0.1391	0.1384	0.1378	0.1372
	2.9	0.1367	0.1361	0.1354	0.1347	0.1339	0.1333	0.1327	0.1320	0.1314	0.1308
	3	0.1306	0.1299	0.1293	0.1286	0.1280	0.1274	0.1268	0.1262	0.1256	0.1251
	3.1	0.1249	0.1243	0.1237	0.1231	0.1225	0.1219	0.1214	0.1209	0.1204	0.1199
	3.2	0.1198	0.1192	0.1186	0.1180	0.1175	0.1170	0.1165	0.1160	0.1156	0.1151
	3.3	0.1150	0.1145	0.1140	0.1134	0.1129	0.1125	0.1120	0.1115	0.1111	0.1106
3.4	0.1107	0.1102	0.1097	0.1092	0.1087	0.1083	0.1078	0.1074	0.1070	0.1066	
3.5	0.1067	0.1062	0.1058	0.1053	0.1048	0.1044	0.1040	0.1036	0.1032	0.1029	
3.6	0.1030	0.1025	0.1021	0.1017	0.1013	0.1009	0.1005	0.1002	0.0998	0.0995	
3.7	0.0995	0.0991	0.0987	0.0983	0.0980	0.0976	0.0973	0.0969	0.0966	0.0963	
3.8	0.0963	0.0959	0.0956	0.0952	0.0949	0.0945	0.0942	0.0939	0.0936	0.0933	
3.9	0.0934	0.0930	0.0927	0.0924	0.0920	0.0917	0.0914	0.0911	0.0908	0.0906	
4	0.0906	0.0903	0.0900	0.0897	0.0894	0.0891	0.0888	0.0885	0.0883	0.0880	
4.1	0.0880	0.0878	0.0875	0.0872	0.0869	0.0866	0.0864	0.0861	0.0859	0.0856	
4.2	0.0857	0.0854	0.0851	0.0849	0.0846	0.0843	0.0841	0.0838	0.0836	0.0834	

Table A.1: Taylor-Maccoll solution for a 10 degree sharp cone with variable specific heat ratio

Appendix B: Discussion of the Differences between the Straight Tip and Angled Tip Concentration Probes

Two slightly different configurations of the same basic concentration probe design were used for the experiments. Figure 2.21 shows pictures of the two different concentration probe configurations and Table B.1 summarizes the differences between the two probes. Both probes have the same nominal electrical properties and critical dimensions. Furthermore, the measurement uncertainty of the two probes was found to be nearly identical (refer to Appendix C). The primary difference between the two configurations is the angle of the probe tip. One probe tip is inclined at a 20° angle relative to the horizontal direction, whereas the other tip is aligned with the horizontal direction. Initially, both probes were built exactly the same way (identical dimensions, components, etc.) and included a 20° tip angle for use in the supersonic wind tunnel. The tip was inclined at 20° to facilitate measurements near the wind tunnel floor. After the experiments for the current study began in the hypersonic wind tunnel, it was discovered that the concentration probe responds negatively to flow angularity and one probe was modified to avoid negative flow angularity effects.

The effect of flow angularity on this type of instrument was previously studied by Ninnemann et al⁴³. Ninnemann measured the sensitivity of a similar probe to inlet air angle for a range of flow angles from 0 - 20° using a small supersonic tunnel designed to operate at Mach 1.5 using any air-helium mixture. He concluded that 20° of flow angularity influences the measurement by a maximum value of about 3% of the reading in terms of mole fraction of helium. Thus, the effect of flow angularity on this measurement is small. Nevertheless, in order to avoid any negative flow angularity effects, an adapter piece was built to change the tip angle of one probe to 0° (aligned with the horizontal direction) for use in the hypersonic tunnel. Measurements in the hypersonic tunnel are made at the end of a duct and are not constrained by a wall (see Figure 2.18).

	Straight Tip Probe	Angled Tip Probe
Tip Angle (relative to horizontal)	0°	20°
Tip Material	416 Stainless Steel	Brass
Hot-Film Sensor	TSI Model 1220-20	TSI Model 1210-20
Maximum Ambient Temperature Rating	300°C	93°C
Thermocouple Type	T	K
Method for Cone-Static Measurement	Attached Cone-Static Probe	Separate Cone-Static Probe

Table B.1: Comparison of the straight tip and angled tip concentration probe configurations

Several additional design improvements were incorporated into the straight tip concentration probe at the same time that the tip angle was modified. These design improvements include the following:

- The tip material was changed to 416 stainless steel for improved wear resistance
- The maximum ambient temperature rating for the probe was increased to 300°C through the use of high temperature materials including the following:
 - TSI model 1220-20 hot-film sensor (same nominal dimensions and electrical properties as model 1210-20, but higher ambient temperature rating)
 - High temperature epoxy
 - High temperature silicone gaskets
- The thermocouple was changed to type T for improved accuracy (the accuracy rating of type T is +/- 0.5°C, whereas the accuracy rating of type K is +/- 1.1°C)
- A cone-static probe was attached to concentration probe to allow simultaneous concentration and cone-static measurements to be made

Appendix C: Uncertainty Analysis

An uncertainty analysis was performed to assess the uncertainties associated with all of the different measurements that were performed for this study. The uncertainty analysis assumes single-sample measurements were performed. The analysis also assumes a 95% confidence level, which means that the analysis is valid for 95% of the measured data. The uncertainty analysis is divided into four different sections (1) boundary layer measurements, (2) injectant mass flow rate measurements, (3) concentration measurements, and (4) Mach number and total pressure measurements. Many different varieties of pressure transducers and thermocouples were used to obtain the experimental data. Table C.1 gives a summary of the accuracy ratings for all of the different pressure transducers and thermocouples that were used for this study. These accuracy ratings were considered as factors that contributed to the measurement uncertainties found in all sections of the following analysis. In addition to the accuracy ratings of these sensors, the uncertainty analysis considered several other contributing factors as well, which are described in the subsequent sections.

In all of the following sections, a common procedure is used. First, the individual variables that contribute to the uncertainty of a measurement are identified. Next, the amount of uncertainty that each variable contributes to the measurement is calculated. Finally, the contributions of the individual variables are combined to determine the overall uncertainty of the measurement. For example, if the measurement of a quantity x depends on variables y and z (i.e. $x = y^2z$ or $x = y/z$, etc.) with uncertainties δy and δz (i.e. y has a true value of $y \pm \delta y$), the uncertainty of quantity x is:

$$\delta x = \sqrt{\left(\frac{\partial x}{\partial y} \delta y\right)^2 + \left(\frac{\partial x}{\partial z} \delta z\right)^2} \quad (\text{C.1})$$

The method for combining the uncertainty contributions from individual variables is known as the square root of the sum of the squares. The theoretical foundation for this method is described in Coleman and Steele⁶².

Measurement	Parameter	Transducer Range or Thermocouple Type	Accuracy Rating
Orifice Plate Flow Meter	p_1	0-13.6 atm (0-200 psia)	+/- 0.30% FS (+/- 0.041 atm)
	T_1	Type E	+/- 1 K
	Δp	+/- 6.80 atm (+/- 100 psi)	+/- 0.25% FS (+/- 0.017 atm)
Concentration Probe (Straight Tip)	p_{03}	0-3.40 atm (0-50 psia)	+/- 0.30% FS (+/- 0.010 atm)
	T_{03}	Type T	+/- 0.5 K
Concentration Probe (Angled Tip)	p_{03}	0-3.40 atm (0-50 psia)	+/- 0.30% FS (+/- 0.010 atm)
	T_{03}	Type K	+/- 1.1 K
Triple-Rake Probe	p_{cone}	0-1.36 atm (0-20 psia)	+/- 0.087% FS (+/- 0.0012 atm)
	p_{02}	0-3.40 atm (0-50 psia)	+/- 0.30% FS (+/- 0.010 atm)
	T_{02}	Type E	+/- 1 K
Cone-Static Probe	p_{cone}	0-1.36 atm (0-20 psia)	+/- 0.087% FS (+/- 0.0012 atm)
Five-Hole Probe	$p_a - p_b, p_{02}$	+/- 3.40 atm (+/- 50 psi)	+/- 0.23% FS (+/- 0.0078 atm)
HST Plenum (Mach 2 Conditions)	$p_{0\infty}$	0-6.80 atm (0-100 psia)	+/- 0.30% FS (+/- 0.020 atm)
HST Plenum (Mach 4 Conditions)	$p_{0\infty}$	0-20.4 atm (0-300 psia)	+/- 0.30% FS (+/- 0.061 atm)
SST Plenum	$p_{0\infty}$	0-20.4 atm (0-300 psia)	+/- 0.30% FS (+/- 0.061 atm)
	$T_{0\infty}$	Type E	+/- 1 K
Free-Jet Facility Plenum	$p_{0\infty}$	0-20.4 atm (0-300 psia)	+/- 0.30% FS (+/- 0.061 atm)

Table C.1: Accuracy ratings for pressure transducers and thermocouples

C.1 Boundary Layer Measurements

The following analysis estimates the uncertainties in the normalized Pitot pressure data ($p_{02} / p_{0\infty}$) and Mach number data obtained for the boundary layer measurements of the hypersonic tunnel.

These measurements were performed with the triple-rake probe. To obtain these measurements, three different pressure transducers were used to measure the Pitot pressure (p_{02}), cone-static pressure (p_{cone}), and tunnel plenum pressure ($p_{0\infty}$). The individual uncertainties of these three transducers were considered as the contributing factors to the overall uncertainties of these measurements. Thus, the uncertainty associated with the normalized Pitot pressure measurement is:

$$\delta\left(\frac{p_{02}}{p_{0\infty}}\right) = \sqrt{\left[\frac{\partial(p_{02} / p_{0\infty})}{\partial p_{02}} \delta p_{02}\right]^2 + \left[\frac{\partial(p_{02} / p_{0\infty})}{\partial p_{0\infty}} \delta p_{0\infty}\right]^2} \quad (\text{C.2})$$

And the uncertainty associated with the Mach number measurement is:

$$\delta M = \sqrt{\left(\frac{\partial M}{\partial p_{02}} \delta p_{02}\right)^2 + \left(\frac{\partial M}{\partial p_{cone}} \delta p_{cone}\right)^2 + \left(\frac{\partial M}{\partial p_{0\infty}} \delta p_{0\infty}\right)^2} \quad (\text{C.3})$$

It is necessary to include the uncertainty associated with the plenum pressure transducer in equation C.3, because the cone-static and Pitot pressure data from multiple runs was normalized with the tunnel plenum pressure in order to calculate the ratio p_c / p_{02} at each spatial location, which was then used to determine Mach number. For example, to calculate the ratio p_c / p_{02} at each spatial data point, values for $p_c / p_{0\infty}$ and $p_{02} / p_{0\infty}$ from separate runs were first calculated for that data point. Then, the ratio of p_c / p_{02} was calculated by:

$$\frac{p_c}{p_{02}} = \frac{p_c}{p_{0\infty}} \frac{p_{0\infty}}{p_{02}} \quad (\text{C.4})$$

Normalizing the p_c and p_{02} data in this manner accounts for the influence of the tunnel plenum pressure on these measurements, which varies during a run and from run to run.

Using Table C.1, the individual uncertainties that apply to equations C.2 and C.3 are:

- $\delta p_{02} = 0.010$ atm
- $\delta p_{cone} = 0.0012$ atm
- $\delta p_{0\infty} = 0.020$ atm (Mach 2 conditions) or 0.061 atm (Mach 4 conditions)

The uncertainties associated with each individual normalized Pitot pressure and Mach number data point were calculated numerically using equations C.2 and C.3 and plotted using error bars in Figures 2.5 – 2.8. The average uncertainty associated with the normalized Pitot pressure data was found to be approximately +/- 0.9% of the measured value, whereas the average uncertainty associated with the Mach number data was found to be approximately +/- 1.1% of the measured value.

C.2 Injectant Mass Flow Rate Measurements

Two different types of instruments were used to measure the injectant mass flow rate: (1) digital mass flow controllers and (2) an orifice plate flow meter. This section describes how the uncertainties associated with the injectant mass flow rates measured by these two devices were determined.

C.2.1 Mass Flow Controllers

The uncertainties associated with the injectant mass flow rates measured by the mass flow controllers were determined based upon the specifications provided by the manufacturer. According to these specifications, the accuracy rating of the mass flow controllers depends upon flow rate. For 0-83% of full-scale output, the mass flow controllers are rated to be accurate to +/- (0.2% full-scale + 0.5% reading). For 83-100% of full-scale output, the mass flow controllers are rated to be accurate to +/- 2% of full-scale output. The full-scale output of the flow controllers depends upon the gas that is being controlled. For the gases used in the experiments, the full-scale output of one flow controller is as follows:

- Helium: 12.50 g/s (4200 SLPM)
- Methane: 27.86 g/s (2335 SLPM)
- Air: 64.72 g/s (3003 SLPM)

Thus, for the mass flow rates used with the flow controllers in the experiments, the accuracy of the system of two flow controllers for each type of gas is as follows:

- Helium (90% full-scale operation): 22.5 g/s +/- 0.5 g/s (2.2% of reading)
- Methane (85% full-scale operation): 47.29 g/s +/- 1.12 g/s (2.4% of reading)
- Air (48% full-scale operation): 62.66 g/s +/- 0.58 g/s (0.9% of reading)

C.2.2 Orifice Plate Flow Meter

The following analysis estimates the uncertainties in the injectant mass flow rates measured by the orifice plate flow meter. To obtain these measurements, three different sensors were used to measure the upstream pressure (p_1), the upstream temperature (T_1), and the differential pressure (Δp). The individual uncertainties of these three sensors, which are shown in Table C.1, were considered as the contributing factors to the overall uncertainty of this measurement. Thus, the uncertainty associated with the injectant mass flow rate measured by the orifice plate flow meter is:

$$\delta \dot{m}_{Orifice} = \sqrt{\left(\frac{\partial \dot{m}_{Orifice}}{\partial p_1} \delta p_1\right)^2 + \left(\frac{\partial \dot{m}_{Orifice}}{\partial \Delta p} \delta \Delta p\right)^2 + \left(\frac{\partial \dot{m}_{Orifice}}{\partial T_1} \delta T_1\right)^2} \quad (C.5)$$

The orifice plate flow meter was used for experiments with helium injection at two different mass flow rates, 22.5 g/s and 30 g/s. Equation C.5 was applied to calculate the measurement uncertainty at these two different mass flow rates, which was found to be approximately:

- Helium (22.5 g/s operation): 22.5 g/s +/- 0.11 g/s (0.5% of reading)
- Helium (30 g/s operation): 30 g/s +/- 0.12 g/s (0.4% of reading)

C.3 Concentration Measurements

An extensive uncertainty analysis was performed to determine the uncertainties associated with the concentration probe measurements. The following factors were considered as contributors to the measurement uncertainty of the concentration probe:

- Day-to-day variations in the hot-film voltage level due to factors such as instrument drift and aging
- Uncertainty associated with the pressure transducer measurement
- Uncertainty associated with the thermocouple measurement
- Data reduction code (includes curve fitting of the calibration data)
- Calibration procedure
- Flow angularity

Therefore, the governing equation for the uncertainty in the injectant mass fraction measured by the concentration probe is:

$$\delta\alpha = \sqrt{\left(\frac{\partial\alpha}{\partial V}\delta V\right)^2 + \left(\frac{\partial\alpha}{\partial p_{03}}\delta p_{03}\right)^2 + \left(\frac{\partial\alpha}{\partial T_{03}}\delta T_{03}\right)^2 + \left(\frac{\partial\alpha}{\partial\lambda}\delta\lambda\right)^2 + \left(\frac{\partial\alpha}{\partial\kappa}\delta\kappa\right)^2 + \left(\frac{\partial\alpha}{\partial\theta}\delta\theta\right)^2} \quad (\text{C.6})$$

where the variable λ represents the data reduction code, the variable κ represents the calibration procedure, and the variable θ represents flow angularity. The following individual uncertainties for equation C.6 were estimated as:

- $\delta V = 1\%$ of measured value
- $\delta p_{03} = 0.010$ atm (from Table C.1)
- $\delta T_{03} = 1.1$ K (from Table C.1)

The value of δV was estimated by analyzing pre-run data that was recorded over the course of the study. The uncertainty contribution from the data reduction code was estimated using a code validation procedure, which is discussed in the following section. The uncertainty contribution

from the calibration procedure was estimated by considering the accuracy of the pressure transducer used to measure the pressure of the calibration tank. The pressure of the calibration tank was measured with a 0-6.80 atm (0-100 psia) transducer with an accuracy rating of +/- 0.30% FS (+/- 0.020 atm). The uncertainty due to the filling procedure for the calibration tank (i.e. over-filling or under-filling the calibration tank) was found to be negligible relative to the uncertainty due to the tank pressure measurement, provided that the calibration procedure is performed carefully. The uncertainty contribution due to flow angularity was estimated to be 3% of the measured mole fraction. The justification for this assumption was previously discussed in Appendix B.

C.3.1 Data Reduction Code Validation

A data reduction code validation procedure for the concentration probe was developed that serves two purposes: (1) it verifies that the data reduction code is working properly and (2) it gives a quantitative measure of how well the code works, which is used as an input for the uncertainty analysis. The code validation procedure is performed as follows:

1. The calibration data points (a set of hot-film voltage, pressure, and temperature values) are used as inputs to the data reduction code
2. The code is used to calculate the mass fraction values for each data point
3. The calculated mass fraction values are compared against the known mass fraction values from the calibration
4. Any error in the calculated values vs. the known values is residual error in the data reduction code

Table C.2 shows the average residual errors for the data reduction code that were calculated using this procedure for values of mole fraction ranging from 10% - 80%.

Mole Fraction	Mass Fraction He	Helium Avg. % Residual Error	Mass Fraction Methane	Methane Avg. % Residual Error
0.10	0.015	8.5%	0.058	13.7%
0.20	0.033	5.1%	0.122	6.0%
0.30	0.056	3.6%	0.192	3.5%
0.40	0.084	3.0%	0.270	3.2%
0.50	0.121	2.5%	0.356	3.0%
0.60	0.172	1.9%	0.454	3.4%
0.70	0.244	2.3%	0.564	2.1%
0.80	0.356	2.0%	0.689	2.6%

Table C.2: Data reduction code validation results for the concentration probe

C.3.2 Analysis Results

The measurement uncertainty of the concentration probe varies depending on its operating conditions. The uncertainty of the probe is highly dependent on gas composition. For example, the measurement uncertainty of the probe for a helium-air mixture is different than for a methane-air mixture. Furthermore, the mass fraction of helium or methane in each mixture also significantly affects the measurement uncertainty. Lastly, the measurement uncertainty of the probe is also slightly dependent on the pressure conditions. To consider all of these factors, the measurement uncertainty of the concentration probe was computed for both helium-air mixtures and methane-air mixtures over a range of mass fraction and pressure values. Tables C.3 and C.5 show the measurement uncertainty of the concentration probe as a function of mass fraction and pressure for helium-air and methane-air mixtures respectively. These calculations demonstrate that the measurement uncertainty of the probe is only slightly dependent on pressure. Thus, to create a more general approximation for the measurement uncertainty, these tables were averaged over the typical experimental pressure conditions (concentration probe pressure \approx 0.3 – 1.4 atm) to create Table C.4, Table C.6, and Figure 2.26.

		Concentration Probe Pressure [atm]												
		0.3	0.4	0.5	0.6	0.7	0.8	0.9	1	1.2	1.4	1.6	1.8	2
Mass Fraction He	0.01	33.2	32.5	32.1	31.9	31.8	31.7	31.6	31.6	31.5	31.4	31.4	31.3	31.3
	0.02	23.5	22.3	21.6	21.1	20.8	20.5	20.3	20.1	19.8	19.6	19.4	19.2	19.1
	0.03	17.7	16.9	16.3	16.0	15.8	15.6	15.4	15.3	15.1	14.9	14.7	14.6	14.5
	0.04	13.9	13.4	13.1	12.9	12.8	12.7	12.6	12.6	12.5	12.4	12.3	12.3	12.2
	0.05	12.4	12.0	11.7	11.6	11.5	11.4	11.3	11.3	11.2	11.1	11.0	11.0	11.0
	0.06	11.9	11.4	11.1	11.0	10.9	10.8	10.7	10.6	10.5	10.5	10.4	10.4	10.3
	0.07	11.2	10.8	10.5	10.3	10.2	10.1	10.1	10.0	9.9	9.9	9.8	9.7	9.7
	0.08	10.6	10.2	9.9	9.8	9.6	9.6	9.5	9.4	9.4	9.3	9.2	9.2	9.2
	0.09	9.8	9.3	9.1	9.0	8.9	8.8	8.7	8.6	8.6	8.5	8.4	8.4	8.3
	0.1	9.6	9.2	8.9	8.8	8.7	8.6	8.5	8.5	8.4	8.3	8.3	8.2	8.2
	0.11	9.5	9.1	8.9	8.7	8.6	8.5	8.5	8.4	8.3	8.3	8.2	8.2	8.1
	0.12	9.2	8.8	8.6	8.5	8.4	8.3	8.2	8.2	8.1	8.1	8.0	8.0	7.9
	0.13	8.9	8.5	8.3	8.2	8.1	8.0	8.0	7.9	7.9	7.8	7.8	7.7	7.7
	0.14	8.9	8.5	8.3	8.2	8.1	8.0	7.9	7.9	7.8	7.8	7.7	7.7	7.7
	0.15	8.9	8.5	8.3	8.2	8.1	8.0	7.9	7.9	7.8	7.8	7.7	7.7	7.6
	0.2	9.2	8.6	8.2	8.0	7.8	7.7	7.6	7.5	7.4	7.3	7.2	7.1	7.1
	0.25	8.4	8.0	7.8	7.7	7.6	7.5	7.5	7.4	7.4	7.3	7.3	7.2	7.2
	0.3	8.7	8.4	8.2	8.1	8.1	8.0	8.0	7.9	7.9	7.8	7.8	7.8	7.8
	0.35	9.7	9.1	8.8	8.7	8.5	8.4	8.4	8.3	8.2	8.1	8.1	8.0	8.0

Table C.3: Concentration probe uncertainty [+/- (% measured value)] as a function of mass fraction and pressure for helium-air mixtures

		+/- (Mass Fraction He)	+/- (% Measured Value)
Mass Fraction He	0.01	0.0032	31.9
	0.02	0.0042	20.9
	0.03	0.0048	15.9
	0.04	0.0051	12.9
	0.05	0.0058	11.5
	0.06	0.0066	10.9
	0.07	0.0072	10.3
	0.08	0.0078	9.7
	0.09	0.0080	8.9
	0.1	0.0088	8.8
	0.11	0.0095	8.7
	0.12	0.0101	8.4
	0.13	0.0106	8.2
	0.14	0.0114	8.1
	0.15	0.0122	8.1
	0.2	0.0159	7.9
0.25	0.0191	7.7	
0.3	0.0243	8.1	
0.35	0.0302	8.6	

Table C.4: Average concentration probe uncertainty for helium-air mixtures

		Concentration Probe Pressure [atm]												
		0.3	0.4	0.5	0.6	0.7	0.8	0.9	1	1.2	1.4	1.6	1.8	2
Mass Fraction Methane	0.02	116.0	109.1	105.2	102.5	100.6	99.1	97.8	96.8	95.2	93.9	92.8	91.9	91.2
	0.03	78.8	74.1	71.4	69.6	68.3	67.3	66.4	65.7	64.6	63.7	63.0	62.4	61.9
	0.05	50.0	47.0	45.3	44.1	43.3	42.6	42.1	41.6	40.9	40.3	39.9	39.5	39.1
	0.07	38.4	36.1	34.8	33.9	33.2	32.7	32.3	32.0	31.5	31.0	30.7	30.4	30.2
	0.09	31.5	29.5	28.4	27.7	27.2	26.8	26.4	26.2	25.7	25.4	25.1	24.8	24.6
	0.11	26.5	24.9	23.9	23.2	22.8	22.4	22.1	21.9	21.5	21.2	21.0	20.8	20.6
	0.13	22.9	21.3	20.4	19.8	19.4	19.0	18.7	18.5	18.1	17.8	17.6	17.4	17.2
	0.15	20.3	18.8	18.0	17.4	17.0	16.7	16.4	16.2	15.8	15.6	15.3	15.1	15.0
	0.2	17.6	16.3	15.6	15.1	14.8	14.5	14.3	14.1	13.8	13.6	13.4	13.2	13.1
	0.25	15.0	14.1	13.6	13.3	13.0	12.9	12.8	12.7	12.5	12.4	12.3	12.2	12.1
	0.3	10.7	10.7	10.8	11.0	11.2	11.3	11.5	11.6	11.9	12.2	12.4	12.6	12.8
	0.35	12.1	11.7	11.5	11.4	11.4	11.4	11.4	11.4	11.4	11.5	11.5	11.6	11.6
	0.4	14.1	13.1	12.4	12.0	11.6	11.4	11.2	11.0	10.8	10.6	10.4	10.3	10.2
	0.45	14.7	12.9	11.9	11.3	10.8	10.5	10.2	10.0	9.7	9.4	9.3	9.1	9.0
	0.5	14.8	12.6	11.3	10.5	9.9	9.5	9.1	8.8	8.4	8.1	7.9	7.7	7.5
	0.55	12.4	11.0	10.2	9.6	9.3	9.0	8.8	8.6	8.4	8.2	8.0	7.9	7.8
	0.6	9.5	9.2	9.0	8.9	8.9	8.9	8.9	8.9	8.9	8.9	8.9	8.9	9.0
0.65	9.3	9.0	8.9	8.9	8.9	8.9	8.9	8.9	8.9	9.0	9.0	9.0	9.1	

Table C.5: Concentration probe uncertainty [± (% measured value)] as a function of mass fraction and pressure for methane-air mixtures

		± (Mass Fraction Methane)	± (% Measured Value)
Mass Fraction Methane	0.02	0.020	101.6
	0.03	0.021	69.0
	0.05	0.022	43.7
	0.07	0.024	33.6
	0.09	0.025	27.5
	0.11	0.025	23.0
	0.13	0.025	19.6
	0.15	0.026	17.2
	0.2	0.030	14.9
	0.25	0.033	13.2
	0.3	0.034	11.3
	0.35	0.040	11.5
	0.4	0.047	11.8
	0.45	0.050	11.1
	0.5	0.052	10.3
	0.55	0.052	9.5
	0.6	0.054	9.0
0.65	0.058	8.9	

Table C.6: Average concentration probe uncertainty for methane-air mixtures

Table C.7 shows a breakdown of the measurement uncertainty for the concentration probe in terms of the contributions of individual variables. The calculations in Table C.7 were performed for the case of helium mass fraction = 0.07, total pressure (p_{03}) = 1 atm, and total temperature (T_{03}) = 294 K, which is a condition that occurred in both the flush-wall and the strut injector experiments. From these calculations, it is evident that the largest contributor to the uncertainty of the concentration probe is the day-to-day fluctuations in the hot-film voltage.

The calculations in Table C.7 also demonstrate that the measurement uncertainty for the two different configurations of the concentration probe (straight tip and angled tip) is approximately the same. The differences between the two different probe configurations that have implications on the measurement uncertainty are (1) the tip angle due to flow angularity effects and (2) the type of thermocouple used. In Table C.7, the overall measurement uncertainty of the probe with and without the flow angularity contribution is calculated. The differences between these two calculations are small, which demonstrates that the effect of flow angularity is also small. In addition, the contribution of the thermocouple to the overall measurement uncertainty of the concentration probe is very small. Thus, based upon these calculations, the measurement uncertainty for the two different configurations of the concentration probe is approximately the same.

Source of Uncertainty	Uncertainty (+/- Mass Fraction He)	Uncertainty (+/- % of Mass Fraction Reading)
Hot-Film	0.0058	8.3%
Pressure Transducer	0.0008	1.1%
Thermocouple	0.0004	0.5%
Data Reduction Code	0.0032	4.6%
Calibration Procedure	0.0023	3.3%
Flow Angularity (20°)	0.0033	4.7%
Total (with Flow Angularity)	+0.0078 / -0.0070	+11.2% / -10.0%
Total (without Flow Angularity)	= +/- 0.0070	+/- 10.0%

Table C.7: Concentration probe uncertainty breakdown for the case of helium mass fraction = 0.07, total pressure = 1 atm, and total temperature = 294 K

From examining Figure 2.26 and Tables C.2 – C.6, some trends in the uncertainty results for the concentration probe are evident. The probe calibration data, which gives a physical representation of the governing equations for the probe, can be used to explain these trends.

First, the measurement uncertainty for a helium-air mixture is less than that of a methane-air mixture. Comparing the calibration curves for the two different gas mixtures (Figures 2.23 – 2.24) reveals that the curves for the methane-air mixture are compacted, which demonstrates reduced sensitivity (reduced voltage output range) and increased uncertainty. Second, the measurement uncertainty of the probe decreases as mass fraction increases. This trend can also be explained using calibration data, because the calibration curves become more spaced out as mass fraction increases, which demonstrates increased sensitivity. Finally, the measurement uncertainty of the probe increases as the total pressure decreases. This can be explained by the convergence of the calibration curves as total pressure decreases, which demonstrates a decrease in sensitivity.

C.4 Mach Number and Total Pressure Measurements

Two different methods were employed to measure values of Mach number and total pressure depending on the flow conditions. For measurement of an airflow, the five-hole probe alone was used to measure these values. For measurement of a gas mixture, a multiple probe survey method was used. Each of these methods was analyzed to determine the uncertainties associated with these measurements.

C.4.1 Measurement of an Airflow

The following factors were considered as contributors to the uncertainties associated with the Mach number and total pressure measurements of an airflow, which were performed with the five-hole probe:

- Uncertainties of the 5 piezoresistive pressure transducers embedded within the probe
- Mach number calibration procedure
- Flow angularity calibration procedure
- Data reduction code (includes interpolation of the calibration data)

Therefore, the governing equation for the uncertainty in the Mach number (M_1) measured by the five-hole probe is:

$$\delta M_1 = \sqrt{\left(\frac{\partial M_1}{\partial p_{02}} \delta p_{02}\right)^2 + \sum_{i=a}^d \left(\frac{\partial M_1}{\partial p_i} \delta p_i\right)^2 + \left(\frac{\partial M_1}{\partial \xi} \delta \xi\right)^2 + \left(\frac{\partial M_1}{\partial \omega} \delta \omega\right)^2 + \left(\frac{\partial M_1}{\partial \lambda} \delta \lambda\right)^2} \quad (\text{C.7})$$

where the variable ξ represents the Mach number calibration procedure, the variable ω represents the flow angularity calibration procedure, and the variable λ represents the data reduction code. Once the uncertainty in the Mach number (M_1) is known at a certain condition (of M_1 , p_{02} , and γ), the corresponding uncertainty in the total pressure (p_{01}) at that condition can be found using equations 2.28 and 2.29. The following individual uncertainties for equation C.7 were estimated as:

- $\delta p_{02} = 0.0078$ atm (from Table C.1)
- $\delta p_a = \delta p_b = \delta p_c = \delta p_d = 0.0078$ atm (from Table C.1)

The uncertainty contribution from the Mach number calibration procedure was estimated by considering the uncertainties of the triple-rake probe transducers, the uncertainty of the supersonic tunnel plenum pressure transducer, the uncertainty associated with misalignment between the triple-rake probe and the five-hole probe, and the uncertainty induced by flow angularity present in the boundary layer. The uncertainties of the plenum pressure and triple-rake probe transducers are shown in Table C.1, the alignment of the two probes was assumed to be within +/- 0.25 mm, and the amount of flow angularity present in the boundary layer was assumed to be 2°. The uncertainty contribution from the flow angularity calibration procedure was estimated by assuming the procedure was accurate to +/- 0.5°. The uncertainty contribution from the data reduction code was estimated using a code validation procedure, which is discussed in the following section.

C.4.1.1 Data Reduction Code Validation

A data reduction code validation procedure for the five-hole probe was used to obtain a quantitative measure of how well the code works, which is used as an input for the uncertainty analysis. The code validation procedure is performed as follows:

1. The calibration data points (a set of 5-hole probe pressure values) from the flow angularity calibration are used as inputs to the data reduction code
2. The code is used to calculate the Mach number, total pressure, and flow angles for each data point
3. The calculated values from step 2 are compared against the known values from the calibration

4. Any error in the calculated values vs. the known values is residual error in the data reduction code

Table C.8 shows the average residual errors for the data reduction code that were calculated using this procedure.

Pitch Angle (θ)	Mach Number	Total Pressure	Pitch Angle (θ)	Roll Angle (ϕ)
	Avg. % Residual Error	Avg. % Residual Error	Avg. Residual Error	Avg. Residual Error
0°-5°	1.3%	3.4%	0.2°	2.6°
5°-10°	1.2%	3.3%	0.5°	0.8°
10°-15°	1.2%	3.1%	1.0°	0.6°

Table C.8: Data reduction code validation results for the five-hole probe

C.4.1.2 Analysis Results

The uncertainty of the five-hole probe varies depending on its operating conditions. Uncertainty values were computed using equation C.7 based upon the typical operating conditions that the probe encounters at freestream Mach numbers of 2, 3, and 4. The results of the uncertainty analysis for the five-hole probe are shown in Table 2.1. The largest contributors to the measurement uncertainty of the five-probe were the uncertainties associated with the Mach number calibration procedure and the uncertainties associated with the five piezoresistive pressure transducers. Misalignment of the two probes is the major concern for the Mach number calibration procedure, whereas the flow angularity present in the boundary layer is a much lesser concern. This calculation assumed 2° of flow angularity was present in the boundary layer, which resulted in an uncertainty in M_I of approximately 0.2%.

C.4.2 Measurement of a Gas Mixture

The following factors were considered as contributors to the uncertainties associated with the Mach number and total pressure measurements of a gas mixture, which were performed using the multiple probe survey method:

- Uncertainty of the concentration measurement (Figure 2.26 applies)
- Uncertainties of the pressure transducers for the cone-static probe, five-hole probe, and hypersonic tunnel plenum pressure measurements
- Flow angularity

Again, it is necessary to include the uncertainty associated with the plenum pressure transducer here, because the cone-static and Pitot pressure data from multiple runs was normalized with the tunnel plenum pressure in order to calculate the ratio p_c / p_{02} at each spatial location, which was then used to determine Mach number. It is also necessary to include the uncertainty associated with flow angularity, since no iterations are performed to correct for flow angularity for this case. Additionally, the uncertainty due to the data reduction code is probably not a significant factor for this case, since an exact theoretical method was applied to determine Mach number that was calculated for a large number of points such that very little interpolation was required.

Considering these factors, the governing equation for the uncertainty in the Mach number (M_1) measured using the multiple probe survey method is:

$$\delta M_1 = \sqrt{\left(\frac{\partial M_1}{\partial \alpha} \delta \alpha\right)^2 + \left(\frac{\partial M_1}{\partial p_c} \delta p_c\right)^2 + \left(\frac{\partial M_1}{\partial p_{02}} \delta p_{02}\right)^2 + \left(\frac{\partial M_1}{\partial p_{0\infty}} \delta p_{0\infty}\right)^2 + \left(\frac{\partial M_1}{\partial \theta} \delta \theta\right)^2} \quad (\text{C.8})$$

where the variable θ represents flow angularity. Once the uncertainty in the Mach number (M_1) is known at a certain condition (of M_1 , p_{02} , and γ), the corresponding uncertainty in the total pressure (p_{01}) at that condition can be found again using equations 2.28 and 2.29.

In equation C.8, the uncertainty associated with concentration measurement was estimated using Tables C.4 and C.6. The uncertainties associated with the cone-static pressure, Pitot pressure, and plenum pressure measurements are shown in Table C.1. Finally, the uncertainty contribution due to flow angularity was estimated by performing the code validation procedure for the five-hole probe, but without iterations to correct for flow angularity. Table C.9 shows the contribution of flow angularity to the uncertainty of this measurement procedure.

Pitch Angle (θ)	Mach Number	Total Pressure
	Avg. % Residual Error	Avg. % Residual Error
0°-5°	1.3%	3.4%
5°-10°	1.7%	4.7%
10°-15°	2.4%	6.9%

Table C.9: Effect of flow angularity on the Mach number and total pressure measurement uncertainties for gas mixtures

C.4.2.1 Analysis Results

The results of the uncertainty analysis for the multiple probe survey method are shown in Table 2.2 and discussed in Section 2.4.2.1. It is also noteworthy that a comparison of Tables C.8 and C.9 demonstrates that the correction factors shown in Figure 2.33 are working properly. The calculations performed for Table C.8 included the correction factors, whereas the calculations performed for Table C.9 did not. From comparing these two tables, it is evident that the correction factors improved the accuracy of the data reduction code when flow angularity was present.

Appendix D: Proposed New Concentration Probe Design

D.1 Introduction

To improve upon the existing concentration probe design, a concept for a new concentration probe was developed with the primary goals of achieving both a reduction in size and a faster response time. This Appendix provides background information on different concentration probe designs, presents a concept for a new design, and analyzes the performance of the new design.

D.1.1 Desired Features for a Concentration Probe

The design of a probe for gas composition measurements is a difficult task that must achieve a balance between many design features. The following is a list of some of the main features that are desirable in a concentration probe design:

- Small inlet area (to achieve good spatial resolution)
- Small sampling volume
- Output independent of the velocity of the fluid relative to the probe
- Capability to detect multiple types of gases
- Fast response time (on the order of milliseconds)
- High frequency response (on the order of kHz)
- Minimal residence time of the sampled fluid inside the probe (on the order of milliseconds)
- Small overall probe volume
- High accuracy
- High reliability
- High strength (to withstand aerodynamic loads at supersonic Mach numbers)
- High temperature rating
- Robust
- Low cost

Several concentration probe designs have been previously developed, which prioritized design features differently. The design features of several previous designs will be discussed in detail, so as to give the reader background regarding the design choices that were made for the proposed new probe design.

D.1.2 Previous Concentration Probe Designs

Previous concentration probe designs have been developed by Ninnemann and Ng⁴³ (1989), Brown and Rebollo⁶³ (1972), Xillo et al.⁴⁵ (1998), and Maddalena⁴⁶ (2007). Figure D.1 shows a comparison of the four previous probe designs. Each probe design has unique design features and performance parameters, but all four probes have the same basic principle of operation. All of these probes are aspirating type probes, which are attached to a vacuum pump.

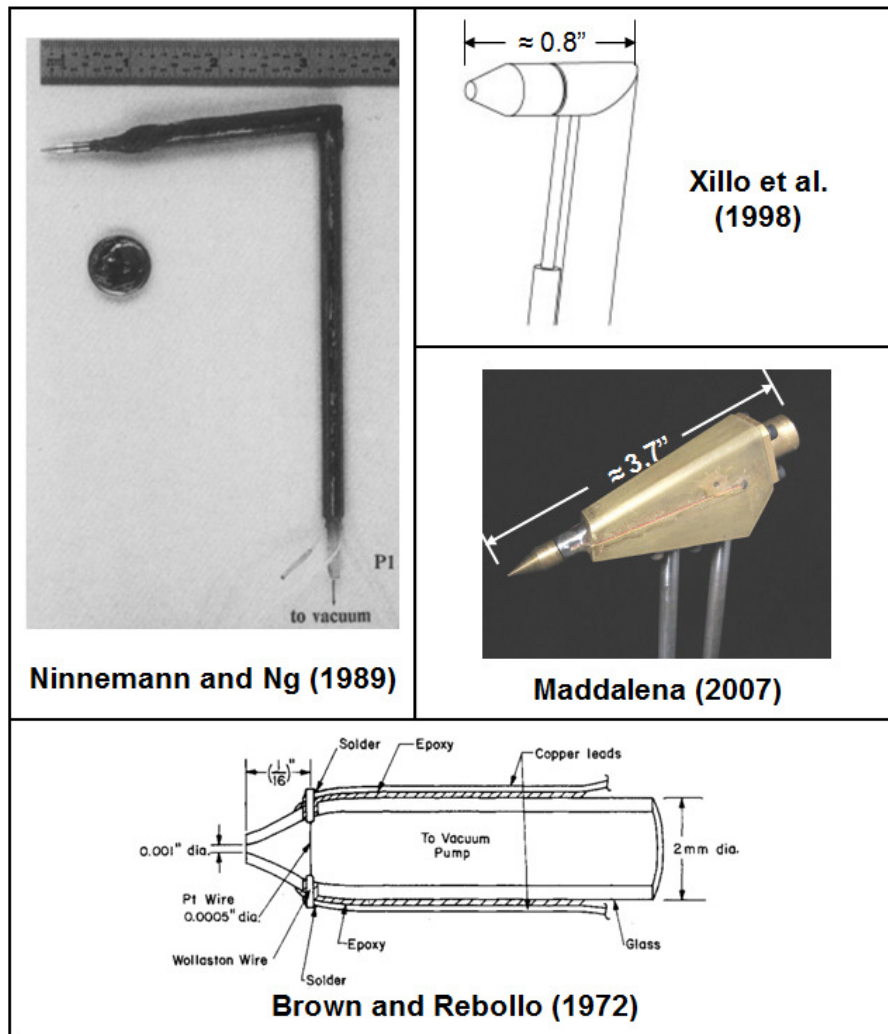


Figure D.1: Comparison of previous concentration probe designs

Another common feature of these probes is the use of a constant temperature hot-film or hot-wire sensor operating in a channel with a choked exit. Furthermore, these probes commonly use a diverging tip (i.e. nozzle). In the tip of the probe, the flow is initially accelerated until the point at which the normal shock occurs. After the normal shock, the flow is decelerated as the tip continues to diverge. Once the flow reaches the measurement plane, it has typically been decelerated to a Mach number on the order of 0.05. All of the probe designs incorporate hot-film and pressure measurements at the measurement plane. Temperature must also be measured and one of the main differences between the four previous designs is the method used for this measurement. The previous designs also differ in the placement of the sensors.

D.1.2.1 Ninnemann and Ng Design (Virginia Tech, 1989)

The Ninnemann and Ng design was one of the original concentration probe designs. It is capable of measuring mean concentration values. The probe used specially made hot-film sensor. A pressure transducer was connected externally via tubing. Temperature measurement was not incorporated into this probe design. The temperature had to be measured using a separate total temperature survey.

The primary advantages of this design are:

- Small inlet area (0.28 mm diameter) resulting in good spatial resolution
- Small tip size (3.18 mm outer diameter)
- Well streamlined probe body
- Probe tip was positioned at a 5 degree angle to allow measurements near a wind tunnel floor

The primary disadvantages of this design are:

- Unreliable hot-film sensor
- Lack of integrated temperature measurement
- Slow response time due to the externally located pressure transducer
- Poor frequency response (approximately 10 Hz)

D.1.2.2 Brown and Rebollo Design (Caltech, 1972)

The Brown and Rebollo design is one of the smallest known concentration probe designs. It achieved excellent spatial resolution. Not all of the details of this probe design are available in the published literature. The method of temperature measurement and the frequency response of the probe are unknown. However, comments can still be made regarding the advantages and disadvantages of this probe design.

The primary advantages of this design are:

- Very small inlet area (0.025 mm diameter) resulting in excellent spatial resolution
- Very small tip size (2 mm outer diameter)

The primary disadvantages of this design are:

- Fragility (the tip was made of blown glass)
- Reliability (a specially made hot-film sensor was used, which was probably significantly less reliable than a commercial hot-film sensor)

D.1.2.3 Xillo et al. Design (Virginia Tech, 1998)

The design goal for the probe built by Xillo et al. was to achieve the highest possible frequency response in order to measure fluctuating concentrations in supersonic turbulent flow. A frequency response of about 2.5 kHz was achieved. To achieve high frequency response, the measurement plane for the probe was located upstream of the normal shock that occurs in the probe tip. In the Ninnemann et al. and Maddalena probe designs, the measurement plane was located downstream of the normal shock. To achieve high frequency response, this design also incorporated a second hot-film sensor for temperature measurement and an integrated piezoresistive pressure transducer.

This probe established an approximate limit for the frequency response of an aspirating type concentration probe. Unfortunately, this limit is well below the frequency of fluctuating concentrations in supersonic turbulent flow.

The primary advantages of this design are:

- High frequency response (about 2.5 kHz)
- Fast response time (on the order of a few milliseconds)
- Incorporated temperature measurement (second hot-film sensor)
- Use of an integrated piezoresistive pressure transducer

The primary disadvantages of this design are:

- Large inlet area (2.18 mm diameter) resulting in poor spatial resolution
- Higher cost than other probes (mainly due to the cost of sensor components)
- Complexity

D.1.2.4 Maddalena Design (Virginia Tech, 2007)

The Maddalena design sought to improve the Ng design by incorporating an integrated thermocouple and a commercially available hot-film sensor for improved reliability. However, some of the desirable aspects of the Ng design were not maintained. The tip of the Maddalena probe was positioned at a 20° angle to the freestream to allow measurements near a wind tunnel floor. However, a 20° tip angle is undesirable as the probe responds negatively to flow angularity. The 5° tip angle that was originally used by Ng is a better choice. Furthermore, the Maddalena probe occupies significantly more volume than the Ng probe, which is also undesirable. The pressure transducer also remained externally located and connected via tubing, which is another undesirable design feature.

The primary advantages of this design are:

- High reliability
- Moderately small inlet area (0.64 mm diameter) resulting in good spatial resolution
- Integrated temperature measurement

The primary disadvantages of this design are:

- Large size
- Slow response time
- Poor frequency response (about 20 Hz)
- Uncertainty of the probe is somewhat limited by the 20° tip angle

D.1.2.5 Additional Background on the Use of the Ng and Maddalena Probes

Previous probes developed by Ninnemann et al. and Maddalena were originally designed for use in the Virginia Tech supersonic wind tunnel. The probe developed by Maddalena was used in the Virginia Tech hypersonic wind tunnel for this study, but the probe is not ideally suited for this application. One issue is the relative size of the probe in comparison to the cross-sectional area of the tunnel. The supersonic tunnel has a much larger cross-sectional area at the nozzle exit than the hypersonic tunnel does. When compared to the size of the supersonic tunnel, the Maddalena probe is relatively small. More importantly, the dimensions of the tip and capture area of the probe are small. The tip of the Maddalena probe was inclined at a 20° angle to allow measurements to be made near the tunnel wall. This tip inclination angle greatly increased the size of the probe, but it was not an issue as the probe was still small in comparison to the size of the supersonic tunnel. However, when compared to the size of the hypersonic tunnel, the Maddalena probe is relatively large and creates a non-trivial amount of blockage. Thus, it would be beneficial to develop a smaller probe that is more compatible with the hypersonic tunnel, but still compatible with the supersonic tunnel as well.

Another issue with the use of the Maddalena probe in the hypersonic tunnel is the response time of the probe. The Maddalena probe has a relatively long response time and it must be paused at each data point for 200 milliseconds, which is an experimentally determined value for obtaining repeatable measurements. For experiments run in the hypersonic tunnel, the Maddalena probe can measure 4-5 data points at 1-2 mm spacing during a 3.2 second run. Additionally, the hypersonic tunnel requires approximately 45-60 minutes to charge in between runs. With these constraints, completion of an entire flowfield survey for a circular scramjet combustor model in the hypersonic tunnel takes about 40-60 man hours. The response time of the Maddalena probe is not nearly as much of an issue when used with the supersonic tunnel, which typically runs for 20 seconds at Mach 4 conditions with 10-15 minutes to charge in between runs. If the pause time of the new probe can be reduced to 50 milliseconds, it would be able to measure 6-7 points at 1-2 mm spacing per hypersonic tunnel run. This would reduce the test time for injection and mixing experiments in the hypersonic tunnel by a factor of about 1/3, a significant improvement. The limiting factor in the response time of the Maddalena probe is the use of an externally mounted pressure transducer that is connected by tubing.

D.1.3 Design Goals for the New Concentration Probe

The new concentration probe will be designed to measure mean concentration values. Valuable data can be obtained by measuring mean concentration values. Moreover, the Xillo probe proved that the aspirating type probe design cannot achieve high enough frequency response to measure fluctuating concentrations in supersonic turbulent flow. Since relatively low frequency response (on the order of 10 Hz) is acceptable for measuring mean concentration values, improving the frequency response on the new probe is not a high priority goal.

The primary design goals for the new concentration probe are to:

1. Reduce size
2. Improve response time (reduce pause time at each data point to 50 ms)
3. Maintain high reliability
4. Improve frequency response (as high as possible, but lower priority than items 1-3)

In terms of the previous designs, the first goal of the new probe is to achieve a size similar to that of Ninnemann or Brown. The second goal is to achieve a response time in between that of Maddalena and Xillo. These were the two highest priority design goals.

D.2 Component Selection

To best achieve the design goals, the Maddalena probe design was chosen as a starting point. This design requires the following components: hot-film sensor, pressure transducer, and thermocouple. Each of these components was investigated to determine the best fit for the system in terms of size, performance, and cost. Figure D.2 shows a comparison of the different components that were considered for the new concentration probe.

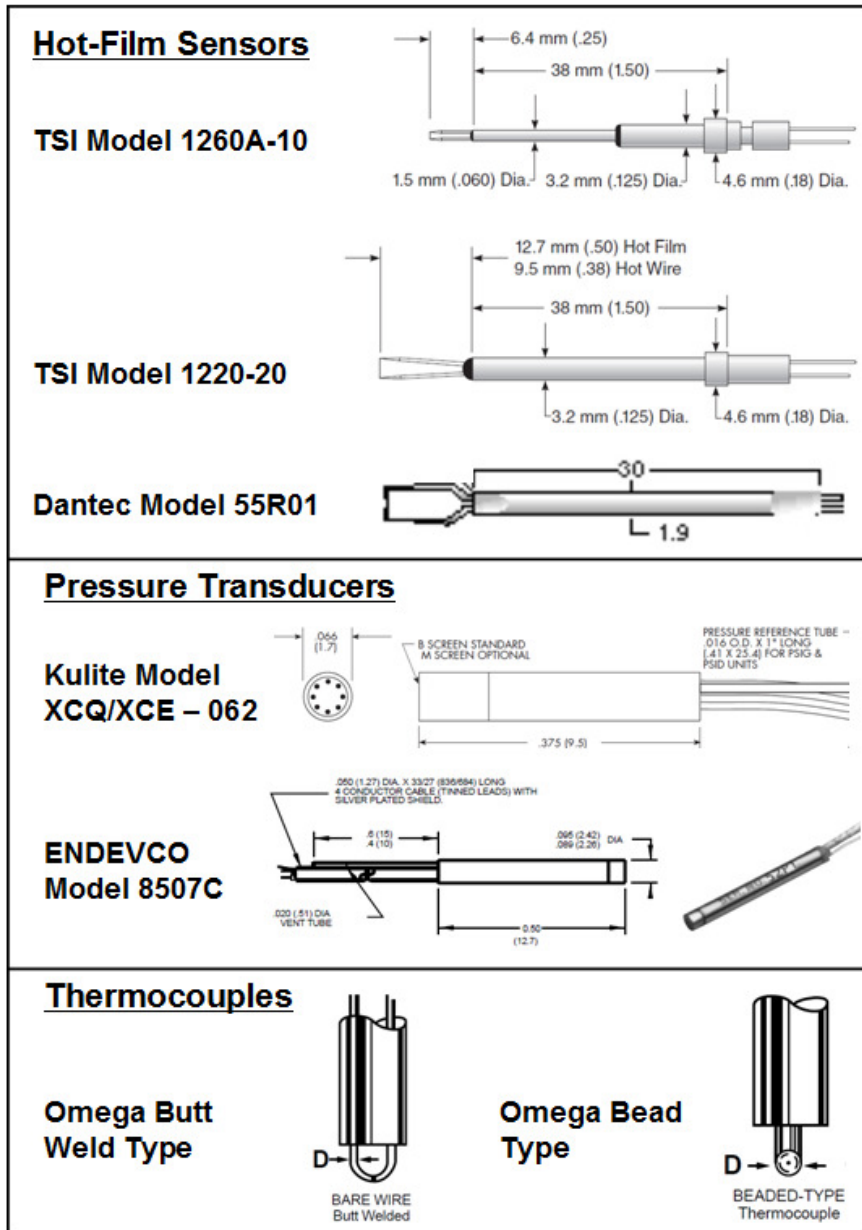


Figure D.2: Comparison of components considered for the new concentration probe

D.2.1 Hot-Film Sensor

Commercial hot-film sensors from TSI Incorporated and Dantec Dynamics were considered. The sensors from both companies were found to have very similar size, performance specifications, and cost. Table D.1 shows the pricing for the hot-film sensors that were considered.

Model	Cost
TSI 1260A-10	\$1,010
TSI 1220-20	\$665
Dantec 55R01	\$741

Table D.1: Pricing for hot-film sensors for the proposed new concentration probe

TSI model 1260A-10 was chosen for several reasons. First, the TSI sensor used in the Maddalena probe was proven to be highly reliable. Second, it is one of the smallest commercial sensors available. Model 1260A-10 was chosen over model 1220-20 as a trade-off between size and temperature rating. Model 1220-20 is rated to a flow temperature of 300 °C, whereas the other 2 models are rated to a flow temperature of 150 °C. Ultimately, it was decided that size is more important than temperature rating.

TSI model 1260A-10 is a platinum hot-film sensor. The hot-film has a diameter of 25.4 μm and an active sensor length of 0.51 mm. It is possible to use this sensor with a Dantec model 56C17 constant temperature anemometer (CTA) fitted with a Dantec model 56C01 CTA bridge. The sensor has a maximum frequency response of approximately 100 kHz. The TSI model 1220-20 and Dantec model 55R01 can potentially be used as alternate components to the 1260A-10 with minor modifications to the probe design.

D.2.2 Pressure Transducer

A miniature piezoresistive pressure transducer was selected for use in the new probe, so that the transducer could be built directly into the probe body. This eliminates the lag time associated with the use of tubing to connect an externally located pressure transducer.

Pressure transducers manufactured by Kulite and ENDEVCO were considered for use in the new probe. All of the transducers considered have similar cost and performance specifications, but the Kulite transducers are smaller (see Figure D.2). Kulite models XCQ-062 and XCE-062 were considered. Model XCQ-062 costs \$837 and is rated to an operating temperature of 120 °C, whereas model XCE-062 costs \$914 and is rated to an operating temperature of 273 °C. The other performance specifications of the two Kulite transducers are the same. The Kulite transducers have a rated accuracy of $\pm 0.5\%$ full-scale, a frequency response of about 50 kHz, and an excitation of 10 VDC. Kulite model XCE-062 was selected for use in the new probe, so

that the pressure transducer would not be the limiting factor in the temperature rating of the probe. Also, the 120 °C temperature rating of the XCQ-062 is borderline for Mach 5 operation in the hypersonic tunnel, which requires heating of the flow. The range of the transducer selected will be 0-50 psia to be compatible with the flow conditions encountered in the VT supersonic and hypersonic wind tunnels. A Measurement Group 2310 Signal Conditioning Amplifier could be used to power the transducer as well as amplify and filter the output signal. ENDEVCO model 8507C-50 can potentially be used as an acceptable alternate to the Kulite model XCE-062 transducer with minor modifications to the probe design.

D.2.3 Thermocouple

Omega butt weld type and beaded type thermocouples were considered for use in the new probe. Beaded type thermocouples have time constants that are about 1.5X the time constant of an equivalent diameter butt weld type thermocouple. Also, the diameter of the thermocouple influences its response time. Smaller diameter thermocouples have faster response times. Therefore, a butt weld type T thermocouple with a very small wire diameter of 0.025 mm (0.001 in) was selected. This type of thermocouple has a time constant of 4 ms when used in air at a flow velocity of 18.3 m/s (60 ft/s). These flow conditions are very similar to the conditions that occur inside the probe (refer to Figure D.4). When responding to a step input, it takes 5 time constants for the thermocouple to approach 100% of the correct reading. Therefore, the thermocouple is expected to have a response time of about 20 ms. Further analysis will show that this is the limiting factor in the response time of the probe. Thus, the new probe will have a response time in the range of 20 ms. The frequency response of the thermocouple is approximately 50 Hz, which will limit the frequency response of the probe. Type T thermocouples have the highest rated accuracy (± 0.5 °C) for the probe operating conditions, so this is the reason for selecting this type. The selected thermocouple (Omega model COCO-001) costs \$24 for a package of 5.

D.3 Probe Design

Figure 5.4 shows a diagram of the new concentration probe design. The new design uses a slightly different approach for sensor location than the previous designs that have been discussed. In the previous designs, the hot-film sensor was located very close to the probe tip.

In the new design, the hot-film sensor is located in the probe body and the flow is turned around an elbow before reaching the sensor location. This design allows the probe to be streamlined to have a minimal influence on the flow. Alternatively, a right angle hot-film sensor could be used to achieve this same result (minimal influence on the flow). However, the use of a right-angle hot-film makes the probe housing more complicated as the sensor needs to be removable if it breaks. Sealing the housing is also difficult for a right-angle hot-film sensor.

One disadvantage of locating the sensors away from the probe tip is this increases the response time of the probe. However, the increase in response time will be shown to be minimal as the flow through time of the probe is on the order of 5 ms for most operating conditions (see Figure 7). Thus, the placement of the sensors inside the probe is a trade-off between size and response time.

The new concentration probe design was developed to be very similar in shape and size to the five-hole probe. The complete probe assembly including a hex shaped mounting base is shown in Figure D.3. The hex shaped mounting base is designed to be built in two halves. The wiring and vacuum pump tubing coming from the concentration probe is routed out of a hole in the mounting base. BNC connectors will be used for the cabling associated with the hot-film sensor and pressure transducer. A miniature type thermocouple connector will be used to connect the thermocouple. The tip of the probe will be aligned to be parallel to the flats of the hex during manufacture, so that the probe can be aligned in the wind tunnels using the flats of the hex with a digital level. Furthermore, the hex shaped mounting base has the same dimensions as the five-hole probe, so that it is compatible with existing mounting hardware for the five-hole probe.

The probe housing is designed to be made from 304 stainless steel (SS). The external tubing will also be made from 304 SS. The probe tip is angled at 5 degrees relative to the freestream to allow measurements to be made near a wind tunnel floor. The tip is made from 416 SS for improved wear resistance. However, 416 SS is difficult to manufacture and the probe tip is a particularly difficult piece to build. Alternatively, the probe tip can be built from brass to make it easier to manufacture. The internal tubing can be made from 304 SS, copper, or a flexible material like tygon. Securing and sealing of the tubing can be accomplished by bonding with

epoxy, soldering, or brazing. If epoxy is used, the temperature rating of the epoxy should be equal to or greater than the temperature rating of the lowest rated component in the probe. Sealing around the base of the hot-film sensor is accomplished using a simple rubber gasket.

Significant effort has been made to make this probe easier to build and repair than the Maddalena probe even though this new probe design is significantly smaller in size. The Maddalena probe routes wires through tight spaces and has wiring that is bonded to the outside of the probe body. The Maddalena probe also made significant use of epoxy as a sealant, which makes repair difficult as epoxy usually must be removed to allow for repair. The new probe design provides ample space for wire routing and all of the wiring is contained within the probe body. A removable cover allows access to all sensors and wiring if repair is needed. Sealing mechanisms such as rubber gaskets are used instead of epoxy when possible. Overall, the design of the new probe should make disassembly, repair, and reassembly easier.

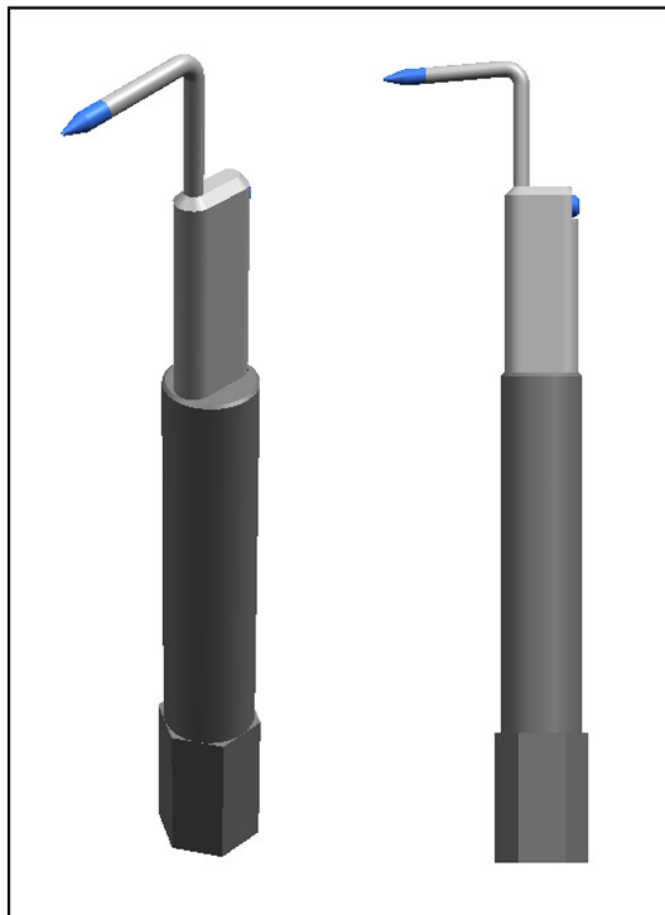
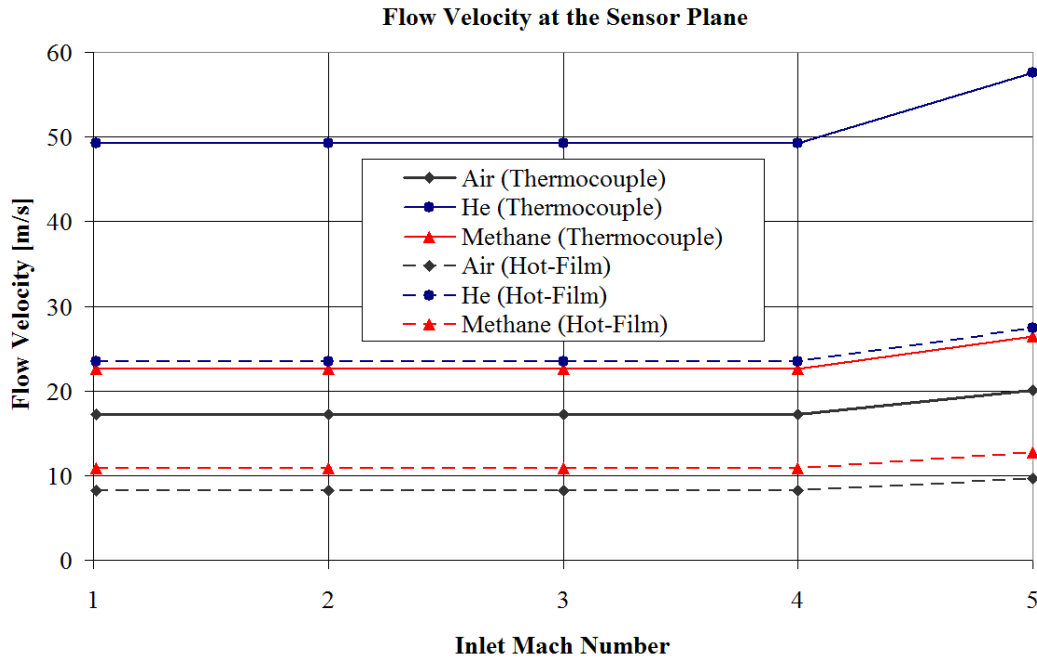


Figure D.3: New concentration probe design with mounting base attached

D.3.1 One Dimensional, Steady Flow Analysis

The one-dimensional, steady flow analysis method used by Xillo et al.⁴⁵ was adapted to analyze the flow through the new probe in order to develop the probe design. The existing probe was also analyzed, so that the relative performance of the new probe design vs. the existing probe design could be assessed. The inlet area, throat area, and measurement plane areas for the new probe design were chosen based upon this analysis. In the new probe design, the measurement region has two cross-sectional areas associated with it. The thermocouple was placed in a region with a lower cross-sectional area than the hot-film sensor and the pressure transducer. This was done to increase the flow velocity at the thermocouple location, which reduces the response time of the thermocouple. In the existing probe design, all of the sensors were located in a region with the same cross-sectional area. Based on the 1-D analysis, the inlet and throat diameters for the new probe design were chosen to be the same value as the existing probe design, 0.64 mm (0.025 in). The choices made for these dimensions prevent the occurrence of a standoff shock in front of the probe tip. The diameter at the thermocouple location was chosen to be 2.16 mm (0.085 in) and the diameter at the hot-film location was chosen to be 3.18 mm (0.125 in). The choices made for these dimensions influence factors such as the overall size of the probe, the flow velocity in the measurement region, and the flow through time for the probe. The results of the 1-D analysis for the new probe design vs. the existing probe design (i.e. the Maddalena probe) are shown in Figures D.4 – D.6. These calculations were performed based upon the nominal flow conditions for the hypersonic wind tunnel. The flow conditions for the supersonic tunnel are similar.

New Probe Design



Existing Probe

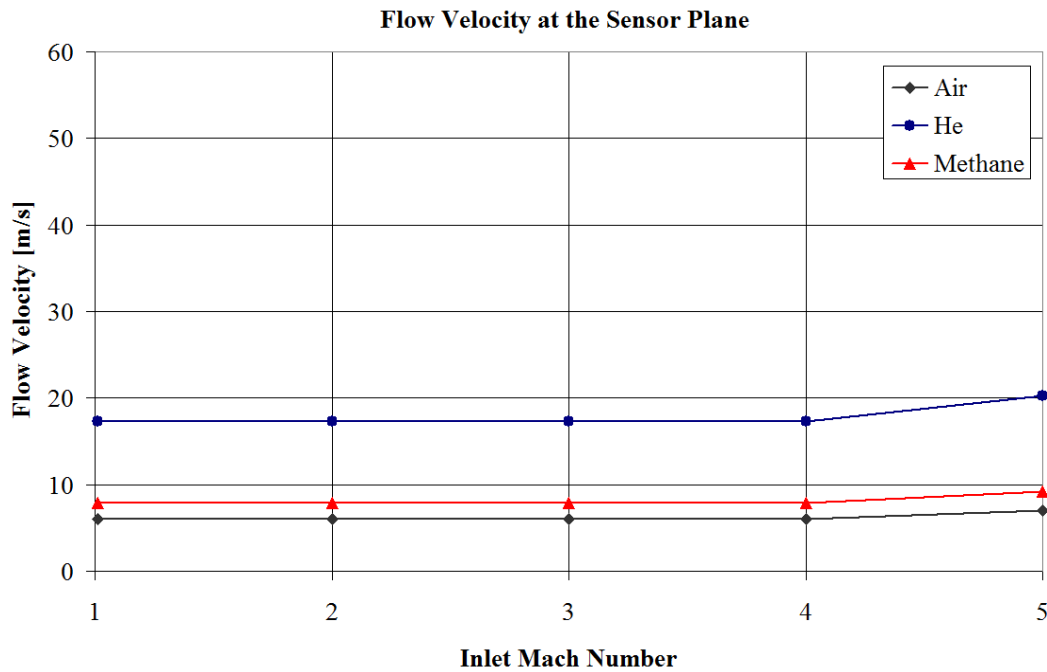
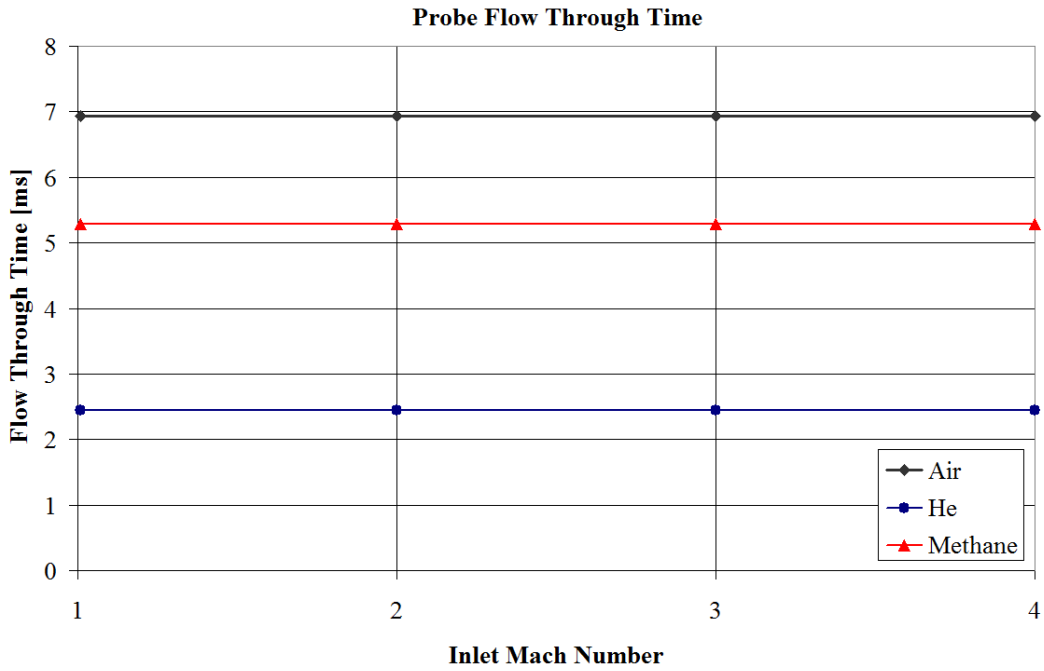


Figure D.4: Comparison of the flow velocity at the sensor plane for the new concentration probe design vs. the existing probe

New Probe Design



Existing Probe

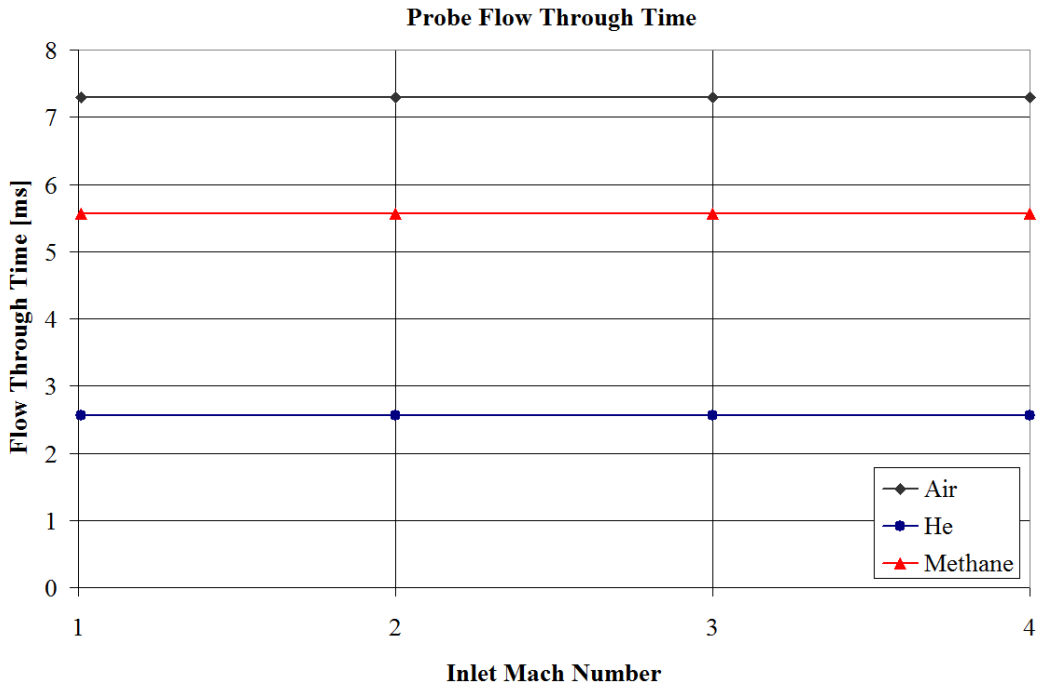


Figure D.5: Comparison of the flow through time for the new concentration probe design vs. the existing probe

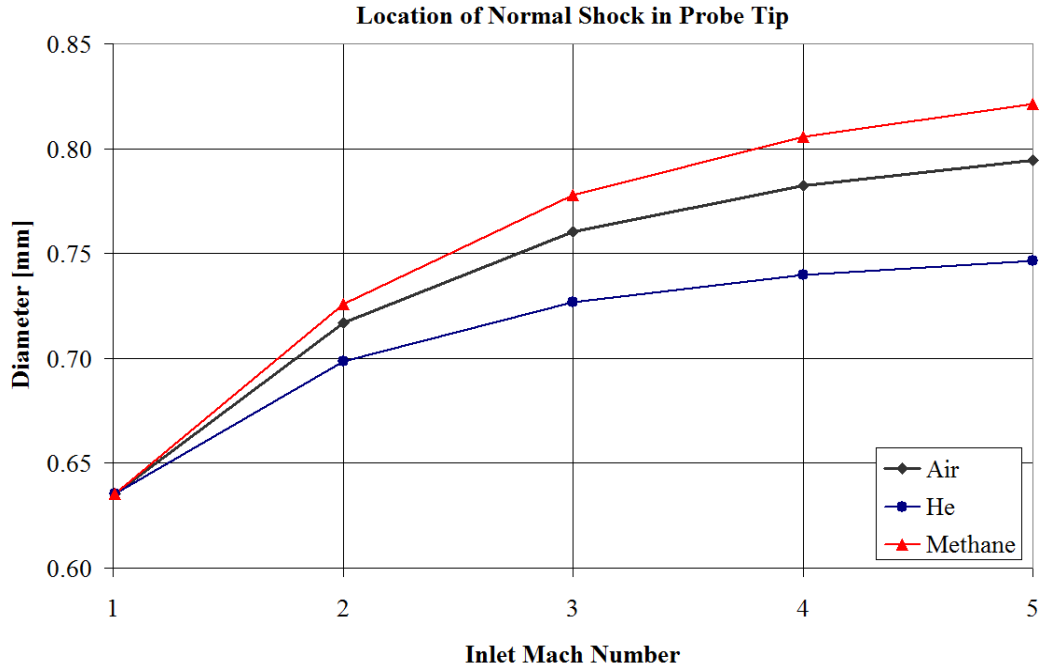


Figure D.6: Location of the normal shock in the probe tip for both the new concentration probe design and the existing probe design

D.4 Conclusions

A miniature, fast-response concentration probe design has been developed that is robust, reliable, inexpensive (compared to optical methods), and capable of detecting multiple types of gases. The probe uses a miniature hot-film sensor made by TSI, a miniature piezoresistive pressure transducer built by Kulite, and one of the fastest response thermocouples available from Omega. The material cost for building the probe is estimated to be about \$2,000. The approximate technical specifications of the probe are as follows:

- Response time: 20 – 25 ms
- Maximum frequency response: 50 Hz
- Capable of measuring multiple types of gas mixtures
- Measurement uncertainty: approximately the same as shown in Figure 2.26

The primary limitations of the probe are:

- Capable of measuring of binary gas mixtures only
- Sensitivity of the probe varies depending on the molecular weight of the mixture being measured (refer to Section 2.3.4.2)

The primary advantages over the previous probe design are:

- Significant reduction in size (refer to Figure 5.5)
- Significant improvement in response time (pause time at each data point will be reduced from 200 ms to approximately 50 ms)
- Improved frequency response (increased from approximately 20 Hz to 50 Hz)

Ultimately, this probe could be a valuable resource for conducting fuel injection and mixing experiments in short duration wind tunnel facilities.

References

- ¹ Fry, R.S., "A Century of Ramjet Propulsion Technology Evolution," *Journal of Propulsion and Power*, Vol. 20, No. 1, pp. 27-58, January-February 2004.
- ² Van Wie, D.M., D'Alessio, S.M., and White, M.E., "Hypersonic Airbreathing Propulsion," *Johns Hopkins APL Technical Digest*, Vol. 26, No. 4, pp. 430-437, 2005.
- ³ McClinton, C.R., Andrews, E.H., and Hunt, J.L., "Engine Development for Space Access: Past, Present, and Future," *International Symposium on Air Breathing Engines*, ISABE Paper 2001-1074, January 2001.
- ⁴ Curran, E.T., "Scramjet Engines: The First Forty Years," *Journal of Propulsion and Power*, Vol. 17, No. 6, pp. 1138-1148, November-December 2001.
- ⁵ Kutschenreuter, P., "Supersonic Flow Combustors" in Scramjet Propulsion (E.T. Curran and S.N.B. Murthy, Editors), AIAA, 2000.
- ⁶ McClinton, C.R., Torrence, M.G., Gooderum, P.B., and Young, I.G., "Non Reactive Mixing Study of a Scramjet Swept-Strut Fuel Injector," NASA TN D-8069, December 1975.
- ⁷ Hsu, K., Carter, C.D., Gruber, M.R., and Tam, C., "Mixing Study of Strut Injectors in Supersonic Flows," AIAA Paper 2009-5226, August 2009.
- ⁸ Hartfield, R.J., Hollo, S.D., and McDaniel, J.C., "Experimental Investigations of a Supersonic Swept Ramp Injector using Laser Induced Iodine Fluorescence," *Journal of Propulsion and Power*, Vol. 10, No. 1, pp. 129-135, January-February 1994.
- ⁹ Riggins, D.W. and Vitt, P.H., "Vortex Generation and Mixing in Three-Dimensional Supersonic Combustors," *Journal of Propulsion and Power*, Vol. 11, No. 3, pp. 419-426, May-June 1995.
- ¹⁰ Rogers, R.C., "A study of the Mixing of Hydrogen Injected Normal to a Supersonic Airstream," NASA TN D-6114, March 1971.
- ¹¹ McClinton, C.R., "The effect of Injection Angle on the Interaction Between Sonic Secondary Jets and a Supersonic Freestream," NASA TND-6669, February 1972.
- ¹² Lin, K., Ryan, M., Carter, C., Gruber, M., Raffoul, C., "Raman Scattering Measurements of Gaseous Ethylene Jets in Mach 2 Supersonic Crossflow," *Journal of Propulsion and Power*, Vol. 26, No. 3, pp. 503-513, May-June 2010.

-
- ¹³ Barber, M.J., Schetz, J.A., and Roe, L.A., "Normal Sonic Helium Injection Through a Wedge-Shaped Orifice into a Supersonic Flow," *Journal of Propulsion and Power*, Vol. 13, No. 2, pp. 257-263, March-April 1997.
- ¹⁴ Tomioka, S., Jacobsen, L.S., and Schetz, J.A., "Sonic Injection from Diamond-Shaped Orifices into a Supersonic Crossflow," *Journal of Propulsion and Power*, Vol. 19, No. 1, pp. 104-114, January-February 2003.
- ¹⁵ Srinivasan, R. and Bowersox, R.D.W, "Simulation of Transverse Gaseous Injection Through Diamond Ports into Supersonic Freestream," *Journal of Propulsion and Power*, Vol. 23, No. 4, pp. 772-782, July-August 2007.
- ¹⁶ Gruber, M.R., Nejad, A.S., Chen, T.H., and Dutton, J.C., "Mixing and Penetration Studies of Sonic Jets in a Mach 2 Freestream," *Journal of Propulsion and Power*, Vol. 11, No. 2, pp. 315-323, March-April 1995.
- ¹⁷ Gruber, M.R., Nejad, A.S., Chen, T.H., and Dutton, J.C., "Transverse Injection from Circular and Elliptic Nozzles into a Supersonic Crossflow," *Journal of Propulsion and Power*, Vol. 16, No. 3, pp. 449-457, May-June 2000.
- ¹⁸ Lewis, D.P. and Schetz, J.A., "Tangential Injection from Overlaid Slots into a Supersonic Stream," *Journal of Propulsion and Power*, Vol. 13, No. 1, pp. 59-63, January-February 1997.
- ¹⁹ Schetz, J.A., Billig, F.S., Favin, S., and Gilreath, H.E., "Effects of Pressure Mismatch on Slot Injection in a Supersonic Flow," *International Journal of Turbo and Jet Engines*, Vol. 9, No. 2, pp. 135-146, 1992.
- ²⁰ Schetz, J.A., "Interaction Shock Shape for Transverse Injection in Supersonic Flow," *Journal of Spacecraft and Rockets*, Vol. 7, No. 2, pp. 143-149, February 1970.
- ²¹ Fuller, R.P., Wu, P.K., Nejad, A.S., and Schetz, J.A., "Comparison of Physical and Aerodynamic Ramps as Fuel Injectors in Supersonic Flow," *Journal of Propulsion and Power*, Vol. 14, No. 2, March-April 1998.
- ²² Jacobsen, L.S., Gallimore, S.D., Schetz, J.A., O'Brien, W.F., and Goss, L.P., "Improved Aerodynamic-Ramp Injector in Supersonic Flow," *Journal of Propulsion and Power*, Vol. 19, No. 4, July-August 2003.

-
- ²³ Maddalena, L., Campioli, T.L., and Schetz, J.A., "Experimental and Computational Investigation of an Aeroramp Injector in a Mach Four Cross Flow," AIAA 2005-3235, June 2005.
- ²⁴ Schetz, J.A., Thomas, R.H., and Billig, F.S., "Mixing of Transverse Jets and Wall Jets in Supersonic Flow," IUTAM Symposium on Separated Flows and Jets, Novosibirsk, Russia, July 1990.
- ²⁵ Seiner, J.M., Dash, S.M., and Kenzakowski, D.C., "Historical Survey on Enhanced Mixing in Scramjet Engines," Journal of Propulsion and Power, Vol. 17, No. 6, pp. 1273-1286, November-December 2001.
- ²⁶ Mays, R.B. Thomas, R.H., and Schetz, J.A., "Low Angle Injection into a Supersonic Flow," AIAA Paper 89-2461, July 1989.
- ²⁷ Schetz, J.A., Hawkins, P.F., and Lehman, H., "Structure of Highly Underexpanded Transverse Jets in a Supersonic Stream," AIAA Journal, Vol. 5, No. 5, pp. 882-884, 1967.
- ²⁸ Viti, V., Neel, R., Schetz, J.A., "Detailed Flow Physics of the Supersonic Jet Interaction Flow Field," Physics of Fluids, Vol. 21, No. 046101, 2009.
- ²⁹ Ben-Yakar, A., Mungal, M.G., and Hanson, R.K., "Time Evolution and Mixing Characteristics of Hydrogen and Ethylene Transverse Jets in Supersonic Crossflows," Physics of Fluids, Vol. 18, No. 026101, 2006.
- ³⁰ Gruber, M.R., Nejad, A.S., Chen, T.H., and Dutton, J.C., "Compressibility Effects in Supersonic Transverse Injection Flowfields," Physics of Fluids, Vol. 9, No. 5, pp. 1448-1461, May 1997.
- ³¹ Portz, R. and Segal, C., "Mixing in High-Speed Flows with Thick Boundary Layers," AIAA Paper 2004-3655, July 2004.
- ³² McClinton, C.R., "Effect of Ratio of Wall Boundary-Layer Thickness to Jet Diameter on Mixing of a Normal Hydrogen Jet in a Supersonic Stream," NASA TM X-3030, June 1974.
- ³³ Segal, C., The Scramjet Engine: Processes and Characteristics, Cambridge University Press, New York, NY, 2009.
- ³⁴ Cohen, L.S, Coulter, L.J., and Egan, W.J., Jr., "Penetration and Mixing of Multiple Gas Jets Subjected to a Cross Flow," AIAA Journal, Vol. 9, No. 4, pp. 718-724, April 1971.

-
- ³⁵ Billig, F.S., Orth, R.C., and Lasky, M., "A Unified Analysis of Gaseous Jet Penetration," AIAA Journal, Vol. 9, No. 6, pp. 1048-1058, June 1971.
- ³⁶ Billig, F.S. and Schetz, J., "Analysis of Penetration and Mixing of Gas Jets in Supersonic Cross Flow," AIAA Paper 1992-5061, December 1992.
- ³⁷ Torrence, M.G., "Effect of Injectant Molecular Weight on Mixing of a Normal Jet in a Mach 4 Airstream," NASA TN D-6061, January 1971.
- ³⁸ Brinckman, K.W., Calhoun, W.H., Jr., and Dash, S.M., "Scalar Fluctuation Modeling for High-Speed Aeropropulsive Flows," AIAA Journal, Vol. 45, No. 5, pp. 1036-1046, May 2007.
- ³⁹ Brinckman, K., and Dash, S.M., "Advances In Scalar Fluctuation Modeling and Automated Validation Tools for High-Speed Propulsion Applications," AIAA Paper 2008-2534, April 2008.
- ⁴⁰ Ungewitter, R.J., Brinckman, K., and Dash, S.M., "Advanced Modeling of New Fuel/Air Mixing Data Sets for Scramjet Applications," AIAA Paper 2009-4940, August 2009.
- ⁴¹ ASME MFC-3M-2004, "Measurement of Fluid Flow in Pipes Using Orifice, Nozzle, and Venturi," ASME, New York, NY, 2005.
- ⁴² Miller, R.W., "Flow Measurement Engineering Handbook, 2nd Edition," R.R. Donnelly & Sons Company, 1989.
- ⁴³ Ninnemann, T.A. and Ng, W.F., "A Concentration Probe for the Study of Mixing in Supersonic Shear Flows," Experiments in Fluids, Vol. 13, pp. 98-104, 1992.
- ⁴⁴ Reis, V.H. and Fenn, J.B., "Separation of Gas Mixtures in Supersonic Jets," The Journal of Chemical Physics, Vol. 39, No. 12, pp. 3240-3250, December 1963.
- ⁴⁵ Xillo, O.C., Schetz, J.A., and Ng, W.F., "A Sampling Probe for Fluctuating Concentration Measurements in Supersonic Flow," AIAA Paper 1999-519, January 1999.
- ⁴⁶ Maddalena, L., "Investigations of Injectors for Scramjet Engines," PhD Dissertation, Virginia Polytechnic Institute and State University, 2007.
- ⁴⁷ Devillers, J.F. and Diep, G.B., "Hot-Wire Measurements of Gas Mixture Concentrations in a Supersonic Flow," DISA Information 14, pp. 29-36, 1973.
- ⁴⁸ Centolanzi, F.J., "Characteristics of a 40 degree Cone for Measuring Mach Number, Total Pressure, and Flow Angles at Supersonic Speeds", NACA TN 3967, May 1957.
- ⁴⁹ Swalley, F.E., "Measurement of Flow Angularity at Supersonic and Hypersonic Speeds with the Use of a Conical Probe", NACA TN D-959, September 1961.

-
- ⁵⁰ Andrews, D.R. and Sawyer, W.G., “The Calibration of a 60° Cone to Measure Mach Number, Total Pressure and Flow Angles at Supersonic Speeds,” Aeronautical Research Council CP-628, June 1962.
- ⁵¹ Naughton, J.W., Cattafesta, L.N., and Settles, G.S., “Miniature, Fast-Response Five-Hole Conical Probe for Supersonic Flowfield Measurements,” AIAA Journal, Vol. 31, No. 3, pp. 453-458, March 1993.
- ⁵² Rock, C., Schetz, J.A., and Ungewitter, R., “Injectant Molecular Weight Effects in Injectors for Circular Scramjet Combustors,” AIAA Paper 2010-380, January 2010.
- ⁵³ Rock, C., Schetz, J.A., and Ungewitter, R., “Experimental and Numerical Studies of a Strut Injector for Round Scramjet Combustors,” AIAA Paper 2009-7313, October 2009.
- ⁵⁴ Burger, S.K., “Investigation of Injectant Molecular Weight and Shock Impingement Effects on Transverse Injection Mixing in Supersonic Flow,” Master’s Thesis, Virginia Polytechnic Institute and State University, April 2010.
- ⁵⁵ Ombrello, T., Qin, X., Ju, Y., Gutsol, A., Fridman, A., and Carter, C., “Combustion Enhancement via Stabilized Piecewise Nonequilibrium Gliding Arc Plasma Discharge,” AIAA Journal, Vol. 44, No. 1, pp. 142-150, January 2006.
- ⁵⁶ Hsu, K.Y., Carter, C.D., Gruber, M.R., and Barhorst, T., “Experimental Study of Cavity-Strut Combustion in Supersonic Flow,” AIAA Paper 2007-5394, July 2007.
- ⁵⁷ Gruber, M., Carter, C., Ryan, M., Rieker, G.B., Jeffries, J.B., Hanson, R.K., Liu, J., and Mathur, T., “Laser-Based Measurements of OH, Temperature, and Water Vapor Concentration in a Hydrocarbon-Fueled Scramjet,” AIAA Paper 2008-5070, July 2008.
- ⁵⁸ Rieker, G.B., Liu, J.T.C., Jeffries, J.B., Hanson, R.K., Mathur, T., Gruber, M.R., and Carter, C.D., “Diode Laser Sensor for Gas Temperature and H₂O Concentration in a Scramjet Combustor Using Wavelength Modulation Spectroscopy,” AIAA Paper 2005-3710, July 2005.
- ⁵⁹ Smith, S., Gruber, M., Mathur, T., Ryman, R., Diemer, J., and Tam, C., “Development of a Rotating Probe System for Supersonic Combustion Experiments,” AIAA Paper 2009-5034, August 2009.
- ⁶⁰ Anderson, J.D., Modern Compressible Flow with Historical Perspective, Third Edition, McGraw-Hill, New York, NY, 2003.

⁶¹ NACA Report 1135, "Equations, Tables, and Charts for Compressible Flow," National Advisory Committee for Aeronautics, Washington, DC, 1953.

⁶² Coleman, H.W. and Steele, W.G., Jr., Experimentation and Uncertainty Analysis for Engineers, Wiley, New York, NY, 1989.

⁶³ Brown, G.L. and Rebollo, M.R., "A Small, Fast-Response Probe to Measure Composition of a Binary Gas Mixture," AIAA Journal, Vol. 10, No. 5, pp. 649-652, May 1972.